QV: THE QUAD WINGED, ENERGY EFFICIENT, SIX DEGREE OF FREEDOM CAPABLE MICRO AERIAL VEHICLE

A Ph.D. Dissertation
Presented to
The Academic Faculty

by

Jayant Ratti

In Partial Fulfillment
of the Requirements for the Degree
Doctor of Philosophy in the
Robotics Department
(Home School:Electrical and Computer Engineering)

Georgia Institute of Technology
May, 2011

QV: THE QUAD WINGED, ENERGY EFFICIENT, SIX DEGREE OF FREEDOM CAPABLE MICRO AERIAL VEHICLE

Approved by:

Ayanna Howard
Committee Chair
Dept. of Electrical and Computer Engineering
Georgia Institute of Technology

George Vachtsevanos
Advisor
Dept. of Electrical and Computer Engineering
Georgia Institute of Technology

Tucker Balch
College of Computing
Georgia Institute of Technology

Wayne Book
Dept. of Mechanical Engineering
Georgia Institute of Technology

Magnus Egerstedt
Dept. of Electrical and Computer Engineering
Georgia Institute of Technology

Date Approved: March 31, 2011

“Karmani ave adhikars te
–you have the power to act only
ma phalesu kadachana
–you do not have the power to influence the result
ma karmaphal hetur bhoo
–therefore you must act without the anticipation of the result
ma sangostu akramani
–without succumbing to inaction”

The translation from *Sanskrit* follows thus:
“Thou hast power only to act, not over the result thereof. Act thou therefore without prospect of the result and without succumbing to inaction.

– Bhagwad Gita

To my family,

My Parents, My Grandparents, My Brothers

Without all of whom I would not have achieved anything in life.

PREFACE

Biologically inspired design was not the first thing to attract me when searching for a PhD topic and the prospect of making a biologically inspired Aerial Vehicle design to achieve what every other helicopter, airplane is already doing so well just seemed a waste of good time and effort. Getting to work on a conceptually new electro-mechanical design never before conceived was by far the biggest driving factor in pursuing the present research. Although, as time progressed and a lot of background, field knowledge gained in the present state of the art, it was made clear that conventional steady state aerodynamics harnessed by helicopters and airplanes was not the elixir it seemed to be at first. With some discussion with James (Seong-Joo Kim) and a lot of literature review back in 2008, it was quickly realized how indispensable it is to perform insect like flapping to go smaller in size and larger in flight endurance. The question on my mind was, if it is really that obvious then why is there no research on or electro-mechanical system already developed which can perform just as efficiently as the insects and small birds. Reading on the work of Khan and Aggarwal and work done by Caltech on the MicroBat, it was soon realized that these systems were approaching the problem on the lines of what was already existing in actuation systems and the focus was on building on top of the existing technology by improving on feathering, reducing weight, downsizing the scale etc. A lot of researchers proposed using resonance flapping for air vehicles and a lot of papers were published as well, but none materialized into true resonance flapping prototypes. Also, the flight times and payload capacities of biologically inspired micro aerial vehicles was astoundingly poor. What began as cynicism, turned into a question and finally a challenge to produce theoretically sound and practically demonstrable/functional prototype, bolstering the original theoretical and simulation work.

ACKNOWLEDGEMENTS

First I would like to acknowledge my advisor, Dr. George Vachtsevanos. His patient instruction and guidance has paved the path through my study and research. On the same note I thank all my friends and colleagues from the Intelligent Control Systems Laboratory, whose collaboration, guidance and support was essential in successfully meeting project / research objectives pertinent to the Micro Aerial Vehicle design and development.

I would also like to thank the committee members for their time and generosity in accepting to be on my committee and taking the time to attend my defense.

I acknowledge the Electrical and Computer Engineering Department for providing lab facilities, software and hardware resources, which have greatly contributed towards the development of the project. I also thank Impact Technologies, LLC for sponsoring in part the hardware development for the project. I thank Georgia Institute of Technology for providing me the right research environment and campus wide resources which went a long way in helping me meet my research and thesis objectives.

I thank all the contributors of the LyX document processor for providing the open source tools used in the composition of this thesis. I thank Doug W. Brown for his help in structuring the LyX template to conform with the LaTeX based Georgia Tech Thesis template.

On a last note, I acknowledge my family members. Many thanks to my brother Karan Ratti for provided untiring motivation during my research. I sincerely thank my Late grandmothers Shakuntala Ahuja and Krishna Ratti for their guidance and wisdom over the years. My greatest thanks to my parents Dr. J.B. Ratti and Dr. Neeta Ratti for their years of support, guidance and role modeling for all my endeavors all through my life.

TABLE OF CONTENTS

LIST OF TABLES

LIST OF FIGURES

SUMMARY

Micro Aerial Vehicles (MAVs) are a class of Unmanned Aerial Vehicles (UAVs) designed for closed-quarter and small/tight space navigational operations. The conventional Micro Aerial Vehicle (MAV) as outlined by the Defense Advanced Research Projects Agency (DARPA), is a vehicle that can have a maximum dimension of 6 inches and weighs no more than 100 grams. Under these tight constraints, the footprint, weight and power reserves available for on-board avionics and actuators is drastically reduced; the flight time and payload capabilities of MAVs take a massive toll in keeping up with these stringent size constraints. However, the demand for micro flying robots is increasing rapidly.

The applications that have emerged over the years for MAVs include search & rescue operations, remote Intelligence, Surveillance and Reconnaissance (ISR), among many others. However, the biggest setback in urban operations and closed quarter navigation is enabling hover-capability / Vertical-Take-Off-and-Landing (VTOL) along with long flight times, high sensor/telemetry payload capacity and small size. VTOL capable rotary and fixed wing flying vehicles do not scale down to micro sized levels, owing to the severe loss in aerodynamic efficiency associated with low Reynolds number physics on conventional airfoils. Some of the biologically inspired designs developed so far include the MicroBat, by Caltech, Mentor, by University of Toronto and Delfly by the Technical University of Delft and Wageningen University and lately the Hummingbird by Aerovironment. However, the present state of the art lacks in one or more of the minimum qualities required from an MAV: Appreciable flight time, payload capacity and Six Degrees of Freedom (6DoF) hovering/VTOL performance. This PhD. work is directed towards overcoming these limitations.

Firstly, this PhD thesis presents the advent of a novel Quad-Wing MAV configuration (termed, QV) capable of performing all 6DoF flight maneuvers. The thesis presents the theory, conceptualization, design, simulation study and finally hardware design/development

of the MAV.

Secondly, it proves and demonstrates a significant improvement in on-board energy-harvesting, capable of resulting in increased flight times and payload capacities of the order of even 200%-400% and more.

Thirdly, the thesis defines a new actuation principle, called Fixed Frequency, Variable Amplitude (FiFVA). It is demonstrated that by the use of passive elastic members on wing joints, a further noteworthy increase in energy efficiency, and consequently reduction in input power requirements is observed. An actuation efficiency increase of over 100% in many cases is predicted. The natural evolution of the actuation development led to invention of two novel actuation mechanisms that are intended to illustrate the FiFVA actuation principle, and consequently show energy savings and flapping efficiency improvement.

Finally, the thesis presents supplementary work in the design, development of two novel Micro Architecture and Control (MARC) avionics platforms (autopilots) to demonstrate flight control and communication capability on-board the four-wing flapping prototype. The design of a novel passive feathering mechanism aimed to improve lift/thrust performance of flapping motion is also presented.

The contributions emerging from the research are:

1. A novel Quad-Wing MAV configuration (termed, QV) for generating a very notable increase in flight time and payload capacity.
2. A novel 6DoF flight control law for the Quad-Wing MAV design.
3. A novel resonance flapping principle termed FiFVA, for significantly improving flapping efficiency using passive elastic elements on wing joints (springs).
4. Two novel FiFVA operated mechanical actuation prototypes and a fully functional Quad-Wing MAV prototype with two indigenously developed Micro Architecture and Control (MARC) avionics platforms.

CHAPTER I

INTRODUCTION

1.1 NOVEL CONTRIBUTIONS OF THE RESEARCH

1. It is shown through the course of discussion and analysis within the dissertation, how increasing the actuation unit of a two wing flapping wing design, resulting in a four wing design, leads to significant increase in flight energy reserves on-board the MAV, leading to longer flight times and higher payload capacities.
2. By adding passive elastic elements (springs), directly or indirectly at the wing joints, a spring-inertia system is created, having a natural resonance frequency. By flapping the wings at the system's natural frequency, significant improvement in flapping efficiency is observed.
3. A novel 6DoF flight control for the four wing flapping design was realized and tested in simulation. The first revision of the hardware prototype was developed to demonstrate three degrees of freedom (pitch, roll and yaw) on a benchtop apparatus.

1.2 PROBLEM DESCRIPTION & BACKGROUND

The conventional Mini and Large scale Unmanned Aerial Vehicle systems span anywhere from approximately 12 inches to 12 feet; endowing them with larger propulsion systems, batteries/fuel-tanks, which in turn provide ample power reserves for long-endurance flights, powerful actuators, on-board avionics, wireless telemetry etc. The limitations thus imposed become apparent when shifting to Micro Aerial Vehicles (MAVs) and trying to equip them with equal or near-equal flight endurance, processing, sensing and communication capabilities, as their larger scale cousins. The conventional MAV as outlined by The Defense Advanced Research Projects Agency (DARPA) is a vehicle that can have a maximum dimension of 6 inches and weighs no more than 100 grams. Under these tight constraints, the

Table 1.1: MAV Design Requirements / Minimum Specifications (As defined by DARPA)

Specifications	Requirements	Details
Size	< 15.24cm (6 in)	Maximum dimension
Weight	~100 g	Objective GTOW
Range	1 to 10 Km	Operational Range
Endurance	60 min	Loiter time or station
Altitude	< 150 m	Operational ceiling
Speed	15 m/s	Maximum flight time
Payload	20 g	Mission dependent
Cost	$ 1500	Maximum cost

footprint, weight and power reserves available to on-board avionics and actuators is drastically reduced; the flight time and payload capabilities of MAVs take a massive plummet in keeping with these stringent size constraints. However, the demand for micro flying robots is increasing rapidly.

Definition 1.1. Micro Aerial Vehicle (MAV) refers to a class of UAVs, that is restricted to a maximum size of 6" (or 15 cm) in any dimension and a Gross Take Off Weight (GTOW) of less than 100 g, as specified by the Defense Advanced Research Projects Agency (DARPA). Other specifications for an MAV as specified by DARPA [22, 34] are listed in Table 1.1.

1.3 PROBLEM ORIGINS

Missions envisioned for MAVs, such as Intelligence, Surveillance and Reconnaissance (ISR), home/personal security, recreation (gaming etc), patrolling, search & rescue etc in urban environments require exceptional long flight times and significant sensor payloads. These missions typically involve flight through or in close proximity to buildings, tunnels, foliage, rubble, hazardous areas, requiring the MAVs to maneuver using sharp dives and climbs along with small-radius turns. The small size of MAVs allows such dynamic flight operations within confined space but the control effectors must provide sufficient power for both dynamic maneuvers and long flight times. Also MAVs operate in a very sensitive Reynolds number regime; wherein aerodynamic flow physics exhibits strong variance

from conventional steady aerodynamic effects seen over the wings of fixed and rotary wing MAVs. Hence, designing vehicles that can efficiently fly in this regime represents an entirely new challenge to design engineers.

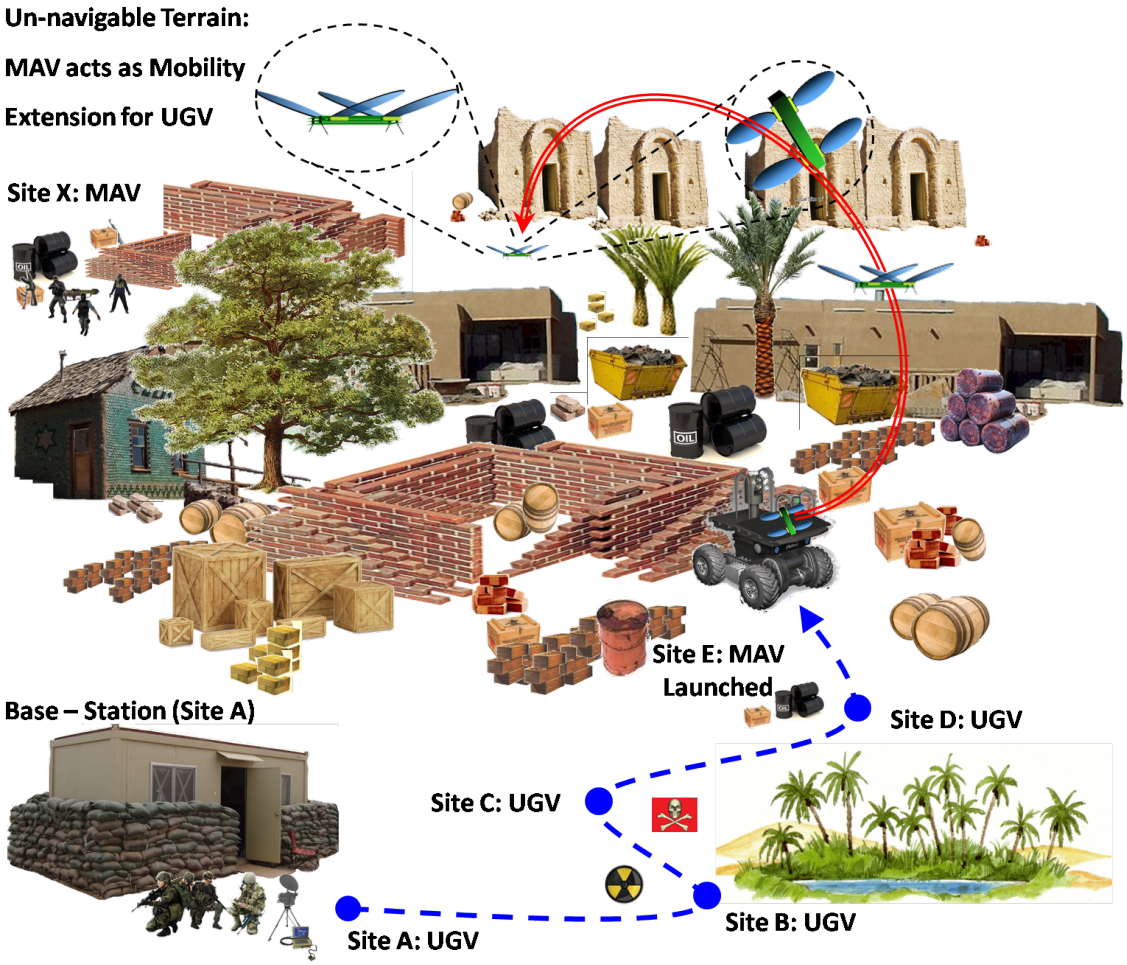

Figure 1.1: Example Mission: Long Endurance MAV Mission: Search & Rescue / ISR

Remark 1.1. The last 30 years have provided significant development in larger-scale UAVs, which can provide some insight and guidance into the performance of microscale fixed-wing and rotary-wing MAV designs. The small size requirements of the MAV limits the payload capacity and flight time performance of the flyer and limits the payload weight [34]. However insects can propel almost 2 to 12 times their own body weight while in flight. Which is unexplained by conventional laminar air flow physics models.

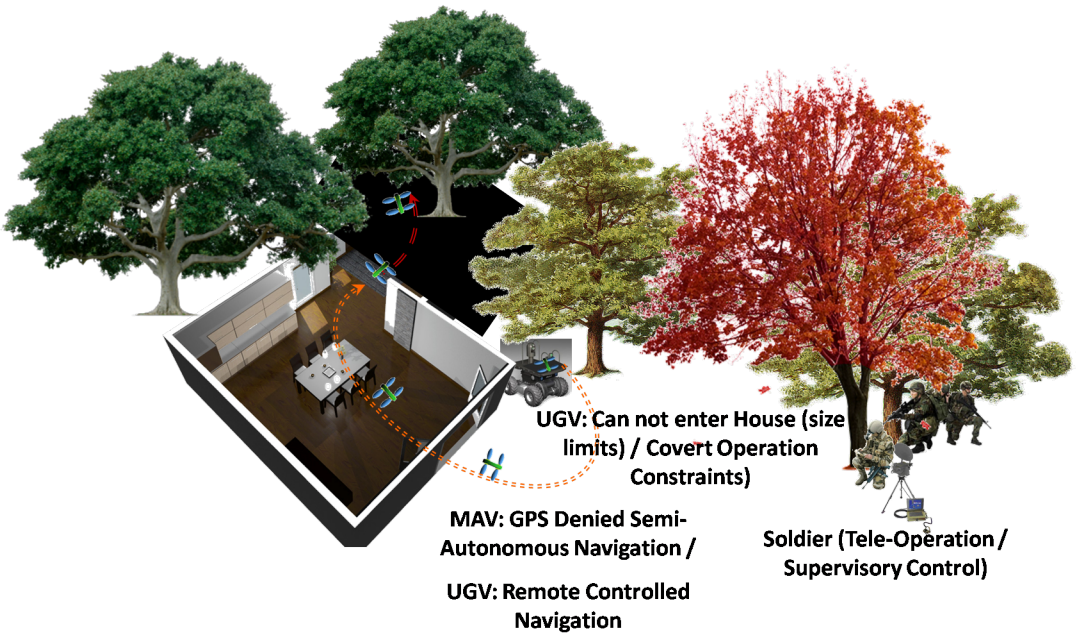

Figure 1.2: Closed-Quarter / Outdoor Operation

VTOL capable rotary and fixed wing flying vehicles do not scale down to micro sized levels, owing to the severe loss in aerodynamic efficiency associated with low Reynolds number physics on conventional airfoils. Also, the design tools and flow physics shift from conventional steady flow towards vortex formation and harvesting associated with insect and bird flights at micro sizes. Thus, researchers directed their efforts in the past few years towards the study, design and development of biologically inspired designs involving flapping wing kinematics and dynamics; efforts were directed to capture the exceptional flight endurance and payload capabilities of insects & small birds. However, the present state of the art lack in one or more of the minimum qualities required from an MAV: Appreciable flight time, appreciable payload capacity for on-board sensors/telemetry and 6DoF hovering/VTOL performance. Almost universally, these flapping machines restrict their motion to kinematically-correct, symmetric flapping that is often mechanically coupled, allowing only hovering or steady forward flight. Also leading to significantly small flight times.

Remark 1.2. At present no VTOL MAV (as per Definition 1.1) has been incorporated into the Air Force or Security Services, owing to either limited flight time capabilities and/or

limited sensor payload capacity.

1.4 PROBLEM ADDRESSED

Unlike subsonic fixed-wing aircrafts and their steady flow dynamics, biological flyers such as insects and small birds utilize vortex formation and harnessing to keep them aloft, especially in case of hovering.

Existing MAV designs cannot match the aerodynamic performance (stability, maneuverability, and efficiency) of insects and small birds due to the lack of design tools at this scale of flight. The underlying aerodynamic phenomenons and physics involved in insect and small bird flights is still a mystery and topic for much further analysis/research [7, 9, 10, 31]. The MAV platforms inspired from flapping wing, biological counterparts have shown very limited flight endurance [6, 15, 25, 45, 48]. The need of the hour calls for a paradigm shift in the development of enabling actuation and control technologies to improve flight endurance [37, 41].

If MAVs are to approach and possibly exceed the performance of biological flyers, advances are required in several fields of study which include:

1. Low Reynolds number aerodynamics $\left(4 \times 10^4\right)$(Appendix A.2)
2. Light weight and adaptive/morphing wing structures/materials and mechanisms (Appendix A.2)
3. High density energy storage (novel battery solutions) (Out of scope of present research).
4. Efficient conversion of stored energy to useful power/propulsion (Chapter 2)
5. Simple control scheme for attaining 6DoF flight with minimal actuators (Chapter 4)

Proposition 1.1. *"Flapping wing MAV flyers (as per Definition 1.1) developed to date have not been able to sustain appreciable flight times or sensor payload capacities, hence the*

Table 1.2: Present State of The Art 2000-02

2000	2000s	2002
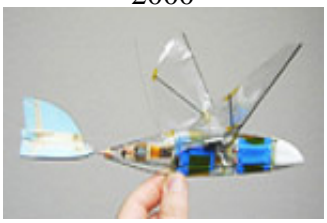		
MicroBat[48]	Univ. of Florida	Mentor [25]
2006	**2007**	**2009**
		
Delfly	Nathan Chronister	Petter Muren

re-thinking and re-designing of the core actuation (propulsion) and controls methodology for a MAV is proposed as one of the means towards overcoming the stated limitations."

1.5 STATE OF THE ART

Table 1.2[1] lists some of the state of the MAVs developed in the past. The MicroBat, developed by Aerovironment and Caltech, was the first micro-sized ornithopter resulting from MAV funding. It had three-channel radio control and used lithium-polymer batteries which had just become available. University of Florida entry at the International Micro Air Vehicle Competition. University teams compete to see who can perform the most pylon circuits with the smallest ornithopter. This annual event is held in a different location each year and also includes rotary-driven MAVs. Although some hovering freeflight ornithopters had been built by hobbyists, Mentor, developed at University of Toronto, was the first hovering ornithopter with radio control. Hovering is important for MAV applications that require maneuvering in tight spaces. Delfly, developed at the Technical University of Delft and Wageningen University, is able to transition between hovering and forward flight. This

[1] www.ornithopter.org

Table 1.3: Design and Performance Parameters for some MAVs

Flight Capable Vehicles	GTOW (grams)	Wing / Rotor Span (cms)	Endurance (min)	Hover Time (min)	Hover Power (W)
Black Widow (Aerovironment)	80	15.24	30	N/A	24.5
I-Fly Vamp (Interactive Toy)	25	22	7	N/A	N/A
Hoverfly (Aerovironment)	180	18	13.2	7.3	70
LUMAV (Auburn Univ.)	440	15.24	20	N/A	N/A
Flytech Dragonfly (Wow-Wee)	28.35	31.2	5	N/A	N/A
MicroStar (Lockheed-Martin)	110	22.86	25	N/A	N/A
Microbat (CalTech)	10.5	15.24	2	N/A	N/A
MICOR (UMD)	103	15.24	3	3	11
Da Vinci Ornithopter	8	12.5	5	N/A	N/A
DelFly II (Tech. Univ. Delft)	16	28	15	8	-
Nanoflyer (PROX)	3.0	8.5	10	10	-
μFR-II	12.3	13.6	3	3	3.5

ornithopters also carry a small video camera. Live images are analyzed by a computer on the ground, giving Delfly the capacity for autonomous navigation. This prototype developed by Nathan Chronister can hover and perform aerobatic maneuvers. Though developed for recreational use, this ornithopter achieved a MAV benchmark because it is the size and weight of a real hummingbird. The ornithopter weighs 3.3 grams and has a 15 cm wingspan. Currently the world's smallest radio-controlled ornithopter, this one constructed by Petter Muren has a wingspan of 10 cm and weighs only 1 gram.

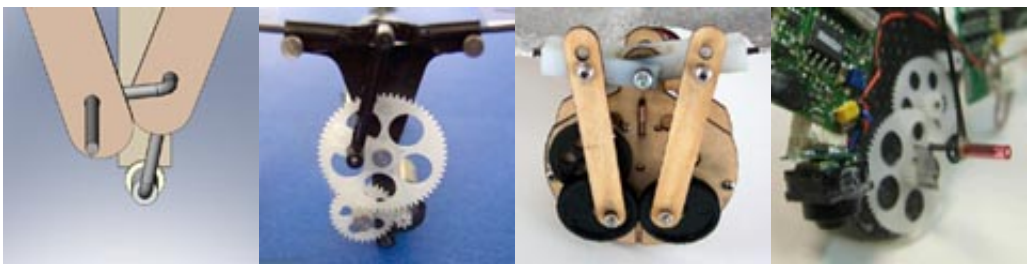

Figure 1.3: State of the art: Crankshaft mechanisms 2000-10. From left: Staggered cranks; Outboard wing hinge; Dual cranks; Transverse shaft cranks

Fig. 1.3[2] lists some of the variations of a crank mechanism used as the primary actuation mechanism in current flapping-wing MAV designs; these are described briefly below:

1. Staggered cranks: The simplest solution is to use a staggered crank. Here, the connecting rods go off at different angles, but their timing is corrected by having them placed on separate crank throws. The staggered crank is most easily constructed from bent wire. This normally is useful in fairly small ornithopters.
2. Outboard wing hinge: If the fabrication methods will not allow a staggered crank, it might be preferrable to separate the two wing hinge lines so that the connecting rods pass together between the wing hinges. Since the angle between the connecting rods is small, the flapping is fairly symmetric.
3. Dual cranks: Another solution is to use two separate cranks; this requires an additional drive shaft and gear. This mechanism will probably weigh a little more than the outboard wing hinge mechanism shown above, but the flapping will be more symmetrical.
4. Transverse shaft: A variation on the dual crank idea is to use a single, transverse drive shaft, with cranks at either end. Since the cranks are not operating in the same plane as the flapping arc, the connecting rods must have ball joints at their ends. This results in more friction compared with ball bearings operating in a single plane.

Table 1.2 and Table 1.3[3] showcase some of the state of the art MAVs that have been developed over the years [6, 15, 25, 45, 48]. At present, a uniformity among most of the MAV designs can be seen from their propulsion / actuation, a variation of a simple reciprocating crankshaft mechanism; symmetric flapping through mechanical coupling to a single rotary actuator; restricted control schemes and low energy efficiency attributed to the use of Frequency Modulated flapping, as opposed to Amplitude Modulation, as used in insect

[2] http://www.ornithopter.org
[3] Adapted from [34]

and bird flight [6, 34, 41, 43]. Elastic storage and reuse of pectoral muscle energy is not facilitated. Complete 6 DoF dynamics attained by addition of an airplane like tail rudder or a tail elevator.

1.5.1 Power To Weight Ratio

For MAVs the power to weight ratio of the power system is extremely critical owing to the fact that the overall aerodynamic efficiencies of conventional fixed-wing vehicles using steady-state analysis tools decreases with size [34]. Also, the efficiency of power/propulsion systems appears to degrade with decreasing size. Presently, the propulsion systems onboard the listed MAVs exhibit mass fractions of over 60% with respect to the GTOW. In contrast, only 16% of a bird's mass is concentrated in muscle matter, used for flapping [34].

1.5.2 Shared Propulsion Characteristics For Present Day MAVs

Although present state of the art designs show tremendous potential and progress in the field, however improvements in actuation/propulsion methodology can still be made to increase energy performance of the systems, enhancing flight time and payload capacities. To begin discussion and analysis of an alternative flapping actuation configuration/mechanism it is important to list the characteristics of present state of the art systems. At present, a uniformity among most of the MAV designs can be seen in the following shared characteristics of their propulsion mechanics and power systems as seen in Table 1.2 and Fig. 1.3.:

1. They all base their propulsion / actuation mechanism on a variation of a simple reciprocating crank-shaft mechanism.
2. The reciprocating mechanism is achieved by driving a four-bar assembly (with the wing as one of the bars) by a rotary actuator.
3. Both the wings are mechanically coupled to the rotary actuator, thereby flapping in unison with each other.

4. The primary thrust capability is delivered by the use of two wings only, actuated by a single rotary actuator.
5. The flapping mechanism though similar to a bird/insect flight, differs in the manner that the elastic storage and re-use of pectoral muscle energy is not facilitated in the design of the system.
6. Fixed Amplitude and Variable Frequency flapping, as opposed to Fixed Frequency and Variable Amplitude (FiFVA) for insect and bird flight[6, 7, 13, 22, 28, 31, 34, 36, 41, 43, 50, 51]. This restricts the control schemes and experimental degrees of freedom.
7. 6 DoF dynamics are achieved by the addition of a tail rudder or a tail elevator, similar to a fixed wing airplane design.

1.6 TRADE STUDY AND PRELIMINARY DESIGN QUALIFICATION

There are basically three types of MAVs: airplane-like fixed-wing models, helicopter-like rotary-wing models and bird or insect-like flapping wing (ornithopter) models. Each type has different advantages and disadvantages. Fixed-wing MAVs can currently achieve higher efficiency and longer flight times, so are well suited to tasks that require extended loitering times and larger ground coverage. Rotary-wings allow hovering and movement in any direction, at the cost of shorter flight time. Flapping wings offer the most potential for miniaturization and maneuverability, but are currently far inferior to fixed wing and rotary wing MAVs. As we go smaller in size, the limitations of fixed and rotary wing technologies become apparent; the Reynolds number decreases with smaller wing surfaces depreciating the performance of airfoils designed for steady state fluid flow observed at high Reynolds numbers (As seen on wings of birds, planes, propeller blades etc). However at low Reynolds numbers, insects and birds have shown promising results. A lot of research in the unsteady Reynolds number has also supported the fact[34]. Thus, the need for a more

efficient flying design is indisputable. The fact remains, that this design has been with us for eons and can be seen all around us.

Insects and birds are the most efficient flyers in our environment, with unmatched dynamics, maneuverability, speed and agility. Their ability to cope with wind turbulence and also varying surrounding environmental conditions is phenomenal; hence the reasoning to mimic their flight dynamics and actuation mechanisms to achieve longer MAV flights with improved dynamics follows coherently.

1.7 BACKGROUND AND STATE OF THE ART

Recent research on MAVs has been greatly inspired by the flight of insects and small birds, due to their extraordinary ability to control flight force in both forward flight and hovering. Theodorsen [49] first derived equations for aerodynamic forces on thin symmetric oscillating airfoils in potential flow for the purpose of predicting aerodynamic flutter. Theodorsen's equations are applicable to flapping flight, but the analysis assumes small oscillation angles and high Reynolds number, and thus the equations may not be applicable for higher-amplitude, low Reynolds number flight of a micro air vehicle [1].

There are also a number of studies of oscillating airfoils (2D more than 3D) and wings using CFD in the literature. Neef and Hummel [32] modeled airfoils in pitching and heaving motion with a constant upstream velocity. Their results matched the results of Theodorsen well, albeit with an aerodynamic phase shift due to unsteady effects. However, this study focused on small to moderate reduced frequencies at high Reynolds number, in which case the Euler equations are valid and the flow can be assumed inviscid. Neef and Hummel also extended their work to 3D studies under the same conditions. Isogai and Shinmoto used CFD to model multiple oscillating airfoils in a dragonfly-like configuration in order to study wake interference effects [17]. Mashraf, et al. used Fluent to model pitching and heaving airfoils over a wide range of flapping frequencies and amplitudes, noting that the laminar flow assumption holds valid even for high frequencies and amplitudes [27]. For efficient

thrust generation, they recommend operating at high frequency but low amplitude, and the research also confirms some predictions of Theodorsen's theory. One study by Liu and Kawachi [26] models the geometry and kinematics of a hawkmoth, which is significantly smaller than the MAV being developed in the current research, and focuses on the role of leading edge vortexes in producing high lift force. The authors deduce that the leading edge vortex may be responsible for the dynamic stall effect which allows wings to operate efficiently at high angles of attack. They hypothesize that this is one of the primary effects allowing insects to fly at very low Reynolds number.

Experimental flapping wing studies are also somewhat rare. This is especially true at low Reynolds number, where the aerodynamic forces are very low and difficult to distinguish from inertial forces, vibration, and noise. Knoller [24] and Betz [3] were the first ones to propose the idea that for a flapping wing there is a normal force vector which results from the combine effect of trust and lift components due an effective angle of attack formed by the oscillating motion of a wing. In this experiment the average thrust force of a stationary airfoil was measured in a sinusoidally oscillating wing stream. Ames, et al. performed experimental studies at Reynolds number as low as 20,000 [1], using smoke for flow visualization and laser velocimetry to measure the flow field. At high frequency, the inertial force made up a significant portion of the measured load and had to be corrected using a dynamic model of the wing. Results were compared with an unsteady panel code, which matched well at high Reynolds number but under-predicted significantly at the lowest Reynolds number studied. Sane and Dickinson [46] used a dynamically scaled model of an insect wing, submersed in oil, to measure forces at very low Reynolds number. This approach has the benefit of amplifying the aerodynamic force but is more complicated and also involves an increased "added mass" inertial force from the denser fluid. This study enforces the fact that the aerodynamic performance of flapping wings depends strongly on wing kinematics; the flapping and feathering amplitudes and frequencies especially have a strong impact on flight performance. In a subsequent study, the same researchers investigated the effects of

wing rotation with the intent of determining how insects maneuver in flight [47].

1.7.1 Biological Species: Flight Comparison

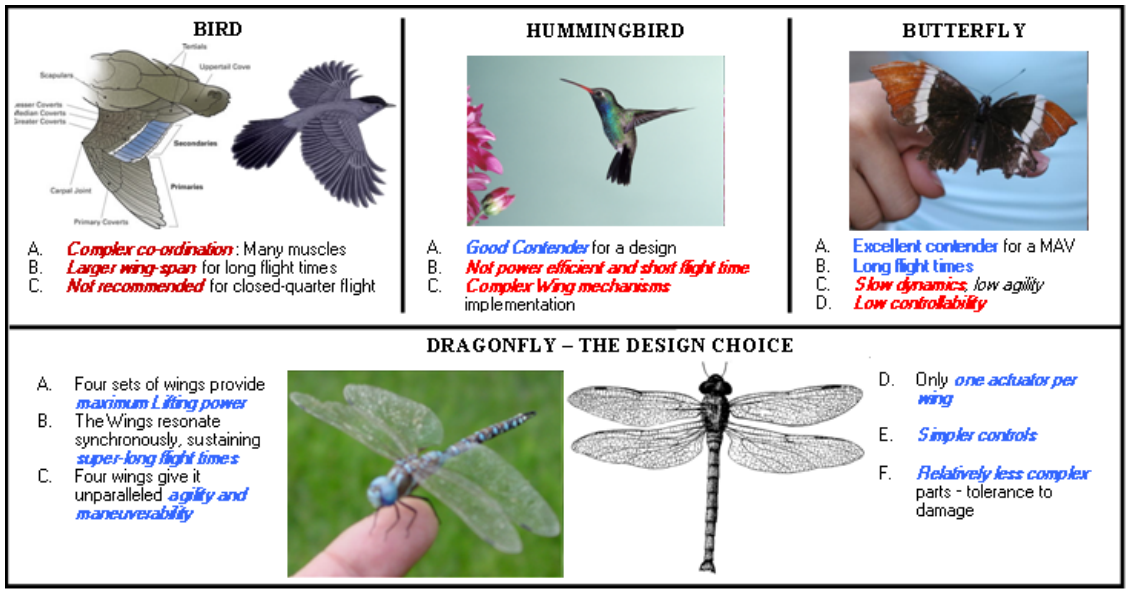

Figure 1.4: Trade study of natural flyers: Insects and Birds

A comparison of the flying mechanism between a bird, a humming bird, a butterfly and a dragonfly was made to choose the optimal MAV design. A dragonfly-like design, as shown in Figure 1.4, was chosen based on the following benefits:

- Four sets of wings provide maximum lifting power – can carry excess payload in the form of sensors and more processing power (Ref. Chapter 2).
- The wings resonate, making it possible to sustain long flight times at minuscule energy requirements (Ref. Chapter 2).
- Four wings provide stable flight performance to environmental disturbances like wind and air gusts (Ref. Chapter 4).

1.8 RESEARCH QUESTIONS AND OBJECTIVES

The research dissertation will address the following research questions and objectives in the following chapters:

1. Chapter I: How do you introduce the research problem? What is the present state of the art in the field?
2. Chapter II: How does a multi-wing MAV design improve upon the energy performance of a 2-wing MAV design? In particular, how will you achieve the following:
   (a) Energy reserve enhancement on-board an MAV for the purposes of longer flight times (enhanced flight endurance).
   (b) Higher payload capacity.
3. Chapter III: How will you show that elastic jointed wings improve power efficiency on MAVs? In particular how will you address the following:
   (a) Theoretical model for torque performance improvement prediction with springs.
   (b) Experimental confirmation of power efficiency improvement with elastic jointed wings.
4. Chapter IV: How will you control the proposed new MAV design to achieve 6DoF flight? In particular, how will you address the following:
   (a) Software simulation / visualization to show flight capability.
   (b) Hardware simulation to show maneuvering capability.

CHAPTER II

ENERGY RESERVE IMPROVEMENT: FOUR-WING DESIGN

2.1 CHAPTER OBJECTIVES

The objectives of this chapter are to address the design/configuration specifications of an MAV propulsion/actuation mechanism (within the constraints of the Definition 1.1), towards meeting the following objectives:

1. Establish a theoretical model for predicting improvement in on-board energy reserves on flapping multi-wing MAVs, leading to higher endurance flights and payload capacities.
2. Perform hardware testing to demonstrate energy reserve improvement resulting in flight time and payload improvement.

2.2 ENERGY RESERVE ENHANCEMENT

The QV design's inherent advantage lies in providing the MAV with a many fold increase in lift and flight time, thus the ability to carry higher payloads in the form of avionics and battery packs and enabling higher endurance flight applications [42]. To describe how energy is saved in a Multi-Wing configuration, we begin by defining the nomenclature in Table 2.1.

Assumption 2.1. The actuators are assumed to have a limit to the maximum lift they can produce, determined by the maximum allowable power rating for safe operation and speed/torque characteristic of the DC motor[1].

[1]DC Motors have a speed/torque curve as a funciton of the input power supply. The assumption is quite reasonable, since a battery input has a hard limit to the maximum voltage it can provide. Considering lithium polymer (LiPo) batteries having high discharge rates, the limitation on the maximum current supply is determined by the voltage-current curves of the actuating motor. Given that the voltage is limited to a maximum value (usually 3.7~4.2V for LiPo batteries), the maximum speed/torque produced by the motor also has a limit.

Table 2.1: Nomenclature

W_{n-MAV}	Weight of n-Wing MAV
$W_{Actuator}$	Weight of Actuator (Including wing-mechanism)
$W_{Battery}$	Weight of the on-board Battery
$W_{Avionics}$	Weight of the on-board Autopilot
$W_{Non-Avionics}$	Weight of Battery, Actuators, wings etc
R_A	Ratio of $W_{Avionics}$ to $W_{Non-Avionics}$
E_{A_N}	Available Energy per Actuator in N-Wing Config.
$E_{Battery}$	Energy Reserve of each Battery
$E_{Avionics}$	Energy Available to the Avionics
D_n	Ratio of W_{n-MAV} to W_{2-MAV}

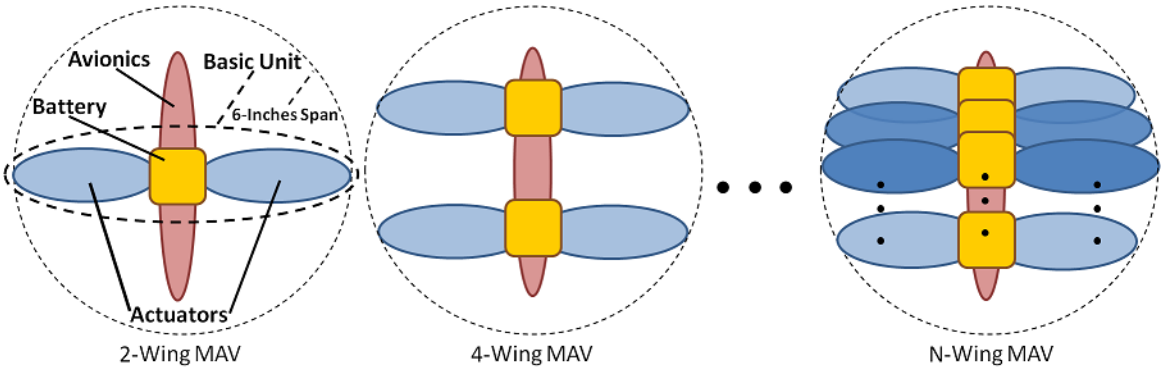

Figure 2.1: 2, 4, N-Wing MAVs: Repeating the Basic Unit

2.2.1 2-Winged Configuration

For a 2-winged configuration, we define the following weight and energy configurations:

$$2 \times W_{Actuator} + W_{Avionics} + W_{Battery} = W_{2-MAV} \tag{2.1}$$

$$2 \times E_{A_2} + E_{Avionics} = E_{Battery} \tag{2.2}$$

So the energy reserves per actuator are given by:

$$E_{A_2} = \frac{1}{2}\left(E_{Battery} - E_{Avionics}\right) \tag{2.3}$$

2.2.2 N-Wing MAV Configuration

Assumption 2.2. The energy consumed / actuator is linearly proportional to the weight of the MAV[2].

The weight configuration for an N-Wing MAV:

$$\frac{n}{2} \times \left(2 \times W_{Actuator} + W_{Battery}\right) + W_{Avionics} = W_{n-MAV} \tag{2.4}$$

$W_{Non-Avionics} = W_{Battery} + 2 \times W_{Actuator}$ is defined as the "Basic Unit"[3,4] seen across different MAV flyers.

[2]It is reasonable to assume linear relationship to describe the input power requirements of the DC actuator for theoretical analysis; however, the relationship will be non-linear in nature. The torque requirement will scale up, when the wings are required to lift a higher mass, as follows intuitively.

[3]Using only one motor to power both the wings together, like in commercially available 2-Wing flyers, requires a bigger motor for the job, so the power and weight increment is equivalent to having two smaller motors powering each wing individually; thus the reasoning to consider one battery and two actuators as a Unit Weight of the MAV.

[4]For Multi-Wing vehicles, multiple copies of the same actuators are used as in the 2-Wing design to better quantify the Power Reserve increase from 2-Wing to Multi-Wing designs.

Assumption 2.3. We consider the worst case scenario: Power intake of actuator is at its breakdown threshold and the MAV is sustaining a constant hover; further increase in MAV weight can not sustain hovering[5].

Assumption 2.4. Input power requirement is proportional to the total weight of the MAV[6].

Hence, the general energy configuration for an N-Wing vehicle:

$$2 \times D_n \times E_{A_n} + E_{Avionics} = \frac{n}{2} \times E_{Battery} \tag{2.5}$$

D_n is dependent on the weight of the MAV. For a 4-Wing configuration having $W_{Avionics}$= 0, $D_4 = 2$. D_n falls in value towards 1 as $W_{Avionics}$ increases, Fig. 2.2. Which clearly implies that the energy reserves per actuator increase in amount as weight of avionics increases on the MAV:

$$D_n = \frac{W_{n-MAV}}{W_{2-MAV}} = \frac{\frac{n}{2} \times W_{Non-Avionics} + W_{Avionics}}{W_{Non-Avionics} + W_{Avionics}} \tag{2.6}$$

So the energy reserves per actuator in general for a Multi-Wing MAV are given by:

$$E_{A_n} = \frac{1}{2 \times D_n} \left(\frac{n}{2} \times E_{Battery} - E_{Avionics} \right) \tag{2.7}$$

We see from Eq. 2.7 that:

[5]This assumption was made to remove the possibility for a 2-Wing MAV to flap faster/larger-amplitude to overcome additional payload on-board. If the payload capacity is limited in such a manner, the increase in payload when moving to a four-wing design can be shown more clearly. This assumption will also hold if the input voltage of the battery has an upper limit; the DC actuator can not generate larger torques when the input power supply is limited to a maximum by voltage.

[6]Torque requirement increase with weight of the MAV, hence the DC actuator would require a higher input power to sustain higher torques at the wing

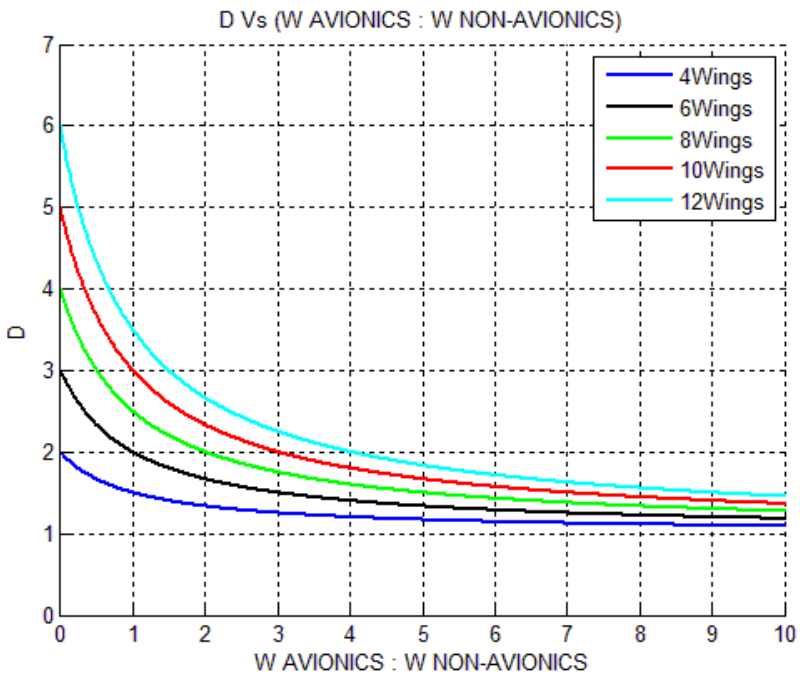

Figure 2.2: Change in Value of D_n with R_A

$$E_{Actuator}|_{n-MAV} \geq E_{Actuator}|_{(n-1)-MAV} \geq \cdots$$

$$\cdots \geq E_{Actuator}|_{4-MAV} \geq E_{Actuator}|_{2-MAV}$$

where, equality is held if $W_{Avionics} = 0$. Practically, this is not possible, since every MAV at bare minimum, needs some electronics to drive the actuators and for remote control operations. Also for an N-Wing MAV,

$$\frac{E_{A_n}}{E_{A_2}} = \frac{1}{D_n}\left(\frac{\frac{n}{2} - \mathrm{E_{Avionics}}/\mathrm{E_{Battery}}}{1 - \mathrm{E_{Avionics}}/\mathrm{E_{Battery}}}\right) \tag{2.8}$$

2.2.3 4-Wing MAV Configuration

For a 4-winged configuration, we define the following weight and energy configurations:

$$4 \times W_{Actuator} + W_{Avionics} + 2 \times W_{Battery} = W_{4-MAV} \tag{2.9}$$

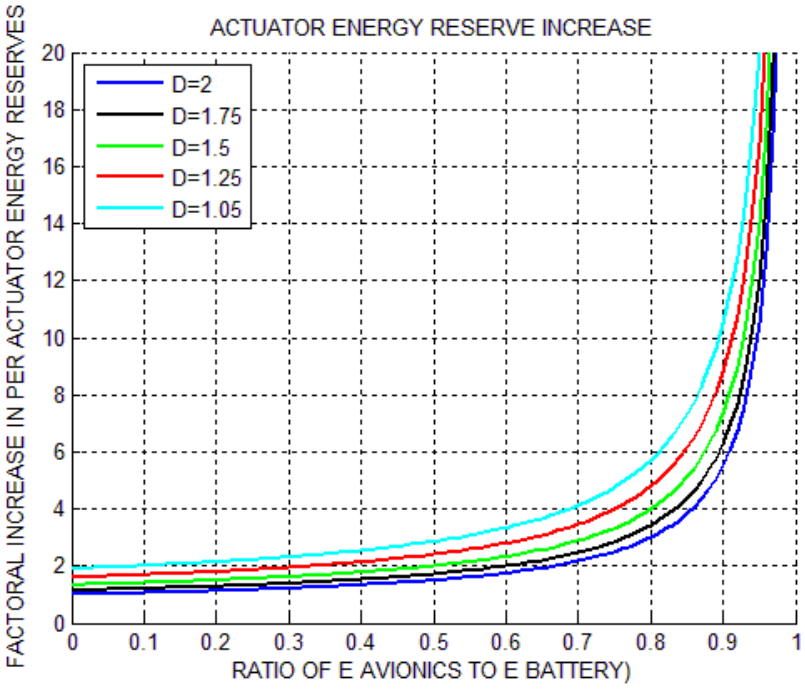

Figure 2.3: Factoral increase of energy reserves of a 4-Wing over a 2-Wing MAV for different weights of avionics

or, $2 \times (2 \times W_{Actuator} + W_{Battery}) + W_{Avionics} = W_{4-MAV}$

We see that:

$W_{4-MAV} = 2 \times W_{2-MAV} - W_{Avionics}$

The energy consumed / actuator is proportional to the weight of the MAV. Higher the weight, higher the energy requirement of the actuator to produce lift.

The energy configuration for the 4-winged MAV is defined by:

$$2 \times D_4 \times E_{A_4} + E_{Avionics} = 2 \times E_{Battery} \tag{2.10}$$

D is dependent on the weight of the MAV. For a four wing configuration having $W_{Avionics}$= 0, $D_4 = 2$ and D falls in value as $W_{Avionics}$ increases; which clearly implies that the energy

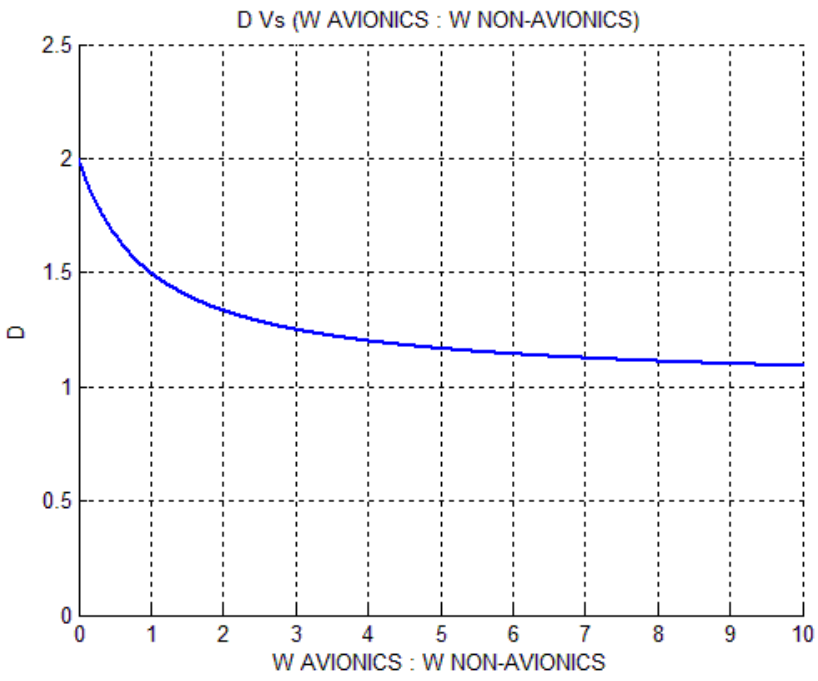

Figure 2.4: Weight of 4-Winged MAV : 2-Winged MAV Vs Avionics Weight : Non-Avionics Weight - D_4 Vs R_A

reserves / actuator increase in amount (in a 4-Wing MAV over a 2-Wing MAV configuration) as weight of avionics increases on the MAV.

The value of D_4 plotted against ratio of $W_{Avionics}/W_{Non-Avionics} = R_A$ is shown in the Fig. 2.4.

From Fig. 2.4, it is clearly seen that the if the weight of the avionics increases in ratio to the weight of the full MAV, then with increasing number of wings the value of D falls towards 1. i.e. the weight of avionics is more significant compared to the weight of non-avionics components of the MAV (Battery, Actuators, wings etc). However, R_A usually lies between 0 and 2 in conventional MAVs and this value is close to 5 and higher for insects [34] (Since avionics also constitute organs and other tissues not directly associated with actuation system).

Assumption 2.5. The number of batteries required for multi-winged vehicles increase linearly with the number of wings of the vehicle. Also for multi-winged vehicles, multiple

copies of the same actuators used on the 2-winged vehicle are multiplied in number[7].

For a 4-Wing configuration, energy reserves / actuator are given by:

$$E_{A_4} = \frac{1}{2 \times D_4} \left(2 \times E_{Battery} - E_{Avionics}\right) \tag{2.11}$$

We see from Equation 2.3 and Equation 2.11 that:

$$E_{Actuator}|_{4-MAV} \geq E_{Actuator}|_{2-MAV} \tag{2.12}$$

where, equality holds if $D_4 = 2$, i.e. $W_{Avionics} = 0$, which is a practical impossibility.

For a 4-winged MAV,

$$\frac{E_{A_4}}{E_{A_2}} = \frac{1}{D_4} \left(\frac{2 - \mathrm{E_{Avionics}/E_{Battery}}}{1 - \mathrm{E_{Avionics}/E_{Battery}}} \right) \tag{2.13}$$

2.2.4 Example Configuration

Example 2.1. If the weight of the avionics, $W_{Avionics}$ **was** $1/4^{th}$ the weight of the MAV, i.e. $\left(W_{Avionics} = \frac{1}{4} W_{2-MAV}\right)$ and the avionics consumed $1/2$ the onboard energy $\left(E_{Avionics} = \frac{1}{2} E_{Battery}\right)$. Then increasing the number of wings from 2 to 4 would result in increase in energy reserves per Actuator by 75%. i.e. the Flight Time of the MAV will increase by 75% (or the payload capacity increases by 75% over the 2-winged MAV).

Example 2.2. If the weight of the avionics, $W_{Avionics}$ **was** $1/2$ the weight of the MAV, i.e. $\left(W_{Avionics} = \frac{1}{2} W_{2-MAV}\right)$ and the avionics consumed $1/2$ the on-board energy $\left(E_{Avionics} = \frac{1}{2} E_{Battery}\right)$.

[7] In LiPo batteries, increasing their capacity results in a linear increase in weight and size. The same linear curve is not followed for actuators, but it is kept so for simplifying analysis.

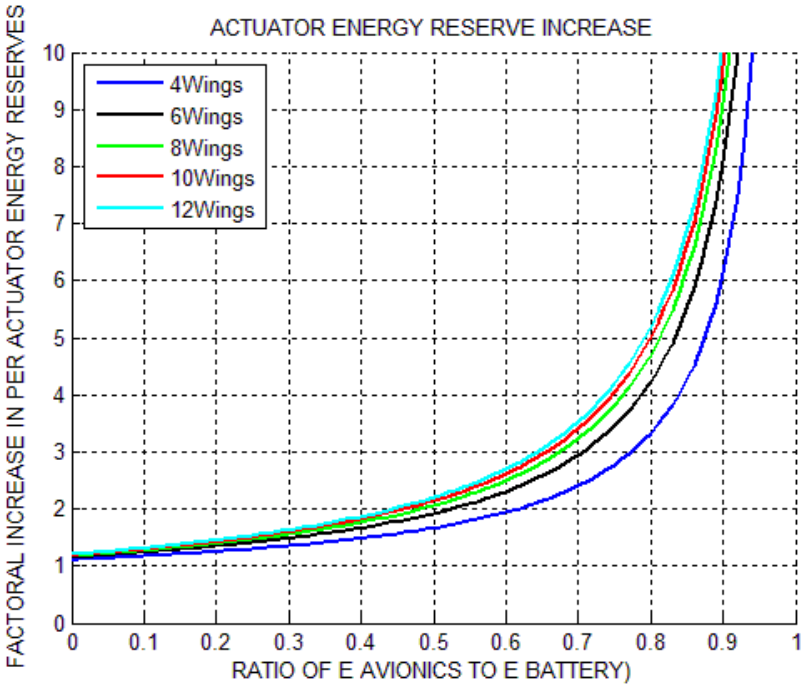

Figure 2.5: Factoral increase of energy reserves of an N-Wing over a 2-Wing MAV for $W_{Avionics} = \frac{1}{2}W_{2-MAV}$

Then from Eq. 2.8, increasing the number of wings from 2 to 4 would result in increase in energy reserves per actuator by 100%. i.e. the flight time of the MAV will increase by 100%.

Example 2.3. Let the avionics weight, $W_{Avionics} = \frac{1}{2}(2 \times W_{Actuator} + W_{Battery})$, also let the avionics consume 50% the energy of a single Battery $\left(E_{Avionics} = \frac{1}{2}E_{Battery}\right)$, then the increase in energy reserves for an N-Wing over a 2-Wing configuration is 66.7% (4 Wing), 92.3% increase (6 Wing), 105.9% (8 Wing), 114.3% (10 Wing), 120.0% (12 Wing). However, the energy reserves and hence increase in flight time/on-board payload capacity saturates eventually if wings are simply increased in number, as is illustrated in the Fig. 2.6.

Equations 2.6 and 2.8 together show that the payload increase for multi-winged MAVs follows the same trend as in Fig. 2.6 and saturates with increasing number of wings.

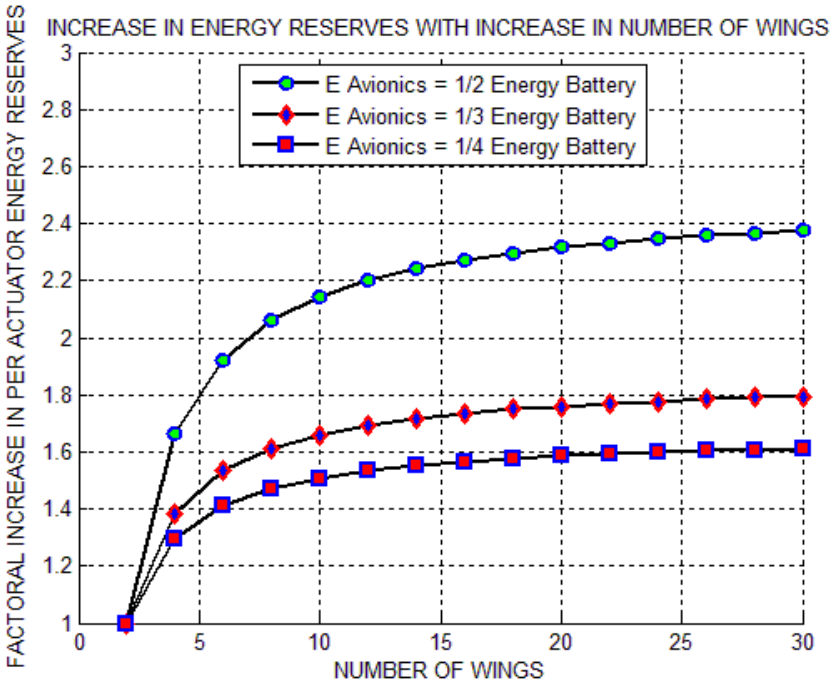

Figure 2.6: Energy Saving / Flight Time Increase Curves

2.3 HARDWARE TESTING AND RESULTS

The four-wing configuration is as shown in Fig. 2.7.

2.3.1 Flight Payload and Power Consumption Comparison

2.3.1.1 Input Power Required for Lift

Example 2.4. The Weight of the Avionics, $W_{Avionics}$ **was** $1/2$ the weight of the MAV, i.e. $\left(W_{Avionics} = \frac{1}{2}W_{2-MAV}\right)$ and the avionics consumed $1/2$ the on-board energy $\left(E_{Avionics} = \frac{1}{2}E_{Battery}\right)$. Then from Eq. 2.8, increasing the number of wings from 2 to 4 would result in increase in energy reserves / actuator by 100%. i.e. the Flight Time of the MAV will increase by 100%.

Exercise 2.1. Experimental Testing was carried out with the following configuration and power settings:

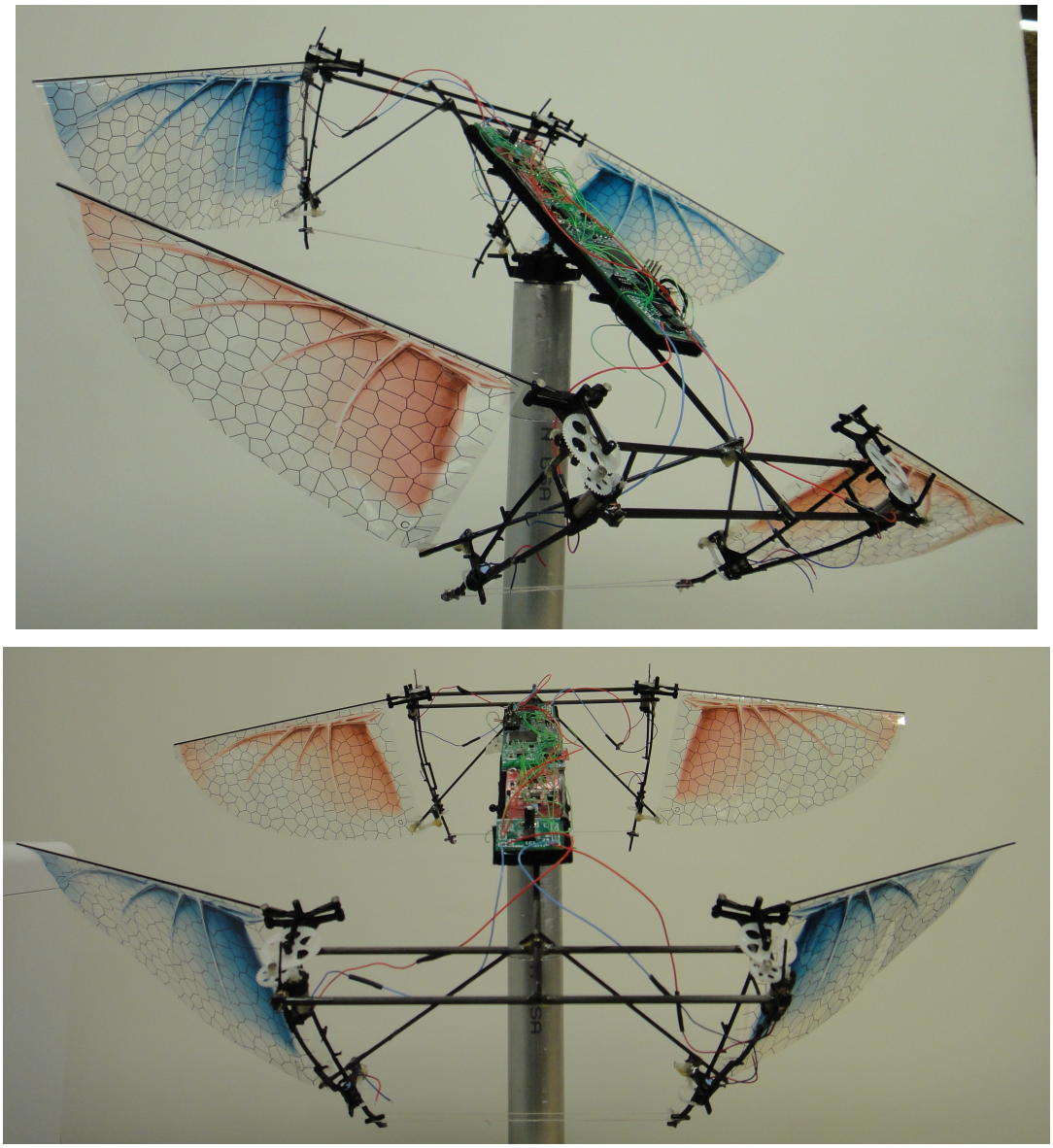

Figure 2.7: 3DoF Benchtop Prototype

Table 2.2: Experiment 1: Configuration and Results

Specifications	Requirements	Details
2-Wing MAV Weight (Incl. Battery)	~30g	Weight of the MAV without electronics
Power Input (MAV) - Actuators only (Two Actuators)	0.48A @ 3.7V = 1.8W	Power Consumed in Lifting its own weight
Energy Reserve of One Battery (2-Wing MAV)	150mAH @ 3.7V = 555mWH	Total Available Power Reserve
Autopilot Weight	~15g	Sensors, Processors, Wireless Transceiver, etc
Power Input (Autopilot)	853mW = 0.853W	Under Nominal Operating Conditions
Time of Operation (2-Wing MAV)	**10min 56s**	**Maximum flight time**
4-Wing MAV Weight (Incl. Battery)	~68g	Weight of the MAV without electronics
Power Input (MAV) - Actuators only (Four Actuators)	0.76A @ 3.7V = 2.8W	Power Consumed in Lifting its own weight
Energy Reserve of Two Batteries (4-Wing MAV)	300mAH @ 3.7V = 1.1WH	Total Available Power Reserve
Time of Operation (4-Wing MAV)	**18min**	**Maximum flight time**
Payload Increase (4-Wing MAV)	**31grams**	**Keeping Flight time equal to 2-Wing MAV**

The performance was measured against the Example 2.2. The MAV was powered at full power (All motors were running at maximum input power - Full Battery Voltage) and the MARC-II Autopilot (Appendix A.4) was running and performing wireless transmission as well.

As can be seen from the Experimental Results, the flight endurance of the four wing MAV having the same autopilot and repeating the same "Basic Unit", the flight time was increased from ~11min to 18min = 65%. The theoretically predicted flight time increase was 100%. The mismatch can be attributed to the fact that the weight of the MAV varied when switching from a 2 Wing model to the 4-Wing model. The increase in chassis weight was unaccounted for. Also the weight of the MAV increased from 30grams (2 Wing version) to 68grams (4 Wing Version). By estimating, using the predicted offset seen from the results, it was predicted that the flight time increase would rise to 83% if the weight was exactly

doubled (60 grams instead of 68 grams). The difference can further be attributed to the fact that the power intake of the autopilot was also increased slightly owing to the fact that in case of the 4-Wing prototype, the autopilot required "Two Extra" Motor drives, which consumed more energy, hence power intake of the autopilot was somewhat increased over its 2-Wing Counterpart. Other experimental deviations were not explored, however the results were very convincing.

Example 2.5. The Weight of the Avionics, $W_{Avionics}$ **was** $1/4^{th}$ the weight of the MAV (this was achieved by applying an anti-gravity pull on the whole MAV of about 7.5grams using a simple pulley system), i.e. $\left(W_{Avionics} = \frac{1}{4}W_{2-MAV}\right)$ and the avionics consumed $1/2$ the onboard energy $\left(E_{Avionics} = \frac{1}{2}E_{Battery}\right)$. Then increasing the number of wings from 2 to 4 would result in increase in energy reserves / actuator by 75%. i.e. the Flight Time of the MAV will increase by 75% (or the Payload capacity increases by 75% over the 2-winged MAV).

Exercise 2.2. Experimental Testing was carried out with the following configuration and power settings:

The performance was measured against the Example 2.1. The MAV was powered at full power (All motors were running at maximum input power - Full Battery Voltage) and the MARC-II Autopilot (Appendix A.4) was running and performing wireless transmission as well.

Again the result was a jump from 13 min 54 seconds to a flight time of 21min 10s, i.e. 52.3% increase in Flight time. The deviation from the theoretical value of 75% can be explained as before. But consistently the result was always an increase in flight time. Also it was seen that the payload increase by keeping the flight time constant was approximately 31grams in Experiment 1 and 24grams in Experiment 2 while keeping flight time constant, which is approximately 69% and 54% respectively, which matches very closely to the Flight Time Increase values of 65% and 52.3% respectively.

Table 2.3: Experiment 2: Configuration and Results

Specifications	Requirements	Details
2-Wing MAV Weight (Incl. Battery)	~30g	Weight of the MAV without electronics
Power Input (MAV) - Actuators only (Two Actuators)	0.42A @ 3.7V = 1.56W	Power Consumed in Lifting its own weight
Energy Reserve of One Battery (2-Wing MAV)	150mAH @ 3.7V = 555mWH	Total Available Power Reserve
Autopilot Weight	~7.5g	Sensors, Processors, Wireless Transceiver, etc
Power Input (Autopilot)	853mW = 0.853W	Under Nominal Operating Conditions
Time of Operation (2-Wing MAV)	**13min 54s**	**Maximum flight time**
4-Wing MAV Weight (Incl. Battery)	~68g	Weight of the MAV without electronics
Power Input (MAV) - Actuators only (Four Actuators)	0.76A @ 3.7V = 2.26W	Power Consumed in Lifting its own weight
Energy Reserve of Two Batteries (4-Wing MAV)	300mAH @ 3.7V = 1.1WH	Total Available Power Reserve
Time of Operation (4-Wing MAV)	**21min 10s**	**Maximum flight time**
Payload Increase (4-Wing MAV)	**24grams**	**Keeping Flight time equal to 2-Wing MAV**

2.4 CHAPTER CONCLUDING REMARKS

The energy reserve increase in Multi-Wing designs is theoretically predicted to be quite significant, spanning to even 400% and above over that shown by a 2-Wing configuration. The energy reserve improvement was shown for the QV design. It was seen that the 4-Wing MAV was able to produce almost 83% (Theoretical value was 100%) flight time improvement over a 2-Wing configuration when the autopilot weight was 1/2 the weight of the MAV and the improvement was 55% (Theoretical value was 75%) when the autopilot weight was 1/4th the weight of the MAV. The payload increase was seen to follow the Energy Reserve increase very closely. A Four-Wing design was shown to indeed improve upon the energy reserves available on a 2-Wing MAV configuration. The hardware experimentation was carried out to compare against the theoretically predicted values. The discrepancy can be explained by the fact that weight increase due to chassis elements was not considered when moving from 2-Wing to a 4-Wing configuration. Also, the increase in weight of additional wiring for the additional motor drivers and the one additional battery wasn't considered in the theoretical model. Within the limitations of the model, the experimental results matched theoretically predicted values reasonably well.

The following chapter addresses the torque reduction and power efficiency improvement by the use of elastic jointed wings.

CHAPTER III

ENERGY EFFICIENCY IMPROVEMENT: ELASTIC JOINTED WINGS

3.1 CHAPTER OBJECTIVES

The objectives of this chapter are to address the design/configuration specifications of an MAV propulsion/actuation mechanism (within the constraints of the Definition 1.1), towards meeting the following objectives:

1. Establish a theoretical model for predicting output torque increase of non-spring-wing configurations over spring-wing configurations.
2. Illustrate and compare various hardware platforms built to conform to resonance flapping/actuation.
3. Perform hardware testing of elastic jointed wings and measure input power efficiency improvement over non-elastic jointed wings.

Energy efficiency on the QV design goes beyond that provided by the Four-Wing configuration over a Two-Wing configuration alone; the inclusion of elastic/restorative wing flapping further improves the energy efficiency of the MAV.

The dynamics of the wing-spring combination can be stated as in Eq. 3.1. The flapping wing configuration is shown in Fig. 3.1.

$$J(\theta)\ddot{\theta} + b\dot{\theta} + K\theta = \tau_{External} \tag{3.1}$$

$J(\theta)$ is the inertia of the wing-limb system; b is the damping constant of the 2^{nd}order system; K is the spring constant of the system. $\dot{\theta}$ is the angular velocity of the wing. The system is a driven harmonic oscillator.

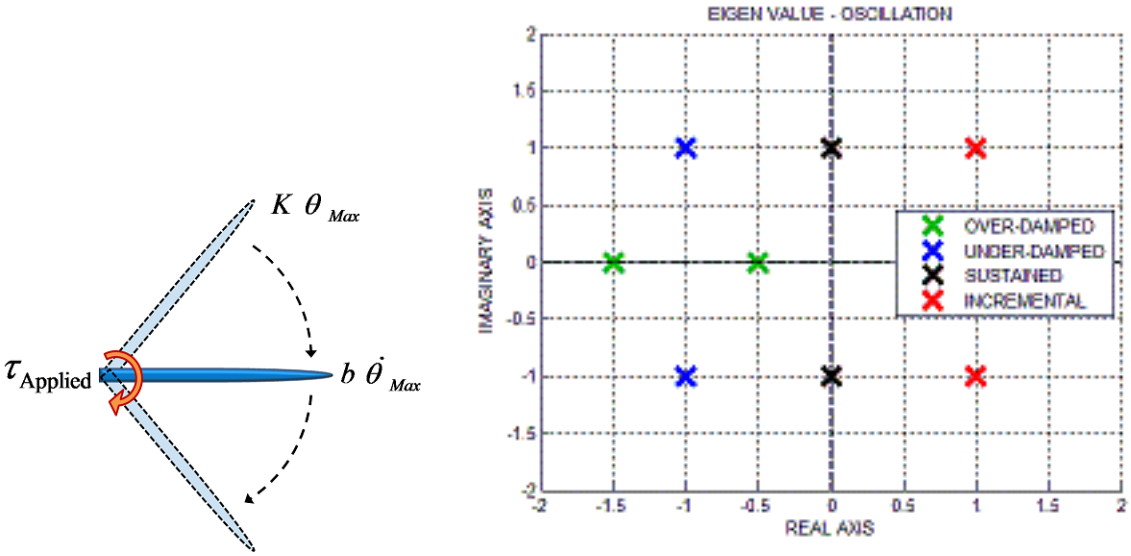

Figure 3.1: Wing System (Left), Eigenvalue Plot (Right)

Assumption 3.1. To simplify dynamics, the non-linear dependence of damping on $\dot{\theta}^2$ has been reduced to a linear dependence $\dot{\theta}$ as shown in Eq. 3.1[1].

3.1.1 State Space Representation

The joint dynamics of the wing, spring and external actuation, stated in Eq. 3.1 have been converted to state space substituting $x_1 = \theta$, $\dot{x}_1 = \dot{\theta} = x_2$ and $\dot{x}_2 = \ddot{\theta}$, giving:

$$\begin{bmatrix} \dot{x}_1 \\ \dot{x}_2 \end{bmatrix} = \begin{bmatrix} 0 & 1 \\ -\frac{K}{J} & -\frac{b}{J} \end{bmatrix} \begin{bmatrix} x_1 \\ x_2 \end{bmatrix} + \begin{bmatrix} 0 \\ \frac{\tau_{Ext}}{J} \end{bmatrix} \tag{3.2}$$

Or Equivalently, $\dot{X} = AX + BU$,

3.1.1.1 Eigenvalue (λ_i) Characteristics

1. $b^2 > 4KJ$, λ_i are real and negative (Fig. 3.1, green crosses)≡Wing system is stable, over-damped; no oscillations.

[1]The dependence on angular velocity is assumed to be a first-order relationship in aerodynamics study, when the angular velocity is small in value. In the presented case, although the relationship is second order proportional but analysis is simplified by considering a first order linear differential equation.

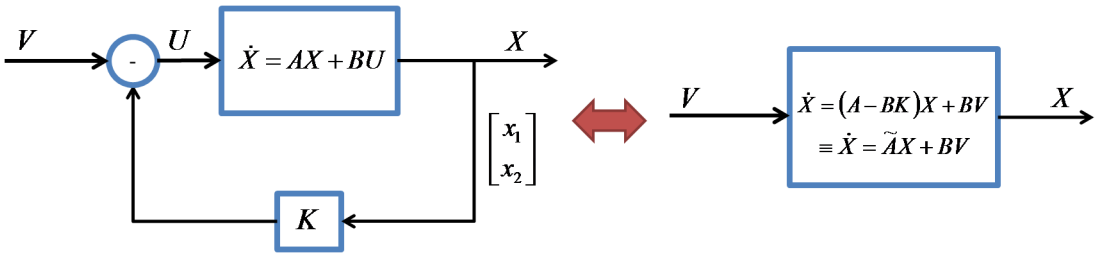

Figure 3.2: State Feedback Control of the MAV wing

2. $b^2 < 4KJ$, eigenvalues are a complex conjugate pair with negative real part (Fig. 3.1, blue crosses)≡Wing system is stable, under-damped; damped oscillations.
3. $b = 0$, (no air drag), λ_i are complex conjugate, $Re(\lambda_i) = 0$ (Fig. 3.1, black crosses)≡The system exhibits undamped, sustained oscillations.

3.1.1.2 State Feedback Control

The goal is to provide a state feedback to the system in the form of an external torque $\tau_{External}$, to overcome the air-drag (damping) on the wing. Thus if damping can be removed, sustained wing oscillations (flapping) can be produced. Towards that goal, an external Torque $\tau_{External}$, is required to make $Re(\lambda_i)$ more positive to increase energy buildup or amplitude increment. For $Re(\lambda_i) = 0$, the oscillations are sustained with no change. For performing maneuvers, the eigenvalues of the individual wings would need to switch between right and left half planes in real time. The State Feedback can be expressed in the form of Eq. 3.3.

$$\dot{X} = AX + BU|_{U=-KX} = \begin{bmatrix} 0 & 1 \\ -\frac{K}{J} & -\frac{b}{J} \end{bmatrix} \begin{bmatrix} x_1 \\ x_2 \end{bmatrix} + \begin{bmatrix} 0 \\ \frac{1}{J} \end{bmatrix} (\tau_{Ext}) \tag{3.3}$$

Choice for feedback gain is $K = \begin{bmatrix} 0 & -\tau_{Ext}/x_2 \end{bmatrix}$ with $\tau_{Ext} = bx_2$ results in the state space

equation becoming:

$$\begin{bmatrix} \dot{x}_1 \\ \dot{x}_2 \end{bmatrix} = \begin{bmatrix} 0 & 1 \\ -\frac{K}{J} & 0 \end{bmatrix} \begin{bmatrix} x_1 \\ x_2 \end{bmatrix} + \begin{bmatrix} 0 \\ \frac{1}{J} \end{bmatrix} V \tag{3.4}$$

Complex Conjugate eigenvalues - Sustained oscillations:

$$\lambda = \pm i\sqrt{\mathrm{K}/\mathrm{J}} \tag{3.5}$$

Conventional flapping systems without the springs ($K = 0$), can be shown to have $\lambda_i = 0, -\mathrm{b}/\mathrm{J}$ (no oscillations); hence have to be driven by external reciprocating torque. The torque equation at the wing joint can be written as $\tau_{ext} = \tau Sin(\omega t)$

$$\begin{aligned} J\ddot{\theta}_1 &= \tau_{1-ext} - b\dot{\theta} - K\theta \\ J\ddot{\theta}_2 &= \tau_{2-ext} - b\dot{\theta} \end{aligned} \tag{3.6}$$

where, τ_{1-Ext} and τ_{2-Ext} are the external torques applied to the wing joint with and without a spring respectively, though the motion profile for the same amplitude should follow the same sinusoidal form;

thus $\ddot{\theta}_1 = \ddot{\theta}_2$.

From Eq. 3.6 we get $\tau_{2-ext} = \tau_1 - K\theta$, but, $\tau_{1-Ext} = b\dot{\theta}$, so we have:

$$\tau_{2-ext} = b\dot{\theta} - K\theta \tag{3.7}$$

For zero air-drag, no-spring the torque required at the wing joint will be equal to $\tau = K\theta$. This is shown as the black solid line, Fig. 3.3. By taking the modulus of this sine wave,

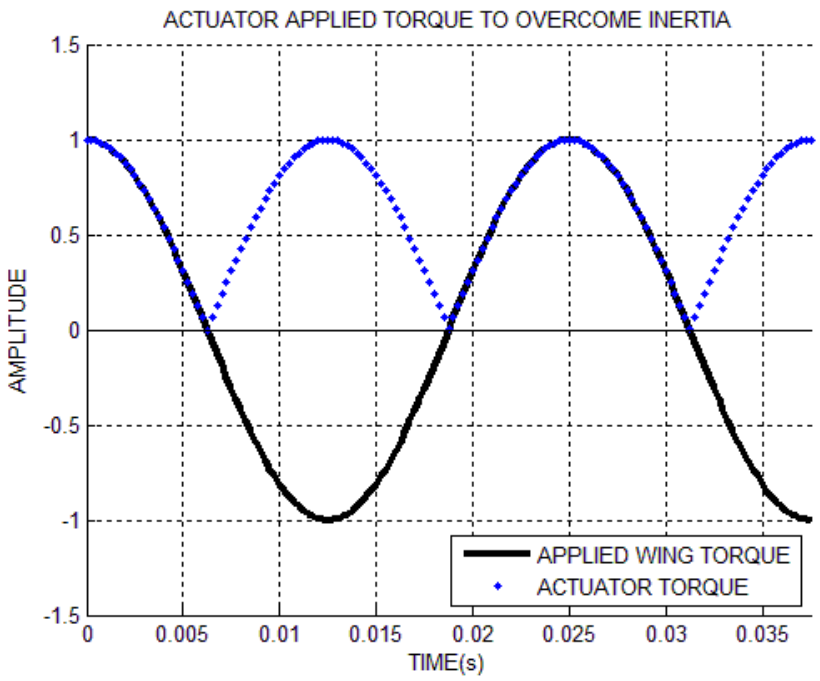

Figure 3.3: Torque profile over Time period T, for the wing-spring system with no damping

we can compute the torque required to be provided by the actuator to sustain wing flapping (blue dotted line, Fig. 3.3)

The average torque required to produce a spring like sinusoidal motion without air damping over one full cycle is given as:

$$\frac{1}{T}\int_0^T K\theta_{max} Sin(\omega t)\, dt = \frac{4}{T}\int_0^{T/4} K\theta_{max} Sin\left(\frac{2\pi}{T}t\right) dt$$

$$= \frac{4K\theta_{max}}{T}\left(\frac{T}{2\pi}\right)\left[-\cos\left(\frac{2\pi}{T}t\right)\right]_0^{T/4} = \frac{2K\theta_{max}}{\pi}$$

Similarly the average torque required with the spring over one full cycle is given as:

$$\frac{1}{T}\int_0^T b\dot{\theta}_{max} Sin(\omega t)\, dt = \frac{2b\dot{\theta}_{max}}{\pi}$$

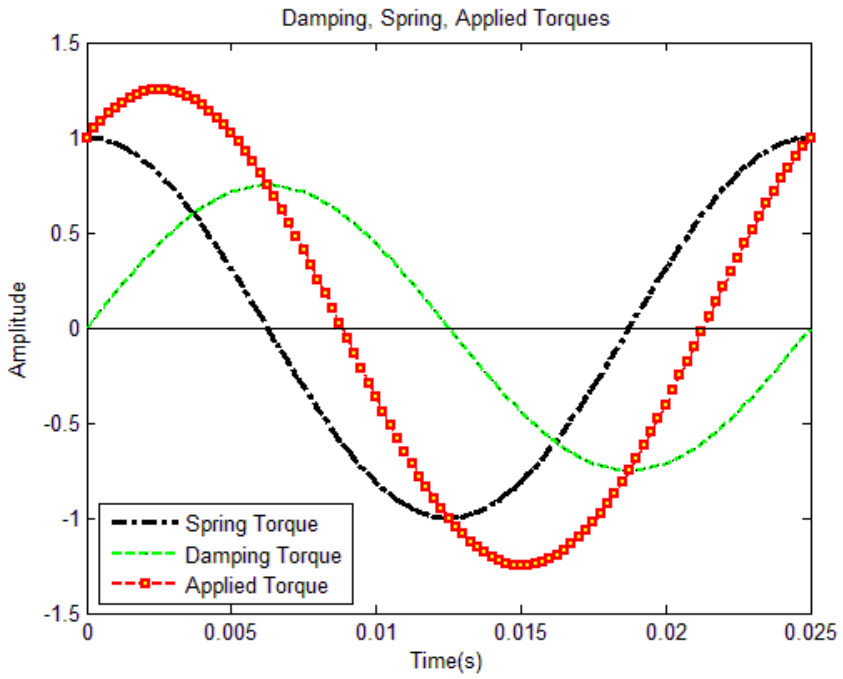

Figure 3.4: No Spring: Torque profiles at wing hinge

Since Damping Torque $\propto$ Angular Velocity ($\dot{\theta}$), hence it has a phase lead of 90^0 over Spring Torque. The effective torque on the system is determined by the addition of sines:

$$\tau_{2-Ext} = b\dot{\theta}_{max}Cos(\omega t) + K\theta_{max}Cos\left(\omega t - \frac{\pi}{2}\right)$$

The addition of two sinusoidal waves with the same frequency but different amplitudes and different phases is given by:

$$A_1Cos(\omega t + \phi_1) + A_2Cos(\omega t + \phi_2) = Re\left\{A_1e^{i\phi_1}e^{i\omega t}\right\} + Re\left\{A_2e^{i\phi_2}e^{i\omega t}\right\}$$

$$= Re\left\{A_1e^{i\phi_1}e^{i\omega t} + A_2e^{i\phi_2}e^{i\omega t}\right\} = Re\left\{\left(A_1e^{i\phi_1} + A_2e^{i\phi_2}\right)e^{i\omega t}\right\} = Re\left\{\left(A_3e^{i\phi_3}e^{i\omega t}\right)\right\}$$

$$= A_3cos(\omega t + \phi_3)$$

where,

$$A_3^2 = A_1^2 + A_2^2 + 2A_1A_2cos(\phi_1 - \phi_2)$$

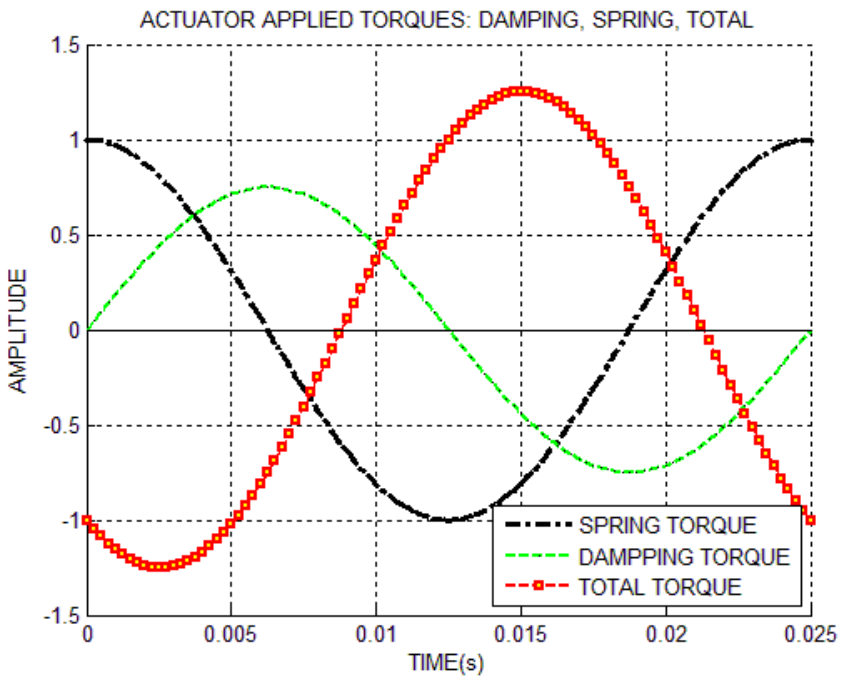

Figure 3.5: No Spring: External torque required at wing hinge (Red)

$\phi_3 = atan\left(\frac{A_1 Sin\theta_1 + A_2 Sin\theta_2}{A_1 Cos\theta_1 + A_2 Cos\theta_2}\right)$

Hence we get for our system, a new sinusoid of the form:

$$\tau_{2-Ext} = \sqrt{(K\theta_{max})^2 + (b\dot{\theta}_{max})^2} Cos\left(\omega t + atan\left(-\frac{K\theta_{max}}{b\dot{\theta}_{max}}\right)\right) \tag{3.8}$$

$$\tau_{2-Ext} = A_3 Cos\left(\omega t + \phi_3\right) \tag{3.9}$$

where, $A_3 = \sqrt{(K\theta_{max})^2 + (b\dot{\theta}_{max})^2}$, $\phi_3 = atan\left(-\frac{K\theta_{max}}{b\dot{\theta}_{max}}\right)$

Calculating also, the average torque without the spring

$$\tau_{2-Ext}|_{Avg} = \frac{1}{T}\int_0^T A_3 Cos\left(\omega t + \phi_3\right) dt$$

$$\tau_{2-Ext}|_{Avg} = \frac{2A_3}{\pi} \tag{3.10}$$

when $b\dot{\theta} = 0,\ \tau_{2-Ext}|_{Avg} = \frac{2K\theta_{max}}{\pi}$,

when $b\dot{\theta} = K\theta_{max},\ \tau_{2-Ext}|_{Avg} = \frac{2\sqrt{2}K\theta_{max}}{\pi}$ (by sine addition).

The equations above gives the average torque required at the wing joint. However, two different cases exist: First, the spring is not used and Second, the spring is used.

3.1.2 Spring Not Used

3.1.2.1 Underdamped or Critically Damped System (i.e. $\left|b\dot{\theta}_{max}\right|$ is $\leq |K\theta_{max}|$),

The average torque required at the wing joint to produce reciprocating wing flapping and generate the desired lift will be $\tau_{2-Ext}|_{NO-Spring}$, given by Eq. 3.11; where the left equality holds at Zero-Damping and the right equality holds at Critical-Damping

$$\frac{2K\theta_{max}}{\pi} \leq \tau_{2-Ext}|_{NO-Spring} = \frac{2A_3}{\pi} \leq \frac{2\sqrt{2}K\theta_{max}}{\pi} \tag{3.11}$$

3.1.2.2 Overdamped System (i.e. $\left|b\dot{\theta}_{max}\right|$ is $> |K\theta_{max}|$,

The average torque required at the wing joint to produce reciprocating wing flapping and generate the desired lift will be:

$$\tau_{2-Ext}|_{NO-Spring} > \frac{2\sqrt{2}K\theta_{max}}{\pi} \tag{3.12}$$

3.1.3 Spring Used

3.1.3.1 Underdamped or Critically Damped System (i.e. $\left|b\dot{\theta}_{max}\right|$ is $\leq |K\theta_{max}|$,

The average torque required at the wing joint to produce reciprocating wing flapping and generate the desired lift will be:

$$\tau_{2-Ext}|_{Spring} = \frac{2b\dot{\theta}_{max}}{\pi} \leq \frac{2K\theta_{max}}{\pi} \tag{3.13}$$

$$\Rightarrow 0 \leq \tau_{2-Ext}|_{Spring} \leq \frac{1}{\sqrt{2}}\, \tau_{2-Ext}|_{NO-Spring} \tag{3.14}$$

The equality on the left holds when damping = 0, implying no external torque requirement. The equality on the right holds when the system is critically damped; at which situation the non-spring system needs about 41.4% more torque to sustain flapping than the system with the spring.

3.1.3.2 Overdamped System (i.e. $\left|b\dot{\theta}_{max}\right|$ is $> |K\theta_{max}|$,

The average torque required at the wing joint to produce reciprocating wing flapping and generate the desired lift will be:

$$\tau_{2-Ext}|_{NO-Spring} > \tau_{2-Ext}|_{Spring} = \frac{2b\dot{\theta}_{max}}{\pi} > \frac{2K\theta_{max}}{\pi}$$

The torque required even in over-damped cases will be higher without the spring, but will progressively become equal to the spring case, as damping increases towards ∞.

A system using non-rotary to reciprocating flapping mechanism would require an additional average torque $\triangle\tau_{2-Ext}$, as compared to the same system with a spring jointed wing:

$$\triangle\tau_{2-Ext} = \frac{2\sqrt{(K\theta_{max})^2 + \left(b\dot{\theta}_{max}\right)^2}}{\pi} - \frac{2b\dot{\theta}_{max}}{\pi} \tag{3.15}$$

Example 3.1. Increase in Energy (%): At a value of $b\dot{\theta}_{max} = \frac{1}{2}K\theta_{max}$, the driving torque ($\triangle\tau_{2-Ext}$) becomes: $\frac{2K\theta_{max}\sqrt{1.25}}{\pi} = 2.2361\frac{K\theta_{max}}{\pi}$, which is 123.61% higher than the torque (and consequently energy) required for the same system with a spring, but no air-damping. The efficiency increase can be even higher (Fig. 3.6) for some systems.

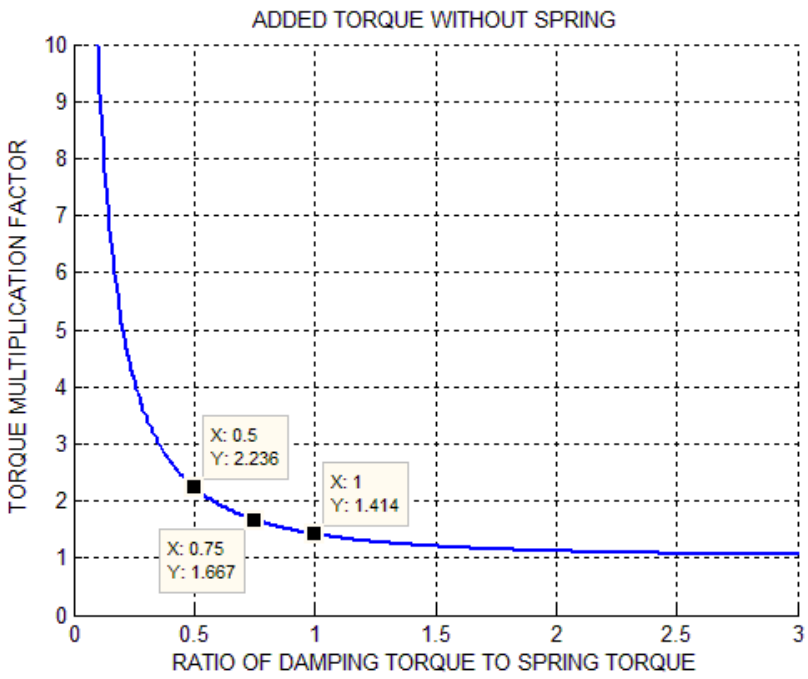

Figure 3.6: No-Spring Torque : Spring Torque vs damping

Assumption 3.2. Relationship of output torque to actuator power-intake is linear[2].

3.2 FIXED FREQUENCY, VARIABLE AMPLITUDE

Definition 3.1. *Fixed Frequency, Variable Amplitude (FiFVA) Control Problem*_-An actuation mechanism converting a rotary motion to reciprocating motion, by the use of a crank mechanism exhibits a low efficiency state. The wing amplitude is always constant, and thus the system can accelerate or decelerate based on how fast the wings are flapping (Frequency Modulation). But for a fixed frequency flight system (insects/birds), changing flapping frequency disturbs the spring-mass system dynamics, resulting in more energy consumption and poor performance [6, 7, 12, 13, 22, 31, 34, 36, 41, 43, 50, 51]. Hence most of the state of the art MAVs to date do away with the spring altogether, thereby losing a lot of flight performance exhibited by birds and insects.

[2]Assumption is made for simplifying analysis, however the dependence is not linear and a non-linear model can be substituted in place of the linear dependance in future work for better accuracy

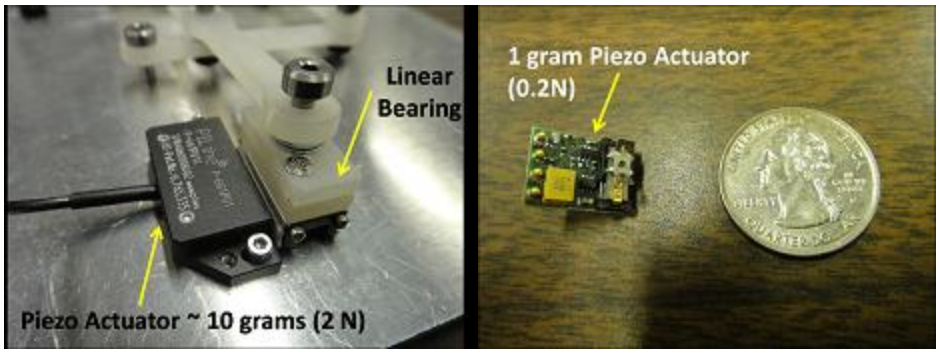

Figure 3.7: Ultrasonic Piezoelectric Linear Actuators

The QV design goal is to implement elastic/resonating actuation mechanisms to improve energy efficiency of flapping mechanics [39]. The challenges in producing FiFVA systems include weight/size issues, mechanical design & coupling issues, scalability and power efficiency $(Power_{output}/Power_{input})$ considerations. This chapter illustrates a compendium of our FiFVA actuation efforts towards achieving resonance flapping. A cumulative comparison chart for all the mechanisms presented herein is given in the concluding remarks for the chapter.

3.3 WING RESONANCE ACTUATION MECHANISMS

3.3.1 Linear Actuator - Four Bar Linkage

The linear actuators (Fig. 3.7) used in the following designs are small ultrasonic, piezoelectric actuators (Replaced over solenoidal linear actuation due to better torque outputs). The actuators provided the required linear force capabilities, but were not very robust to high frequency switching motion due to some reasons: tuning difficulties, low switching bandwidth (less than 15Hz) and weight (10 g).

3.3.1.1 Hard Linkage

A four-bar linkage[3] as shown in Fig. 3.8 and Fig. 3.9 with torsional and extension springs at the wing base mechanically hard couples the actuator to the wing. The system is kine-

[3]The work on the four-bar benchtop prototypes was done with the help of Thomas D. Pappas and Andrew Punnoose

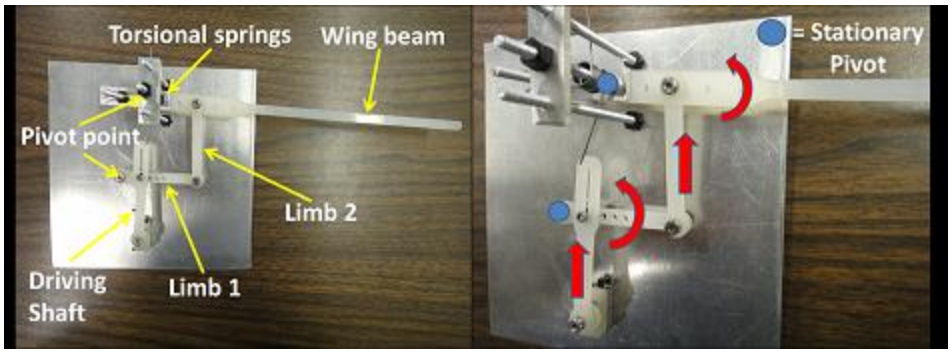

Figure 3.8: Four-Bar (Hard) Linkage Mechanism with Torsional Spring

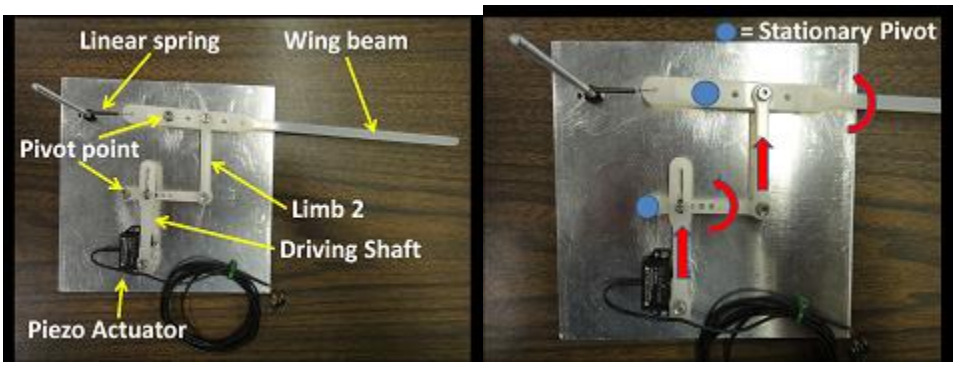

Figure 3.9: Four-Bar (Hard) Linkage Mechanism with Extension Spring

matically constrained to move as explained in Equations 4.4 and 4.24. The extension spring provided less friction and mechanical parts than the torsional spring, but their extension is non-linearly related to the wing deflection.

3.3.1.2 Soft Linkage

The four bar mechanism was also adapted to a soft contact system as shown in Fig. 3.10 to decouple it from the linear actuator. The decoupling provides the means to extend amplitude of the wing flap beyond that kinematically possible by the Hard Linkage. The soft coupling also isolates the actuator and wing to some extent from each other from environmental disturbances on the wing and mis-actuation/functional-irregularity by the actuator.

Remark 3.1. In general converting a linear actuation into a reciprocating-rotary actuation was given up since the inclusion of additional links and limbs to convert linear motion to reciprocating-rotary increased system weight, friction and mechanical complexity. Ad-

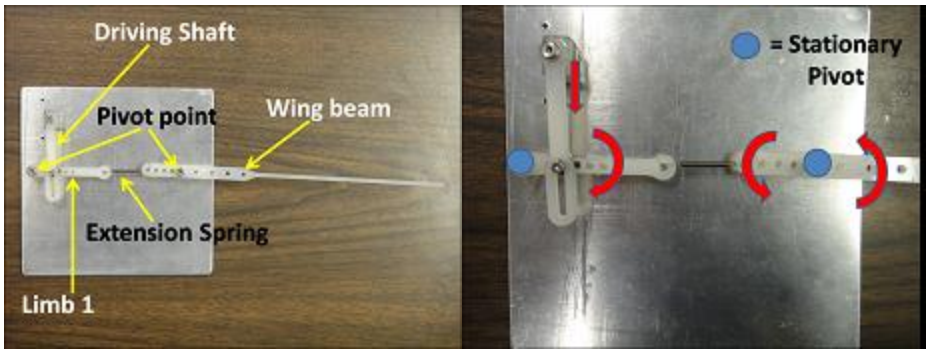

Figure 3.10: Four Bar (Soft) Linkage Mechanism with Extension Spring

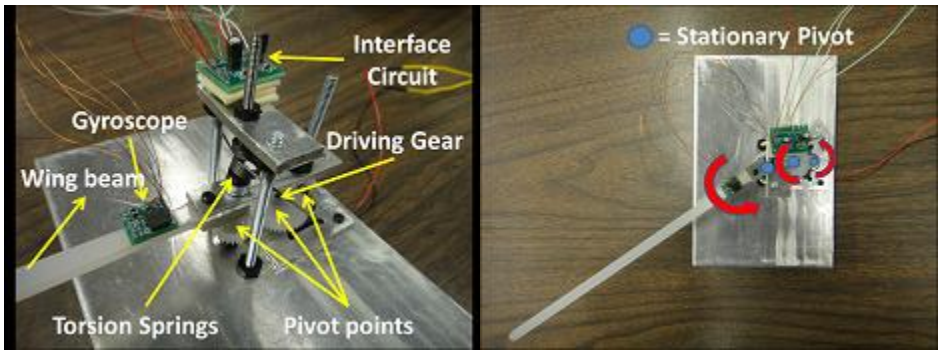

Figure 3.11: Direct Motor Drive - Geared, with feedback

ditionally the linear actuators were not high switching bandwidth capable, were output power/force deficient and required frequent re-tuning / maintenance.

3.3.2 Direct Geared Motor Drive - Reciprocating Motion

The experimentation gave way to the use of a standard geared micro rotary motor, coupled to the wing directly as shown in Fig. 3.11. The figure also shows the gyroscopic feedback obtained from the wing to determine its internal states for executing the closed-loop energy control. The energy control is described in Section 4.6.2.3. The direct drive system was switched by alternating current at a frequency determined by the spring / mass combination. The frequency of flapping was seen to saturate at 11Hz, owing to the bandwidth limitations of the rotary motor in the back-forth motion switching mode. The rotary motor exhibited hysteresis and coil demagnetization issues when polarity across its terminals was switched beyond 11 Hz.

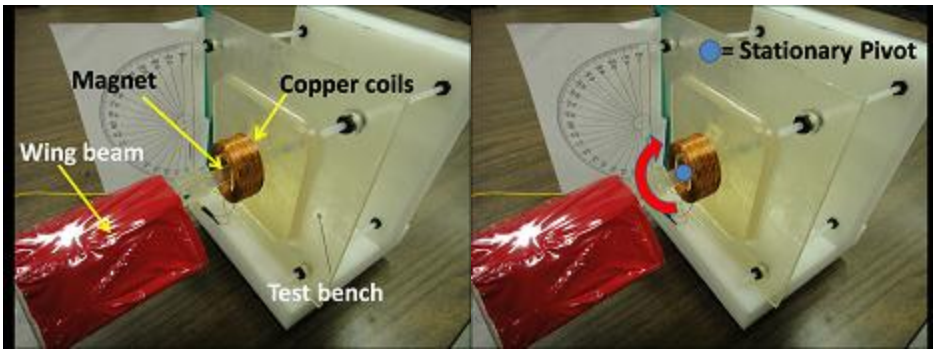

Figure 3.12: Solenoidal Actuator (Called SOLO) - Direct Drive w/ Ext. Spring

3.3.3 Solenoidal Actuator - Direct Drive

The direct drive system from Fig. 3.11 gave ample information and motivation to design a completely new actuation system, without the need to convert rotary motion to reciprocating motion. The design was inspired from some hobby RC servos, but was re-engineered to produce higher output torque. Various magnetic coils were designed (a total of 9 different configurations) and were tested in the manner shown in Fig. 3.12. The Magnet chosen was an N52 Industrial Grade Neobydium Magnet with dimensions of 0.125" Diameter and 1.0" Length Cylindrical. The magnet was repelled/attracted by switching the polarity of the solenoidal coils. The output torque produced by this particular coil (as shown in Fig. 3.12) was 550 gcm at an input power consumption of 1.5 W. The flapping frequency was tested to reach 55 Hz. Some of the other coil configurations tested are illustrated in Table 3.1 and Table 3.2. Some of the efficient coil configurations were able to produce over 40^o wing sweeps at resonance at small power consumptions. The results came out to be very promising and the system was miniaturized to the form shown in Fig. 3.14 to be used on an actual prototype.

3.3.3.1 Solenoidal - One-Spring Configurations

One design approach was to use spiral springs, since they are impartial to rotation in either direction and yet adhere to *Hooke's Law* (Fig. 3.13). A potential disadvantage of the proximal spring was non-linear operation. A wire form spring can also be used, as a cantilever

Table 3.1: Coil Configurations and Power Results (All coils operated at 3.6V)

S.no	D $_{Inner-Major}$ (mm)	D $_{Inner-Minor}$ (mm)	Height (mm)	AWG	Total Turns	Layers	Turns/Layer	Winding Thickness (mm)
1	30.3	19.1	17.5	28	4,737	100	48	36.7
2	30.3	19.1	17.5	31	1,815	27	67	7.0
3	30.3	19.1	17.5	32	284	4	75	0.88
4	30.3	19.1	17.5	25	1,290	38	34	20.1
5	30.3	19.1	17.5	26	625	17	37	7.7
6	30.3	19.1	17.5	28	103	2	48	0.8
7	30.3	19.1	17.5	18	402	27	15	31.8
8	30.3	19.1	17.5	19	321	19	17	20.2
9	30.3	19.1	17.5	21	168	8	21	6.6

Table 3.2: Coil Configurations and Power Results Continued from 3.1.

S.no	Length of Wire (m)	Current (mA)	Resistance (Ohm)	Time Constant (ms)	Torque (gcm)	Weight (g)	Insulation	Wing Sweep (Degrees)
1	908	34	206	25	3.9172	653	Enamel	8^o
2	173.6	55	82.2	2.5	60.6	62.3	Enamel	20^o
3	22.0	260	13.2	0.25	145.42	6.4	Enamel	27^o
4	179	150	19	10	443	259	Enamel	40^o
5	68.5	310	8.45	2.5	649	78.6	Enamel	46^o
6	7.1	800	2	0.25	443	5.1	Enamel	40^o
7	74.1	1A	1.5	20	811	521	Enamel	50^o
8	45	1.1A	1.2	10	1040	262	Enamel	55^o
9	14.8	1.45A	0.7	2.5	811	54.5	Enamel	50^o

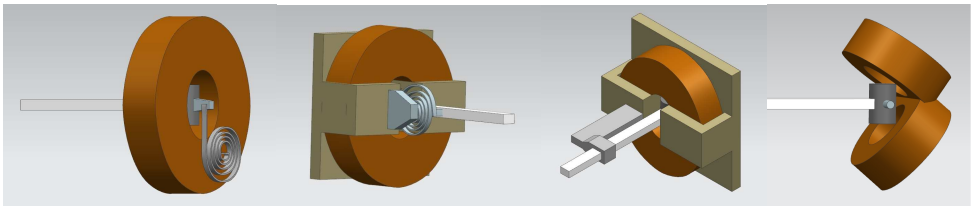

Figure 3.13: a) Proximal, b) Distal spiral spring; c) Cantilever Spring; d) Double Coil

Figure 3.14: Micro Solenoidal (SOLO) Actuators: (Left: Extension-Spring; Right: Compression-Spring)

beam, as shown in Fig. 3.13a and Fig. 3.13b. The use of two coils to allow for a more concentrated magnetic field density around the magnet was also investigated; however the design was found to be impractical due to size constraints[4].

The in-line spring arrangement in Fig. 3.12 was rearranged to make the system more compact. The benefit of this arrangement (Fig. 3.14) is that it allows for a reduced wingspan. The actuator was also miniaturized to weigh 5 g and produced an output torque of 75gcm. At 3.6 V, the coil drew 500 mA and reached a resonant frequency of 20 Hz.

3.3.4 Rotary to Reciprocating Drive Systems

Another path towards obtaining resonance flapping was through rotary motor driven reciprocating systems. However unlike the solenoidal and linear actuators, the rotary motor based FiFVA systems needed to have an additional degree of actuation to control Amplitude Modulation.

3.3.4.1 Vertical-Axis Cam Follower

The first cam design was a hollowed cylinder that had been cut at an angle across its axial cross-section (Fig. 3.15).

The tip of the piston contacts the lip of the cam and is forced upwards/downwards with the cam rotation. When rotated constantly about its vertical axis, this cam causes perfect

[4]The CAD for Fig. 3.13, 3.14 was done by Aaron T. May and Josh Sandler

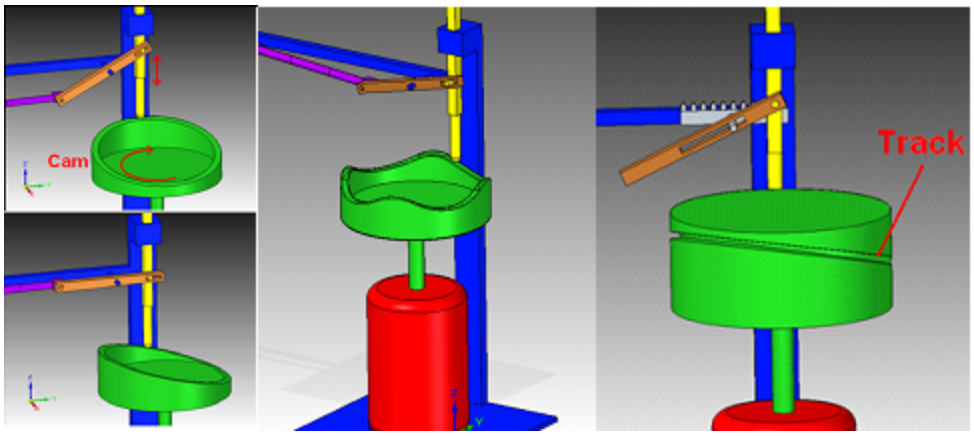

Figure 3.15: Motion of vertical cam and displacement of piston

sinusoidal motion in the piston. By placing more sinusoidal ridges along the circumference, more oscillations can be achieved (Fig. 3.16, Right). This is also seen on the Vertical-Axis cam (Fig. 3.15, Center). A track with a ball bearing can also be used instead of a cam shape as shown in Fig. 3.15(Right)[5].

3.3.4.2 Horizontal-Axis Cam

Designs involving cams with a horizontal axis of rotation were also examined. Seen in Fig. 3.16. The elliptical cam would allow a piston-follower to reciprocate twice per cam rotation. The higher the "major-to-minor axis" ratio (a thinner ellipse), the greater the deviation from sinusoidal motion. The instantaneous piston position from the cam pivot is given by $R = \sqrt{(a.cos\theta)^2 + (b.sin\theta)^2}$, where θ is the angular position of the point of contact of the piston with the cam and represent the ellipse semi axis. Larger ratios (elongated ellipses) experience steep transitions in displacement. A ratio of 1.333 gives near-sinusoidal motion. Although cams provide possible mechanical advantages, they also create issues in friction and scaling when working on the scales intended for micro air vehicles.

[5]The CAD design for the vertical and horizontal-axis cams were done by Emanuel M. Jones

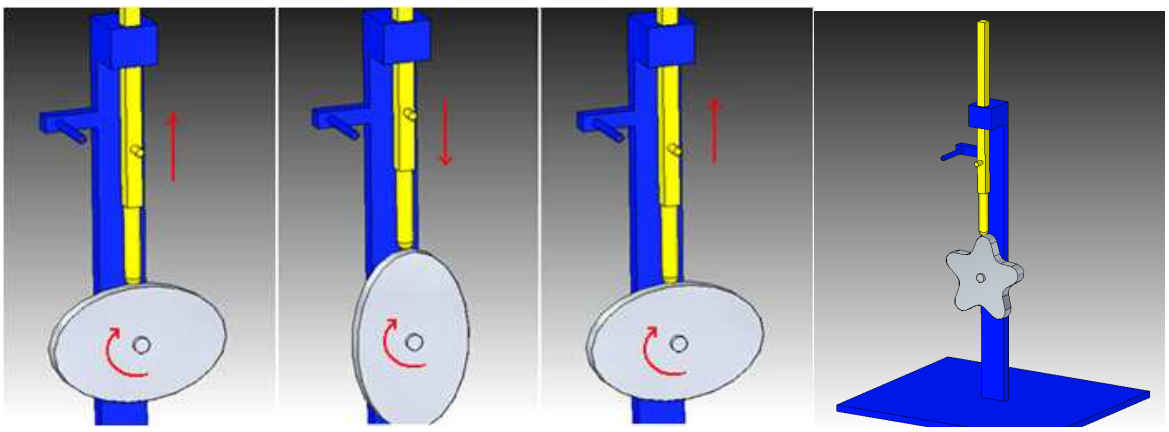

Figure 3.16: Horizontal -axis cam rotation and piston motion

3.3.4.3 Hypocycloidal Gear Train

A hypocycloidal gear train[6] was examined since by the use of an additional worm gear arrangement, amplitude modulation is possible, providing FiFVA control over wing flapping.

A spur gear is pivotally attached to a plate and spun around the inside of the ring gear. The internal ring gear and the spur gear have a 2:1 ratio so that the red dot seen in Fig. 3.17 will travel in a straight line throughout the spur gear rotation. The worm gear at the bottom of each diagram in Fig. 3.17 has the ability to shift the entire ring gear through 0 to 90º rotation (note the black dot), thus rotating the motion of the red dot to a horizontal position, rendering none or minimal vertical displacement depending on whether a yoke is used or not respectively. Any amplitude between maximum and zero displacement is attainable simply by rotation of the internal ring gear. Maximum amplitude obtained equals the pitch diameter of the ring gear.

A connecting rod was chosen for this system, to extend from the spur gear (red dot) and to attach to the wing to create flapping motion, similar to that seen in conventional ornithopters (Fig. 3.18).

Note 3.1. *Note 1:* Working of the different actuation schemes has also been presented in

[6]The work on the hypocyloidal actuation was done with the help of Emanuel Jones

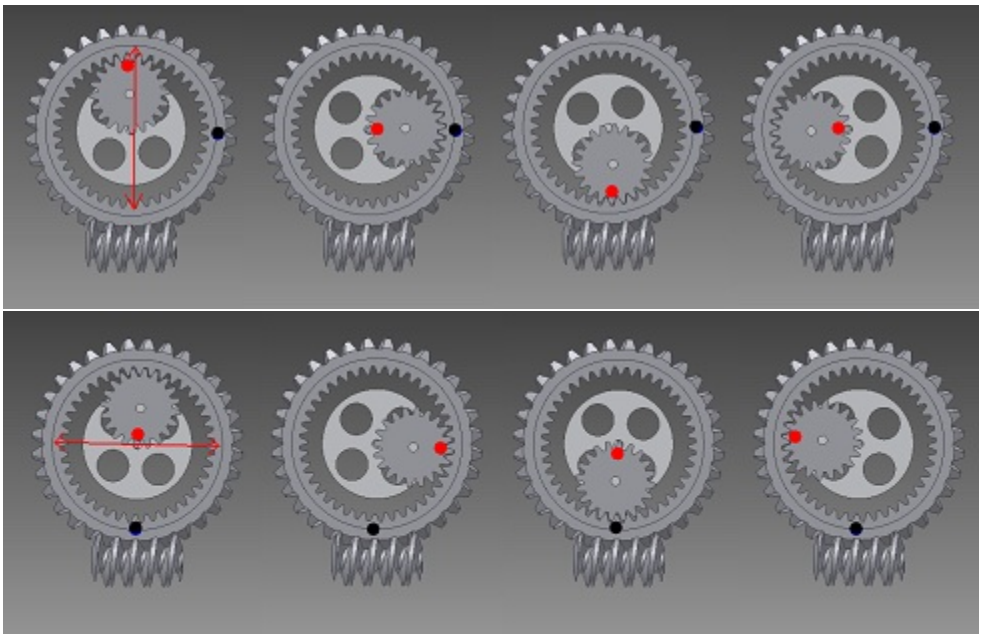

Figure 3.17: Hypocycloidal Gear Train (Amplitude Modulation)

the video accompanying the dissertation.

3.3.4.4 Actuation Efficiency Increase: Spring Jointed Wing

The original prototype is shown in Fig. 3.18. It was essential to use the same mechanism prototype to test the efficiency increase when moving from a Non-Spring Jointed Wing to a Spring Jointed Wing. This was essential to remove any ambiguity or doubts associated with changing the platform. The MorphES actuation mechanism is able to produce identical flapping as in regular crankshaft mechanism, when the amplitude is kept constant. The system in that case works on Frequency Modulation for generating higher lifts. When appended with an extension spring as shown in Fig. 3.19, the system develops a natural frequency determined by the inertia, damping and spring constants. By fixing the flapping frequency at constant and modulating the amplitude, the system was shown to produce resonant flapping.

Note 3.2. The spring configuration is not the one proposed initially. A lot of frictional losses (internal coil friction, friction with sliding yoke) were observed. Also the spring

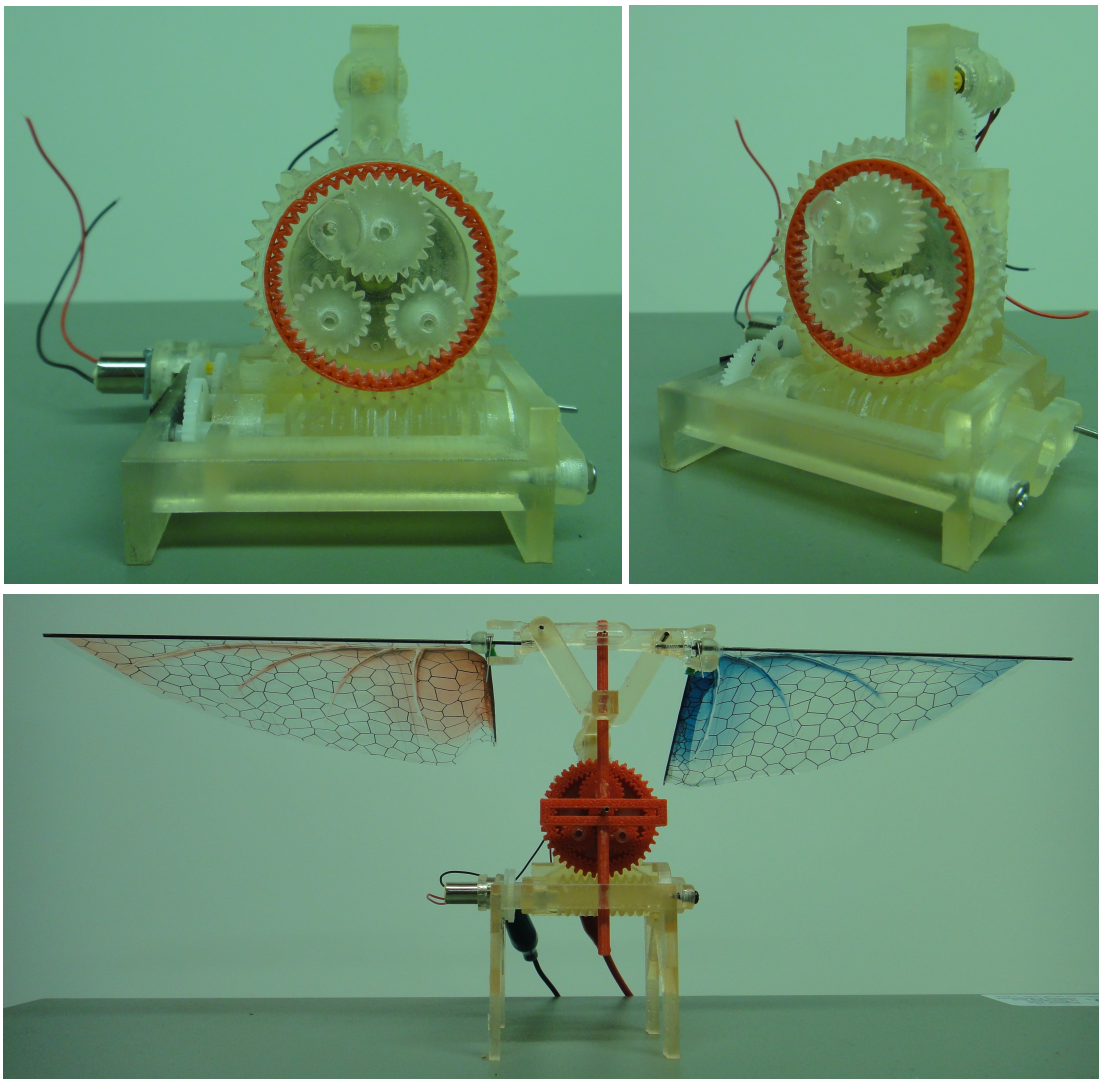

Figure 3.18: Hypocycloidal Gear Mechanism, called MorphES: Inter-meshing of the internal gears (Top); Assembled Prototype (Bottom)

doesn't compress linearly (as modeled previously), it however shows non-linear bending and torsion due to its much bigger inner diameter as compared to the yoke-shaft (causing non-linear compression). However, the compression was seen to be linear for small amplitudes (small compressions); this can be seen in the Fig. 3.21 and Fig. 3.22.

Remark 3.2. The results seen in Fig. 3.22 do not match those seen in Fig. 3.21 due to the non-linearity of the spring compression (for higher amplitude flapping) and also due to the severly increased friction due to the grinding of coils in large compression and also due to their friction with the sliding yoke-shaft. The spring configuration is being moved to a more efficient configuration as shown in Fig. 3.14b.

Note 3.3. Fixed Amplitude systems like those used in the state of the art cannot start-up with a spring installed. The spring imparts a very significant torque while starting the motors and does not allow regular crankshaft systems to start up. This limitation is very conveniently overcome by the MorphES[7] actuation system by the use of continuously varying gearing mechanism integrated into its operation. By beginning at neutral position (zero amplitude) and gradually gearing-up (increasing amplitude) the system progressively adds potential energy to the spring, while staying in sync with its natural resonant frequency. This is one very novel feature of the MorphES actuation system, making resonant flapping feasible with the use of rotary actuators.

Fact 3.1. *No flapping actuation system till date has been able to achieve resonant flapping by the use of springs. The MorphES actuation system is the first system achieved to make resonance flapping feasible by its continuous/dynamic gearing (up/down) capability.*

Table 3.3, lists the power consumption results obtained at different amplitude magnitudes for the flapping mechanism.

It is shown in the experimental run that by adding the spring into the flapping mechanism, power consumption by the system reduced significantly compared to a non-spring system.

[7]MorphES Stands for: Morphing Energy Saving

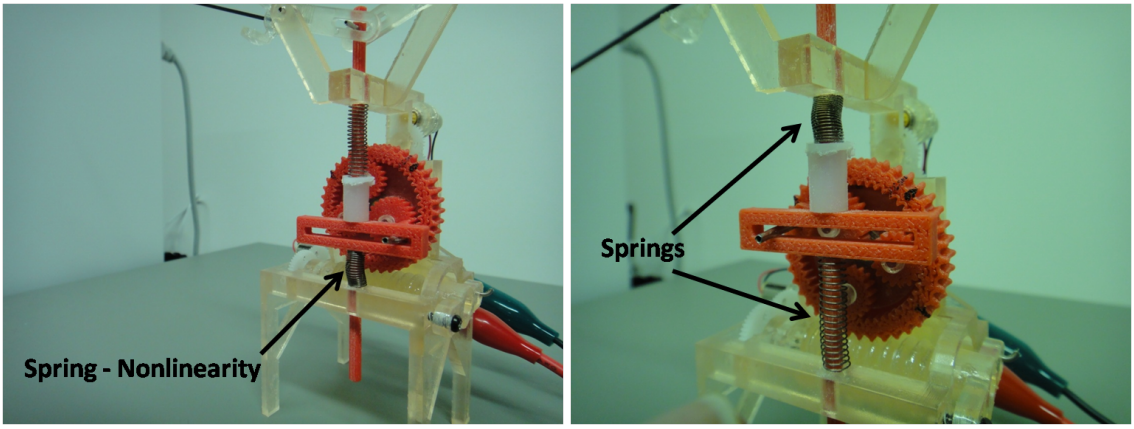

Figure 3.19: MorphES Actuation System, Spring Loaded Wings: Magnified (Side View)

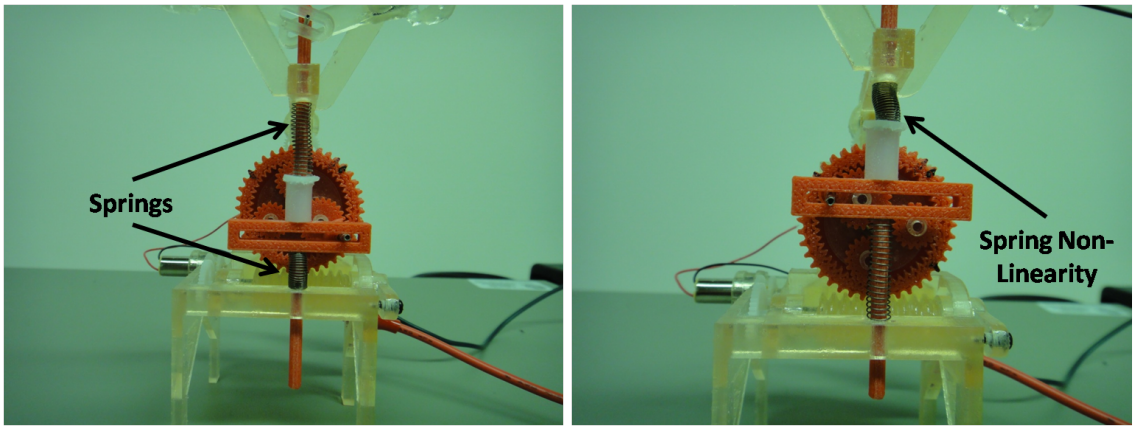

Figure 3.20: MorphES Actuation System, Spring Loaded Wings: Magnified (Front View)

Table 3.3: Experiments: Resonant Flapping Configuration and Power Performance

Spring Constant (K) (Lbs/in)	**Flapping Amplitude (% of Maximum)**	**Resonance Frequency (Hz)**	**Power (mW) @ Resonance (With Spring)**	**Power (mW) (No Spring)**	**Increase in Power Intake (%) (With No Spring)**
0.29	10	9.469	72.26	90.46	25.19
0.29	20	9.27	83.97	91.28	8.71
0.29	30	9.08	164.2	88.25	N/A (Friction Upset Results Significantly)
0.29	40	8.9	158.5	83.03	N/A (Friction Upset Results Significantly)

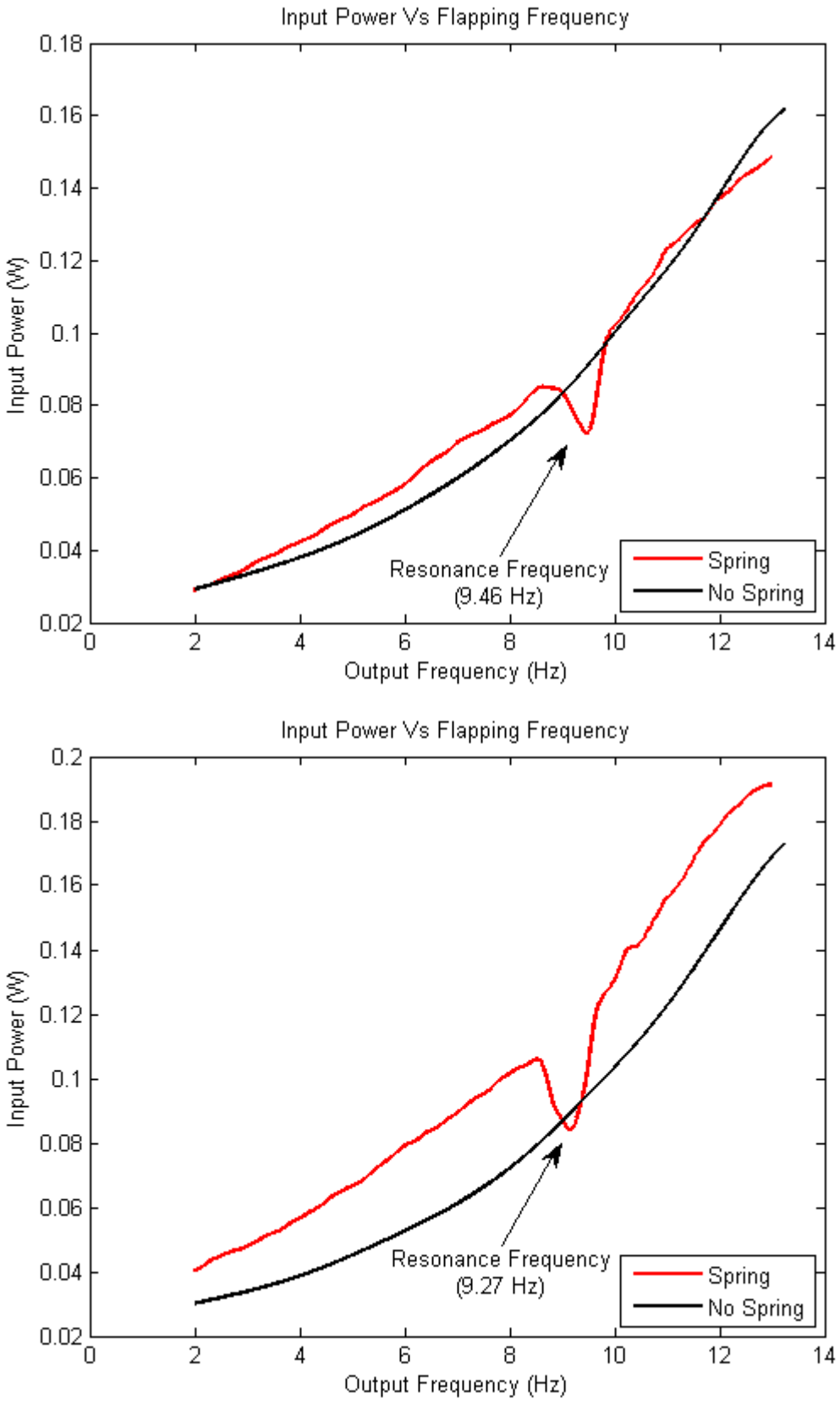

Figure 3.21: Flapping Power Intake vs Flapping Frequency: 10% Amplitude (Top), 20% Amplitude (Bottom)

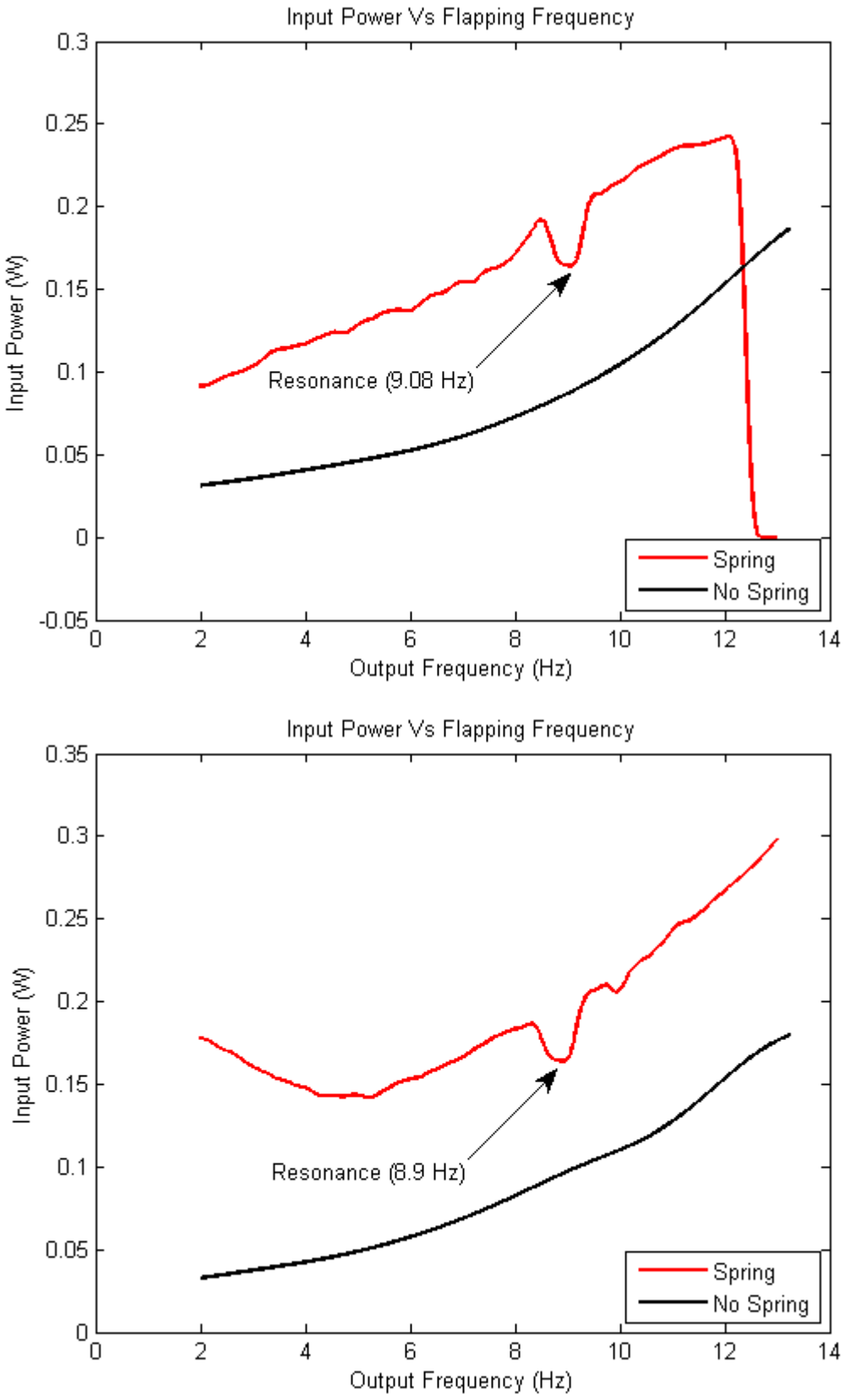

Figure 3.22: Flapping Power Intake vs Flapping Frequency: 30% Amplitude (Top), 40% Amplitude (Bottom)

Exercise 3.1. In the first experiment the flapping amplitude was set at 10% of the maximum possible amplitude by actuating the amplitude control motor. The resultant input power was seen to be approximately 91mW with "no-spring"; the power consumption with the spring was approximately 72mW. The increase in power consumption by removing the spring was seen to be approximately 25%. This result follows the theoretical analysis done in Chapter 2.

Exercise 3.2. In the first experiment the flapping amplitude was set at 20% of the maximum possible amplitude. The resultant input power was seen to be approximately 90mW with "no-spring"; the power consumption with the spring was approximately 84mW. The increase in power consumption by removing the spring was seen to be approximately 8.71%. This result follows the theoretical analysis done in Chapter 2.

Exercise 3.3. For the third and fourth experiment, the flapping amplitude was set at 30% and 40% respectively. The result was a significant drop in flapping efficiency. The power consumption increased by approximately 90% over a "no-spring" condition. This is explained by the non-linear operation of the spring at higher flapping amplitudes. The spring configuration was not correctly set-up leading to significant grinding and friction between adjacent coils of the spring. The coils also locked against each other and did not compress linearly as observed at lower flapping amplitudes.

Remark 3.3. It was observed that at higher flapping amplitudes, the resonance frequency decreased nominally. This is explained by the addition of friction / damping at higher frequencies. The natural harmonic oscillation frequency decreases with increased damping.

It was seen that when flapping the wing mechanism at near about the resonance frequency, there was an enormous drop in power consumption from normal operational values. Driving the spring-jointed wing at Off-resonance frequency was seen to consume a significantly large amount of power (This is intuitive).

The results obtained match very closely to those obtained in Chapter 2. For Experiments 1 and 2, the friction can be considered as the damping element. As damping increased from Experiment 1 to Experiment 2, the efficiency improvement decreased, as shown in Fig. 3.6.

It was successfully shown that the wing-spring system exhibited natural resonant oscillation frequencies. By exciting the wing at the resonance frequency set by the spring-mass combination, the power consumption was noted. It was demonstrated that by matching the resonance frequency of the spring-mass combination, the actuation power consumption reduced significantly. 44% input power was seen to be conserved with the use of the spring. The effectiveness and viability of spring-jointed mechanisms has been demonstrated to match those without the spring and were seen to outperform the non-spring jointed wings in power consumption requirements.

3.3.5 MAV Designs based on Different Actuation Schemes

3.3.5.1 Modular MAV Configurations

At present there are four different MAV prototypes being constructed in our laboratory conforming to the QV design specifications; each has four wings to produce Lift & 6DoF control. The main chassis of the prototypes is common across the four prototypes. Some of the 3D prototypes are shown in Fig. 3.23[8].

3.4 CHAPTER CONCLUDING REMARKS

The chapter undertook the discussion on the design and evolution of the different FiFVA actuation systems produced to facilitate resonance flapping of wings of an MAV. A comparative study of the different actuation mechanisms developed over time was undertaken. Two actuation systems namely the SOLO and MorphES were shown to provide exceptional performance towards resonance flapping. The SOLO actuation was seen to provide resonance flapping by the use of only one actuator. The MorphES actuation performed the same

[8]The CAD was created by Emanuel M. Jones

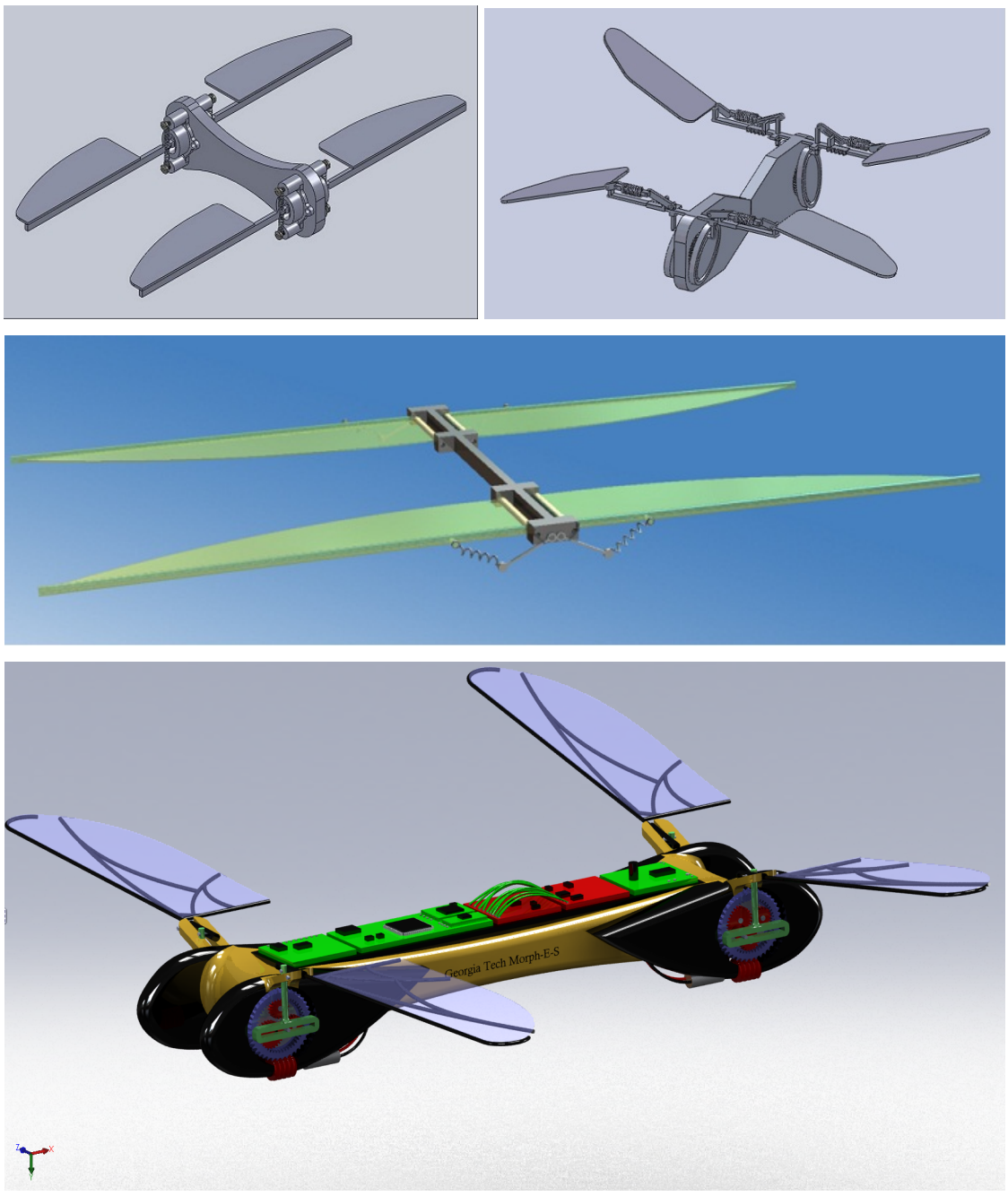

Figure 3.23: MAV Designs based on SOLO Actuators, Micro Linear Actuators, Cam-Follower Drive Trains and the MorphES Actuators

Table 3.4: Comparison of Different Fixed Frequency - Variable Amplitude (FiFVA) Actuation Schemes: Prototype Revisions I

Actuator Type	**Actuation Method to produce Wing Flapping**	**Mechanism / Coupling**	**Mechanical Complexity**	**Scalability (towards smaller size)**	**Power Intake** (P_i)
Linear - Ultrasonic Piezoelectric	Switching electrical polarity across actuator for Frequency Modulation;	Hard Coupling: Four-Bar (w/ Torsional Spring) coupling to wing	Medium - High (15 Hz Flapping)	Medium Scalability - Efficiency drops with smaller scales	5 W (10V Differential, 500mA)
		Hard Coupling: Four-Bar (w/ Extension Spring) coupling to wing	Medium (15 Hz Flapping)	Medium Scalability - Efficiency drops with smaller scales	4.5 W (10V Differential, 450mA)
	Input Voltage Modulation of actuator for Amplitude Modulation	Soft Coupling: Four-Bar (w/ Extension Spring) coupling to wing	Medium (15 Hz Flapping)	Medium-High Scalability - Efficiency drops with smaller scales	3.75 W (10V Differential, 375mA)
Direct Geared DC Motor	Switching electrical polarity across motor for Frequency Modulation;	Hard Coupling: (w/ Torsional Spring), Geared down coupling to wing	Medium (11 Hz Flapping)	Medium-High Scalability	7.2W (8V, 900mA)
	Input Voltage Modulation of motor for Amplitude Modulation	Soft Coupling: (w/ Extension Spring), Geared down coupling to wing	Low-Medium (11 Hz Flapping)	High Scalability	8W (8V, 1A)

Table 3.5: Comparison of Different Fixed Frequency - Variable Amplitude (FiFVA) Actuation Schemes: Prototype Revisions II

Actuator Type	**Actuation Method to produce Wing Flapping**	**Mechanism / Coupling**	**Mechanical Complexity**	**Scalability (towards smaller size)**	**Power Intake** (P_i)
Solenoidal, Magnetic Angular Actuator	Switching electrical polarity across coil for Frequency Modulation;	Soft Coupling: (w/ Extension Spring)	Low-Medium (55 Hz Flapping)	Very High Scalability	1.08W (3.6V, 300mA)
	Input Voltage Modulation of coil for Amplitude Modulation	Soft Coupling: (w/ Compression Spring)	Low-Medium (55 Hz Flapping)	Very High Scalability	Not Tested at same size/scale
DC Motor Primary (Brushless/Coreless) - Main Drive	Input Voltage Modulation of primary motor for frequency Modulation;	Horizontal cam: (w/ extension spring) and worm geared movable pivot	Very-High (Conceptual System)	Low Scalability (Mechanical couplings harder)	(Conceptual System)
&		Vertical cam: (w/ extension spring) and worm geared movable pivot	High (Conceptual System)	Low Scalability (Mechanical couplings harder)	(Conceptual System)
DC Motor Secondary (Coreless) - Amplitude Servoing	Input Voltage Modulation of secondary motor for Amplitude Modulation	Hypocycloidal System: Planetary Gears on Cyclic, driven by Primary Motor; Ring Gear - driven by worm-geared secondary motor; Extension/Compression Springs at wing pivot	Highest (25 Hz Flapping, with variable amplitude)	High Scalability (Although Mechanical couplings hard)	0.75W (3V, 250mA)

operation using two actuators (one for frequency modulation, other for amplitude modulation), however provided more output torque to the wings than the SOLO. The SOLO on the other hand was very easily miniaturized.

A torque comparison model between a non-spring jointed wing and a spring-jointed wing was laid out and shown to predict improvement in output torque requirement by employing a passive spring in the actuation mechanism. Non-use of springs showed torque increase by many folds over spring jointed flapping mechanisms, spanning to 100% and above in many cases. The theoretical predictions were followed with hardware experimentation and power efficiency was shown to improve with spring-jointed wings; an improvement of 25% was observed in one of the cases.

CHAPTER IV

FLIGHT CONTROLLER DEVELOPMENT

4.1 CHAPTER OBJECTIVES

The objectives of this chapter are to address the following:

1. Kinematic analysis of the wing mechanism
2. Dynamics analysis of the wing mechanism and creating a wing model to be tested in simulation
3. Controller development at wing level: Non-linear Hybrid Energy Control of the wing
4. Controller development at MAV level: Modeling/dynamics of the combined four wing configuration and the design and application of a novel 6DoF flight control scheme
5. To demonstrate the practical effectiveness of the control system on a hardware prototype of the four-wing MAV design

Note 4.1. The appendices, address the Embedded System Design and Development to equip the prototype with on-board processing and sensing capabilities, essential for a Hardware in Loop Simulation (HILS). The appendices also illustrate some of the aerodynamic analysis, carried out towards designing the flapping and feathering mechanism of the MAV Wing.

4.2 MAV DESIGN CONCEPTION: QV DESIGN

Given the requirement for a more efficient MAV design and having shortlisted one of the natural flyers as inspiration for the four-wing design, Fig. 1.4, the new MAV design concept (QV Design[1]) adapts some of the characteristics of the dragonfly with indigenous modifications. The basic conceptual design is of the form as shown in Fig. 4.1.

[1]QV stands for Quad-Wing MAV. The name has been chosen to abbreviate the most basic appearance of the illustrated four wing design

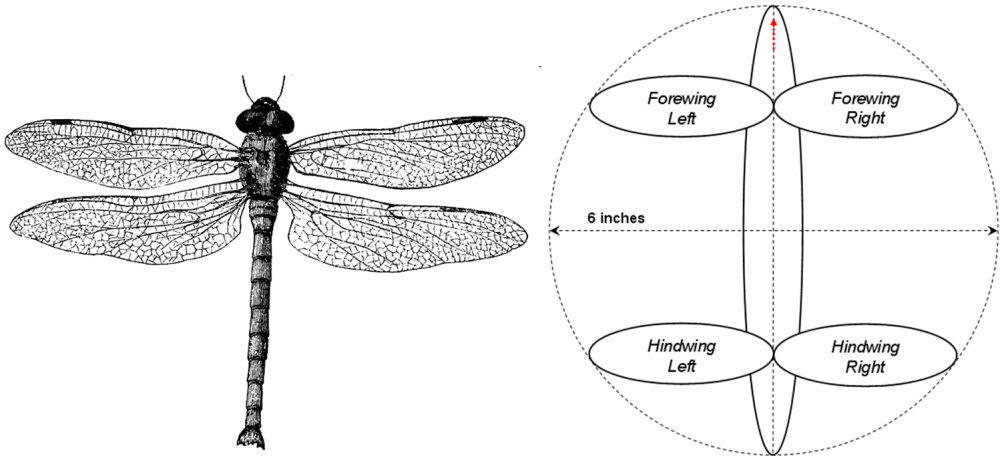

Figure 4.1: Conceptual Design of a Dragonfly-Like MAV

4.2.1 Design Similarities and Differences from a Dragonfly

1. The four wings have been retained in the new design to enable higher propulsion forces, thereby improving the payload capability of the system. Conventional MAV designs only utilize 1 pair of wings (Ref. Chapter 1)
2. The wings have been spaced further apart along the length of the MAV to improve pitch and yaw controllability of the system (Increased inertia; slowing down system dynamics)
3. Similar to a dragonfly, the wings are controlled independently of one another, hence are mechanically decoupled from each other.
4. Unlike a dragonfly, each wing has only 1 DoF of motion, thereby reducing the actuators required on each wing to just one.
5. The second degree of freedom on each wing is passive, i.e. the wing feathers about its longitudinal axis; whereby the wing produces a positive thrust on the body (Up thrust) on its downstroke but acts like a streamlined planar laminar on its upstroke, thereby minimizing the negative lift on the body.
6. Each wing is capable of elastic storage and re-use of propulsion energy, which helps in reducing the power intake of the wing in each cycle.

7. The wings resonate based on the frequency defined by the spring-mass combination of the wing's elastic restoring joint and the mass of the wing. The frequency of each wing is thereby kept constant and only amplitude is varied by controlling the power to the wing actuators, similar to insect flight.

4.2.2 Assumptions During Design Conception

To facilitate the design of the Quad-Wing MAV (QV) and develop control and actuation strategies, the following assumptions have been made:

1. The complex aerodynamics present at low Reynolds number flight have been neglected for designing the control system, although a detailed discussion has been carried out in Appendix A.2.
2. Only the aerodynamic lifting forces generated due to flapping motion have been integrated in the non-linear system and controller design discussed herein, other aerodynamic complexities have been treated as out of scope for the discussion.
3. The wings of the system are simple shapes: rectangles, circles, ellipses or quarter-ellipses (Appendix A.2).
4. The present analysis also considers the lift forces to be only bi-directional, i.e. downward force and outward force as shown in Figure 4.15. The thrust component (directed from the wing's leading edge spar to its trailing edge) has been ignored in the controller development.

Further assumptions have been made during the course of conception, design and analysis and have been listed where ever necessary.

4.3 WING ACTUATION MODELING

The idea of using a system which maintains constant frequency but varying amplitude better approximates the flight dynamics of insects and birds. Such a system has been attempted

but never conceived in reality [22, 28, 29, 36]. A basic mathematical model of the actuation mechanism has been developed and briefly described herein. The nomenclature of the symbols used in the following equations is illustrated in Figure 4.4.

The system model is based on two coupled mechanisms in series, a four-bar linkage mechanism and an inverse crank-shaft mechanism. Fig. 4.4 illustrates the coupled mechanism. The kinematics and dynamics of the four-bar linkage and crank-shaft mechanisms are interrelated in the state vector X from Equation 4.24. The design was adapted from the basic concept of actuating the wing using reciprocating linear actuators (solenoids, to begin with). The basic idea is demonstrated in Figure 4.2.

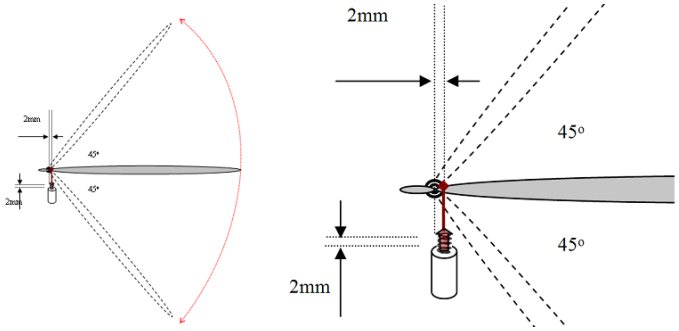

Figure 4.2: Actuation Mechanism Using Linear Actuators: Basic Idea

As seen in Figure 4.2, the solenoid reciprocates the wing by switching between pushing and pulling motion. However to obtain an appreciable amplitude, the placement of the solenoid needs to be very close to the wing pivot, as shown in the Figure 4.2. This raises linkage and structural deformation concerns. The four bar linkage was utilized to overcome the linkage difficulties. The solenoids are attached much further from the wing pivots now, as shown in Figures 4.3, 4.4 and 4.5.

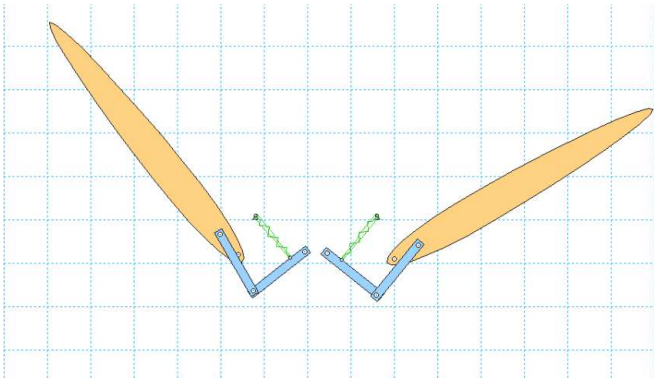

Figure 4.3: Simulation in Working Model 2D

A simulation platform was created in Working Model 2D[2]. The wing with the actuator, spring and four bar linkages has been shown in Figure 4.3.

4.3.1 QV Wing Mechanism Kinematics: Nomenclature

In the referenced figure, the global origin has been defined as the Joint 1, $O_0\,(x_o,y_o)$, The wing is pivoted about Joint 3, $O_3\,(x_3,y_3)$ and extends upto Joint E, $O_E\,(x_E,y_E)$. The solenoid can be seen as the grey cylinder. Its extension range is from $O_5\,(x_5,y_5)$ to $O_5'\,\left(x_5',y_5'\right)$ or equal to x. The pivot O_0 acts as the crank pivot. The inverse crank-shaft mechanism is required to transfer the force from the solenoid to the four bar mechanism and vice versa. L_1, L_2, L_3 and d_{03} act as the four limbs of the four bar linkage mechanism.

[2]Software by Design Simulation Technologies, Inc.

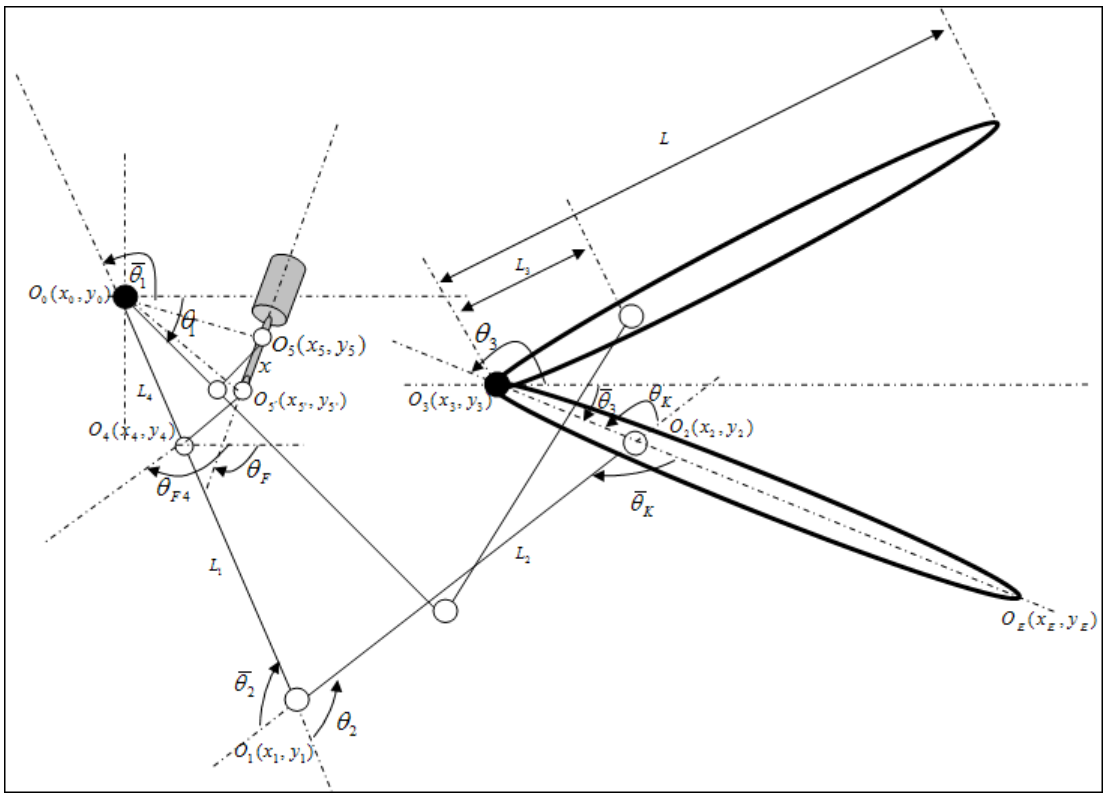

Figure 4.4: Illustration of Nomenclature: Kinematic Relationships

We can define distances and pin joint reference points as: d_{05}, d_{45}, $d_{05'}$, x_5, y_5, $x_{5'}$, $y_{5'}$ etc. Out of which $d_{05'} = d_{05} + x$ is the variable linkage. More on the derivation of these terms is elaborated in the appendix. We also divide the joint 1 angle $\angle\theta_1$ into smaller angles as shown in Equation 4.1 for simplifying the calculation of $\angle\theta_1$. The definition and derivation of these smaller angles is explained in the Appendix A.1.1. In order not to deviate from the context, it is sufficed to mention that $\angle\theta_1$ is kinematically deterministic from the solenoid (linear actuator) piston position.

$$\theta_1 = \theta' + \theta'' + \theta''' \tag{4.1}$$

4.3.2 QV Wing Mechanism Kinematics: Displacement Analysis

Applying the fundamentals of *Inverse Kinematics* we start from θ_3 and work our way back

to θ_1. θ_1 is the quantity that is known at all times because of the knowledge of the system variable x (Linear actuator instantaneous stroke position). We assume new variables to simplify our computation

$$\begin{aligned} L_1 Cos\theta_1 + L_2 Cos(\theta_1 + \theta_2) &= (x_3 - x_0) + L_3 Cos\bar{\theta}_3 \\ L_1 Sin\theta_1 + L_2 Sin(\theta_1 + \theta_2) &= (y_3 - y_0) + L_3 Sin\bar{\theta}_3 \end{aligned} \tag{4.2}$$

The equation 4.2 describes the basic displacement equation. Where the symbols and new variables have been described in Appendix A.1.2.

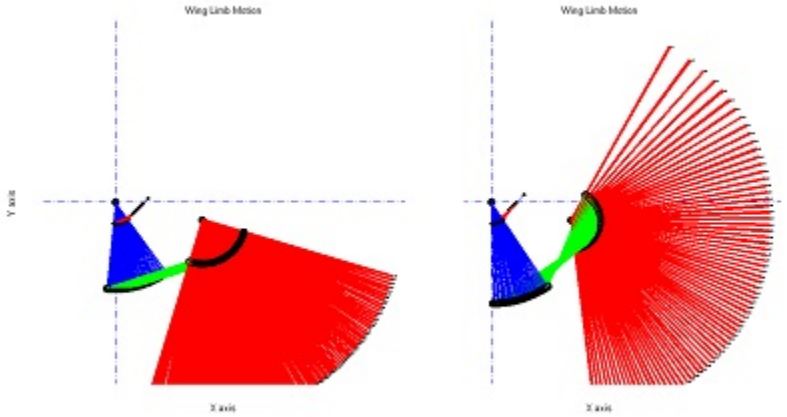

Figure 4.5: Wing Sweep: Range of Motion $\left(L_{3-Left} > L_{3-Right}\right)$, hence wing's range of motion is smaller (Left Fig.). By fixing the dimensions and position of various joints/limbs, the wing can be made to correctly generate a full sweep (Right Fig.)

4.3.3 QV Wing Mechanism Kinematics: Velocity Analysis

The angular velocity analysis and derivation has been elaborated in Appendix A.1.3. The final values of angular velocities are given as follows. These values have also been derived in [33], under the 'kinematics of a four bar linkage'.

$$\omega_1 = \dot{\theta}_1 = \omega_3 \frac{L_3}{L_1} \frac{Sin\theta_k}{Sin\theta_2}$$

$$\omega_2 = \dot{\theta}_2 = -\omega_3 \left(\frac{L_1 L_3 Sin(\theta_3 - \theta_1) + L_3 L_2 Sin\theta_k}{Sin\theta_2 L_1 L_2} \right) \tag{4.3}$$

$$\omega_k = \dot{\theta}_k = \omega_3 \left(1 + \frac{L_3 Sin(\theta_3 - \theta_1)}{Sin\theta_2} \right)$$

4.3.4 QV Wing Mechanism Dynamics

The nonlinear system can be modeled as an externally actuated, damped spring-mass system, where the force/thrust is applied in consequence of the solenoidal push/pull motion. The inverse crank shaft mechanism has the solenoid as the actuating shaft and the limb 1 acting as the crank. Thus converting linear reciprocating solenoidal motion into rotational reciprocating motion required at the wing joint.

However the rotational range of motion obtained is not adequate to provide a full 110^o sweep angle, as seen in a dragonfly; hence the need to amplify this range of motion. To achieve this active amplification, a 4-bar linkage mechanism is utilized. The mechanical construction and connections have been demonstrated in the schematic diagram 4.4.

To generate the model for each wing, the different torques acting on the wing need to be considered:

1. $\tau_{30Solenoid}$, or the solenoidal torque being transferred to the wing through the 4-bar linkage from the Joint 1 to wing Joint 3. Only a component of the total solenoidal force will be visible at Joint 3 owing to losses through the transference.
2. $\tau_{3Limb-JointWeights}$, is the torque imparted to the wing due to gravity acting on the different masses (wings, limbs and joints) of the flapping mechanism. This torque varies dynamically and shifts the equilibrium point of the system.
3. $\tau_{3WingAir-Drag}$, is the damping torque due to air drag acting on the wing, this torque varies with wing speed and also with the direction of motion of the wing.

4. $\tau_{3Spring}$, is the torque due to the restoring action of the spring attached at the wing.
5. $\tau_{3Friction}$, is the damping, frictional torque due air friction and friction at the limb joints.

A fully autonomous system (non-actuated) will have all the above torques except $\tau_{30Solenoid}$. We have derived and simulated the autonomous and driven behavior of the system in the upcoming sections. The net torque acting on the wing τ_3 is as follows:

$$\tau_3 = \tau_{30Solenoid} + \tau_{3Limb-Joint\,Weights} + \tau_{3WingAir-Drag} + \tau_{3Spring} + \tau_{3Friction} \tag{4.4}$$

4.3.4.1 Torque on the Wing due to Air Drag

$$d\tau_{3air} = -\frac{1}{2}\rho_{air}\omega_3^2 l^3 W_L(l)\, dl\, C_D \tag{4.5}$$

$$\tau_{3WingAir-Drag} = -\frac{1}{2}\rho_{air}\omega_3^2 C_D \left[\int_0^L l^3 W_L(l)\, dl\right] \tag{4.6}$$

where,

ρ_{air} is the density of air, ω_3 is the angular velocity of the wing, l is a variable distance from the wing pivot. $W_L(l)$ is the wing width as a function of distance l from the pivot. C_D is the Drag Coefficient of the Wing and its value is determined experimentally. The value of C_D will be maximum in the down stroke of the wing due to maximum resistance to air. The value of C_D will be less in the upstroke. The derivation of $\tau_{3WingAir-Drag}$ has been elaborated in Appendix 4.3.4.3.

Assumption 4.1. The C_D values below have been chosen for simplicity of analysis. A better experimental value has been found [35], but not incorporated in the model in this

discussion. The value of C_D has been chosen to be equal to 2.00 on the down stroke, to correspond to a flat plate perpendicular to the flow of air. The value of C_D has been chosen to be equal to 0.1 in the uipstroke, to correspond to a dragonfly's drag coefficient at zero angle of attack [50, 51], but more than that of a flat plate parallel to the flow of air.

4.3.4.2 Wing Mass Dynamics

$d\vec{F}_{wing-mass} = -\rho_{wing} W(l)\, dl\, t(l) g\, \hat{j}$

$W(l)$is the width distribution of the wing,

$t(l)$is the thickness distribution of the wing,

$g$is the acceleration due to gravity

ρ is the density of the wing material

dl is a differential element of the wing at distance of l from the pivot of the wing.

$$\vec{F}_{wing-mass} = -\rho_{wing} g \left(\int_0^L W(l)\, t(l)\, dl \right) \hat{j} \tag{4.7}$$

$$\vec{\tau}_{wing-mass} = \vec{l} \times \vec{F}_{wing-mass}$$

$$\vec{\tau}_{wing-mass} = -\rho_{wing} g\, Cos\theta_3 \left(\int_0^L W(l)\, t(l)\, l\, dl \right) \hat{k} \tag{4.8}$$

$\vec{\tau}_{Limb\,Joint\,Weights}$ can be further optimized by including the above equation for $\vec{\tau}_{wing-mass}$ instead of assuming the M_3 to be located at the middle of the wing.

4.3.4.3 Air-Drag

$$d\vec{F}_{air} = -\frac{1}{2}\rho_{air}\omega_3^2 l^2 W_L(l)\, dl\, C_D \left(\hat{\omega}_3 \times \hat{l}\right) \tag{4.9}$$

$$\vec{F}_{air} = \begin{bmatrix} F_x \\ F_y \end{bmatrix} = \frac{-\frac{1}{2}\rho_{air}\omega_3^3 C_D \left[\int_0^L l^2 W_L(l)\, dl\right]}{|\omega_3|} \begin{bmatrix} Sin\bar{\theta}_3\, \hat{i} \\ -Cos\bar{\theta}_3\, \hat{j} \end{bmatrix}$$

$$\vec{F}_{air} = -\frac{1}{2}\rho_{air}\omega_3 |\omega_3| C_D \left[\int_0^L l^2 W_L(l)\, dl\right] \begin{bmatrix} Sin\bar{\theta}_3\, \hat{i} \\ -Cos\bar{\theta}_3\, \hat{j} \end{bmatrix} \tag{4.10}$$

$$d\vec{\tau}_{3air} = \vec{l} \times d\vec{F}_{air} \tag{4.11}$$

$$d\vec{\tau}_{3air} = -\frac{1}{2}\rho_{air}\omega_3^2 l^3 W_L(l)\, dl\, C_D \hat{\omega}_3 \tag{4.12}$$

Note 4.2. The torques have not been shown as vectors, since in the 2D analysis all torque vectors point out of the plane and hence can unanimously be designated as $\vec{\tau} = \tau\hat{k}$. Hence for further analysis through out the document all torques have been unvectored.

4.3.4.4 Inertia and Angular Acceleration of the System about the Wing Joint

The inertia of the system about Joint 3 is required to calculate the angular acceleration of the system about Joint 3. The result has been adapted from generalized inertia equation derivation, Ref. [33]

$$J_3 = \frac{1}{3}M_1 L_1^2 \left(\frac{L_3}{L_1}\right)^2 \frac{Sin^2\theta_K}{Sin^2\theta_2} + \frac{1}{3}M_3 L^2 + \frac{1}{12}M_2 L_2^2 \left(\frac{L_3}{L_2}\right)^2 \frac{Sin^2(\theta_3 - \theta_1)}{Sin^2\theta_2} + M_2\left(u_2^2 + v_2^2\right)$$

where,

$$u_2 = \frac{L_3}{Sin\theta_2}\left[\frac{1}{2}Sin(\theta_1 + \theta_2)\, Sin(\theta_3 - \theta_1) - Sin\theta_1 Sin\theta_K\right]$$

$$v_2 = \frac{L_3}{Sin\theta_2}\left[Cos\theta_1 Sin\theta_K - \frac{1}{2}Sin\left(\theta_1+\theta_2\right)Sin\left(\theta_3-\theta_1\right)\right]$$

Inertia of the system keeps changing dynamically based on angular positions of the four bar linkage. The instantaneous acceleration of the wing is given by:

$$\ddot{\theta}_3 = \frac{\tau_3}{J_3} \tag{4.13}$$

4.3.4.5 Torque on Wing due to Limbs and Joint Weights

The limb joint torque equations have been derived using Newtonian Force/Torque/Reactions and conservation of moment of the system, using Free Body Diagrams (FBDs) for the four-bar linkage mechanism. All joint masses M_js and limb masses M_is have been included in the calculation. Only the final results have been published here. The derivation has been omitted to maintain continuity.

$$\tau_{0\,Limb-Joint\,Weights} = -\frac{gL_1}{2Sin\theta_k}\left(M_\gamma Sin\theta_k Cos\theta_1 + M_\delta Sin\theta_2 Cos\bar{\theta}_3 + M_2 Cos\left(\theta_1+\theta_2\right)Sin\left(\bar{\theta}_3-\theta_1\right)\right)$$

$$M_\gamma = 2M_{j2} + M_1 + 2M_2$$

$$M_\delta = 2M_{jk} + \frac{L}{L_3}M_3$$

and

$$\tau_{3\,Limb-Joint\,Weights} = -\frac{gL_3}{2Sin\theta_2}\left(Cos\theta_1 Sin\theta_k M_\alpha + Cos\bar{\theta}_3 Sin\theta_2 M_\beta\right)$$

$$M_\alpha = M_1 + 2M_{j2} + M_2$$

$$M_\beta = 2M_{jk} + M_2 + \frac{L}{L_3}M_3$$

4.3.4.6 Torque on wing Due to the Torsional Spring

$$\tau_{3\,Spring} = -K_{spring} \times \left(\theta_3 - \theta_{3\,Equilibrium}\right) \tag{4.14}$$

The spring is a torsion spring with the spring torque proportional to the angular deviation from equilibrium.

4.3.4.7 Torque on Wing due to Friction

$$\tau_{3\,Friction} = -K_{Friction} \times \dot{\theta}_3 \tag{4.15}$$

Assumption 4.2. The value of friction constant $K_{Friction}$ has been kept constantly. Other sources of friction in the system have been ignored, owing to their relatively less dominant values compared to other forces.

4.3.5 Torque on Wing due to the Solenoid Actuator

4.3.5.1 Solenoid Actuator Dynamics:

$$F_{mag} = i^2 \frac{k_a}{(k_b + x)^2} \tag{4.16}$$

F_{mag} is the magnetic force generated by the solenoid, k_a and k_b are approximate constants, determined experimentally[4] and i is the current through the solenoid. The result has been adapted from [4]. A full derivation of the above equation has been given in the appendix.

4.3.5.2 Crank-Slider Mechanism (Force / Torque Conversion):

The conversion of linear solenoidal force F_{mag} to torque about the joint 0 is obtained using the crank-slider mechanism kinematic and dynamic equations. The reference to these derivations is [33]. The final derived equations have been listed here:

$$F_{Generalized} = -\left(F_{mag} \times K_s\right) \tag{4.17}$$

$$\tau_{0\,Solenoid} = F_{Generalized} - E \times \left(\dot{\theta}\right)^2 \tag{4.18}$$

where, $\dot{\theta} = -\dot{\theta}_1$, $K_s = \dfrac{ds}{d\theta}$ and E is the Centripetal Coefficient of the crank-slider system [33].

4.3.5.3 Four-bar Linkage Mechanism (Torque Transfer):

Torque about the linkage 3 due to torque about the linkage 0 has been obtained from [33], under the section on Four-Bar Linkage Dynamics.

$$\tau_{3\,0\,Solenoid} = -\frac{L_3 Sin\left(\theta_k\right)}{L_1 Sin\left(\theta_2\right)} \tau_{0\,Solenoid} \tag{4.19}$$

4.3.5.4 Outer Loop Current Dynamics:

Outer Loop can be achieved by controlling the voltage (V) across the solenoid using Pulse Width Modulation (PWM) based on inertial sensor feedback.

$$V = Ri + \frac{d\lambda}{dt} \tag{4.20}$$

where,

R = Resistance of the Solenoid - battery circuit

i = Current flowing through the solenoid

λ = Magnetic Flux Linkage of the solenoid coil

So,

$$V = Ri + \left(L_{ext} + \frac{d\lambda(x,i)}{di}\right).\frac{di}{dt} + \frac{d\lambda(x,i)}{dx}.\frac{dx}{dt} \tag{4.21}$$

$$\frac{di}{dt} = \left(V - Ri - \frac{d\lambda(x,i)}{dx}.\frac{dx}{dt}\right).\frac{1}{\left(L_{ext} + \frac{d\lambda(x,i)}{di}\right)} \tag{4.22}$$

The $\frac{di}{dt}$ term is required in completing the dynamics matrix of the state space equation 4.24. Further discussion can be followed in Appendix A.1.5.

4.4 NON-LINEAR STATE SPACE MODEL

The wing state vector X bundles the dynamic relationships between the four-bar mechanism, the inverse crank-shaft mechanism, the solenoidal linear motion and current intake at an input U. The State Space model representation is as shown:

$$\dot{X} = f(X,u), Y = g(X,u) \tag{4.23}$$

$$X = \begin{bmatrix} x \\ \dot{x} \\ \theta_1 \\ \theta_2 \\ \theta_k \\ \theta_3 \\ \dot{\theta}_3 \\ i \end{bmatrix} = \begin{bmatrix} x_1 \\ x_2 \\ x_3 \\ x_4 \\ x_5 \\ x_6 \\ x_7 \\ x_8 \end{bmatrix} \text{ and } \dot{X} = \begin{bmatrix} Solenoid\,Linear\,Velocity \\ Solenoid\,Linear\,Acceleration \\ \begin{bmatrix} \\ Joint\,Angular\,Velocities \end{bmatrix} \\ Joint\,3\,Angular\,Acceleration \\ Solenoid\,Current\,Gradient \end{bmatrix} \tag{4.24}$$

The dynamics of the wing motion depend on various configuration specific elements and constants of the wing-coupling which have been captured using $\dot{X}$ in Equation 4.24.

The outputs for the system are the lifting forces produced by the wings of the MAV. The

output model is shown below with its dependence on wing configuration parameters like shape & size and also on air drag & density coefficients.

Assumption 4.3. The wing only produces two components of lift/thrust, one in the downward direction (+/- Y direction) and one in the outward direction (+/- X direction), as shown in Figure 4.15.

$$Y = \begin{bmatrix} F_x \\ F_y \end{bmatrix} = -\frac{1}{2}\rho_{air}\omega_3 |\omega_3| C_D \left[\int_0^L l^2 W_L(l)\, dl\right] \begin{bmatrix} Sin\bar{\theta}_3 \\ -Cos\bar{\theta}_3 \end{bmatrix} \tag{4.25}$$

$$Y = K_{constant} x_7 |x_7| \begin{bmatrix} -Sin\, x_6 \\ Cos\, x_6 \end{bmatrix} \tag{4.26}$$

where, C_D is the drag coefficient of the wing, the derivation has been explained in Section 4.3.4.1. Y defines the lift forces generated by the wing. The mid-level system has been described in Section 4.6.2, which also describes the mid-level linear controller used for the system. The non-linear wing system acts as the substrate for the mid-level linear system.

Once the output Y is determined as a function of state variable X, then we can calculate the total force $Force_{Total}$ = Y, in the x and y directions generated per complete-stroke of the wing, shown in figure 4.15. Thereafter, we can compute the total force Y, generated over a unit time as a function of the state variables and the input V; using the result to compute the Roll, Pitch, Yaw motions of the vehicle, demonstrated in Section 4.6.2.

4.4.0.5 Hybrid Non-Linear System

The dynamics of the system will need to be grouped into two travel regions due to the separate air drags in the upstroke and downstroke of the wing, as shown below.

Region 1: $(x = x_{min}, \dot{x} = 0)$ to $(x = x_1, \dot{x} = max)$ to $(x = x_{max}, \dot{x} = 0)$

Region 2: $(x = x_{max}, \dot{x} = 0)$ to $(x = x_2, \dot{x} = min)$ to $(x = x_{min}, \dot{x} = 0)$

4.5 NONLINEAR MODEL VERIFICATION / SIMULATION

The non-linear model has been verified using free-body, dynamics-modeling and simulation in MATLAB. The verification process has been performed as follows:

4.5.1 Free-Body Simulation of the Wing-Actuator Mechanism - Under Gravitational Restoration

4.5.1.1 Procedure and Assumptions

- First, all external forces (except gravity) have been ignored; damping due to air-drag and friction are all ignored. The actuator is assumed to be free of spring restoring forces or external actuating forces.
- The model in its most simple form can be seen as a complex pendulum; which would have a moment of inertia and restoring force due to gravity only. The moment of inertia is time varying and will have to be modeled appropriately using conservation of energy principles; the moment of inertia can be calculated about each of the joints.
- The kinematics and dynamics of the system have already been defined. The system is initialized at a starting position and released. The resulting motion will be of a complex pendulum and should have a fixed time period (period of oscillation). The actuator will also actuate (guided oscillation: between guide rails) in relation to the kinematics of the system.
- The model was verified by confirming that all the joints and actuators oscillate about the equilibrium position of the system i.e. the system is a lossless system oscillating about its equilibrium point.

4.5.1.2 Results

- As shown in Fig. 4.6a, the actuator oscillates about its equilibrium position in a sinusoidal manner. This is the result of initializing the system at an equilibrium point and letting gravity act on the system. Due to the weights of the limbs/joints of the system, gravity moves the system like a complex pendulum. The actuator coupled to the system, performs kinematical oscillations as well.
- The joints of the system can be seen to perform oscillations about the system equilibrium point as shown in Fig. 4.6b. The system is kinematically constrained; hence the oscillation frequency and sinusoids for all angular positions are mutually dependent. The system also amplifies the angular sweep from input (Joint 1) to output (Joint 3). Fig. 4.7a shows the actuator's linear velocity during periodic oscillations. All the joints experience angular velocities which vary in amplitudes. In Fig. 4.6b it is clearly visible how the kinematics of the system amplify the input angular velocity (Joint 1) into output angular velocity (Joint 3).

4.5.2 Free-Body Simulation of the Unactuated Wing Mechanism - Under Gravitational Restoration, Elastic Restoration, Friction and Air-Damping

4.5.2.1 Results

The animation in Fig. 4.8 shows the effect of damping on the system (air drag / friction). The wing-limb configuration finally stabilizes at the system equilibrium point (equilibrium between weight of the system and the spring restoring force).

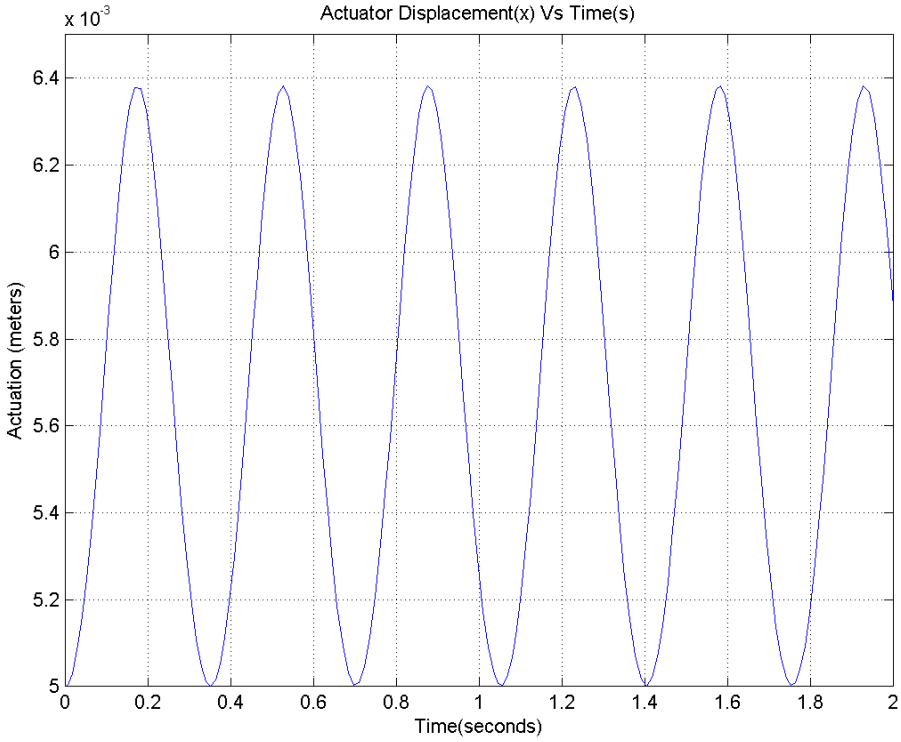

(a) Actuator displacement Vs Time

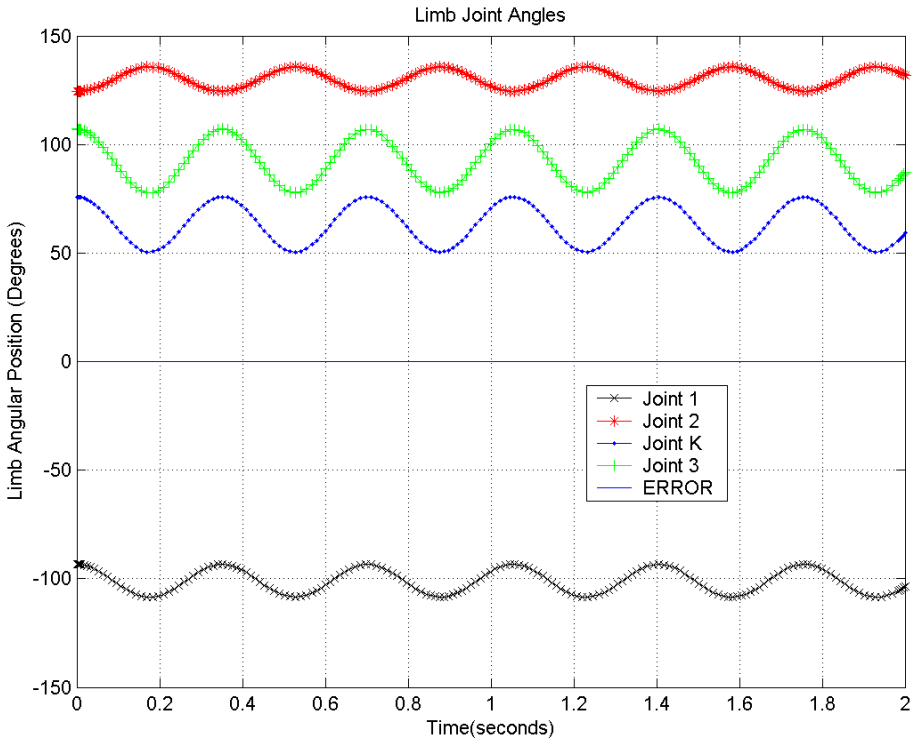

(b) Joint angular positions

Figure 4.6: Simulation results of the complex pendulum under gravitational restorative force

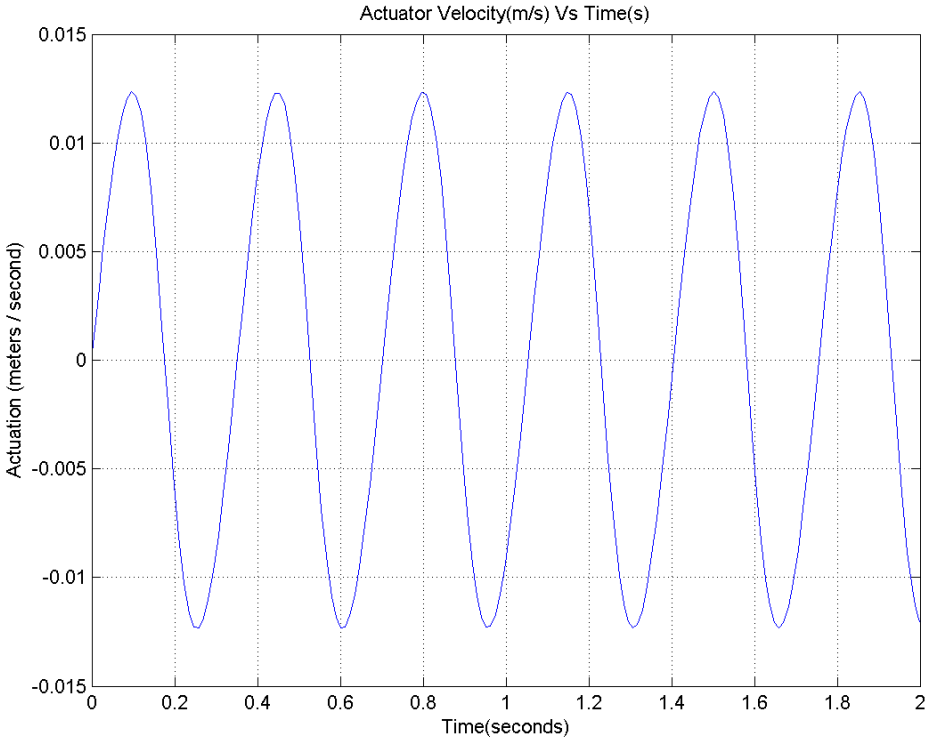

(a) Actuator linear velocity

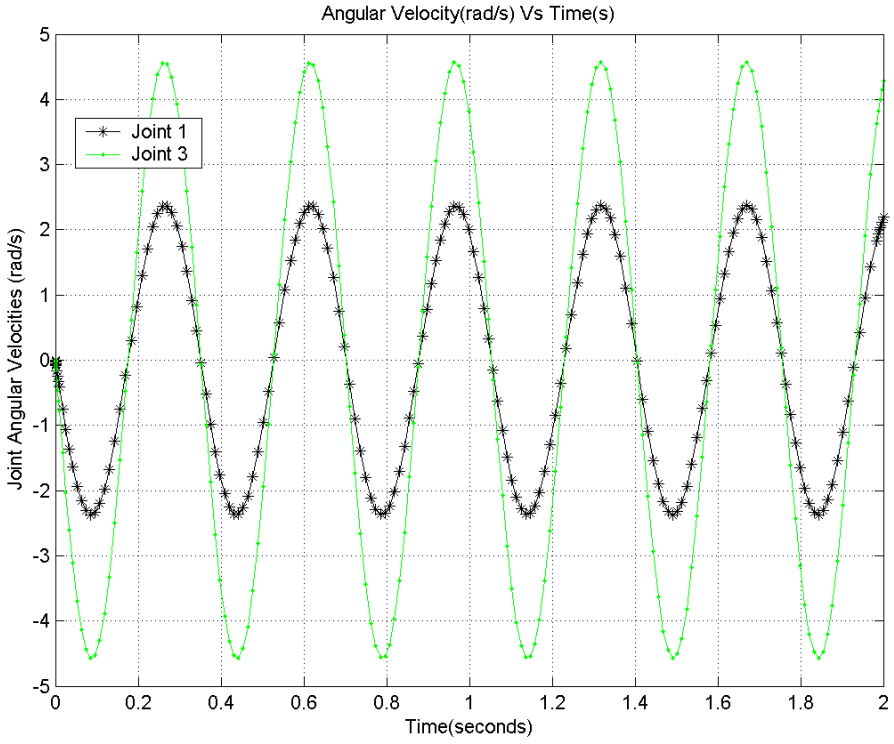

(b) Wing - Joint angular relationship

Figure 4.7: Simulation results of the complex pendulum under gravitational restorative force

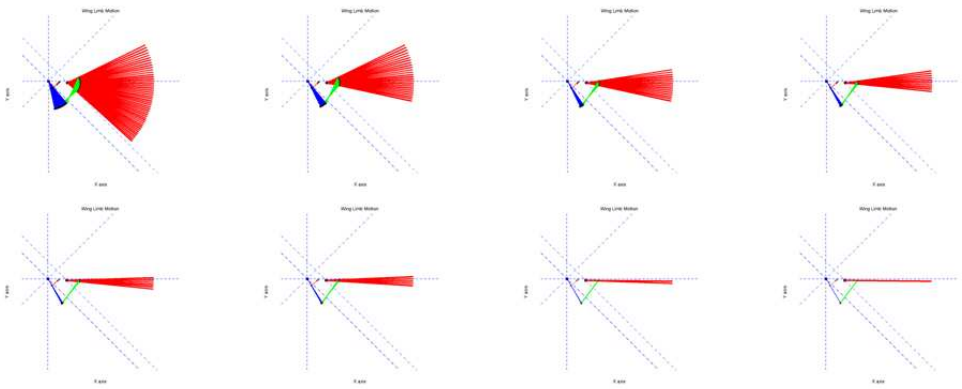

Figure 4.8: Damped Motion of the MAV Wing

- The actuator performed damped oscillations about the new system equilibrium point as shown in Fig. 4.9a. The frequency of the oscillations depend on the system dynamics. The damping is more prominent in the down-stroke of the wing. This is consistent with the fact that during down-stroke the wing has maximum drag and offers its full surface area to the wind. This stroke also produces almost all of the lifting force.
- As shown in Fig. 4.9b, the joints converged to their individual equilibrium angular positions.
- The flapping frequency for the system on an average is about 39Hz. The inertia of the system is not constant and dynamically changes over the range of motion, hence the flapping frequency which is dependent on the system restoring forces and inertia keeps changing dynamically as well. The thrust of the system non-linearly drops down to zero eventually as shown in Fig. 4.10a. The drop in thrust can be seen to be faster on the down-stroke than on the up-stroke. This further bolsters the fact that the damping is more pertinent in the down-stroke.

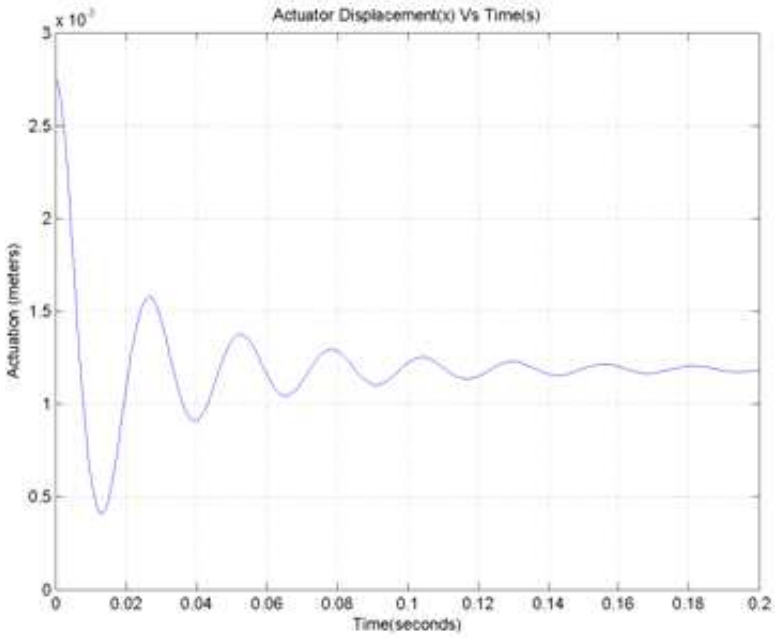

(a) Actuator displacement Vs Time

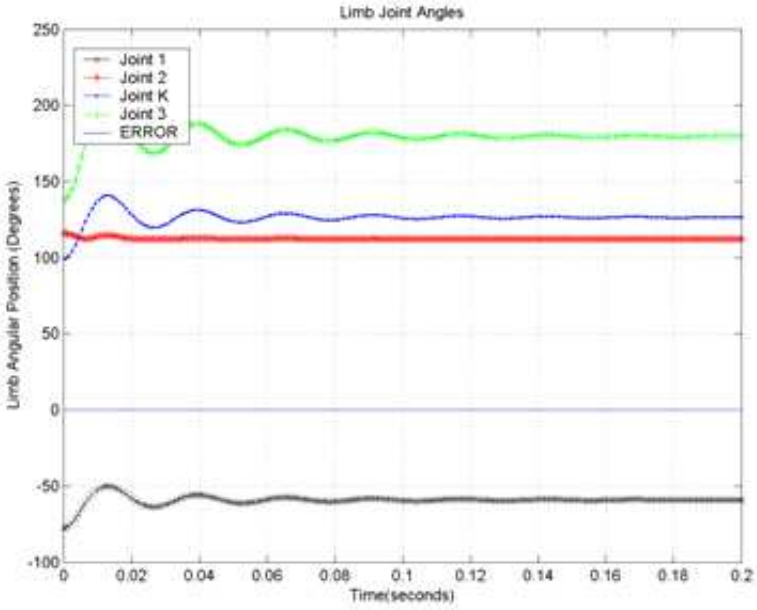

(b) Joint angular positions

Figure 4.9: Simulation results of the complex pendulum under air damping and mechanical friction

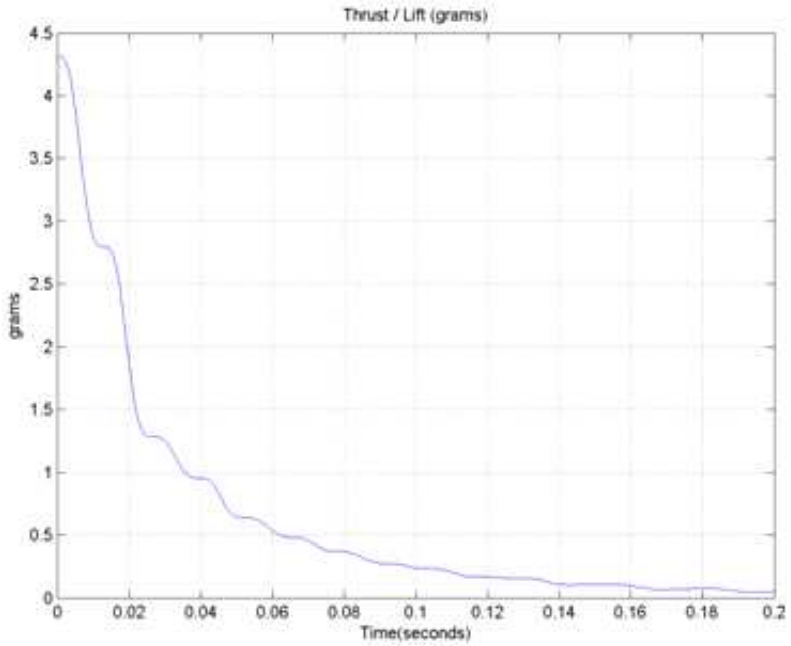

(a) Output thrust/lift produced by the wing (grams)

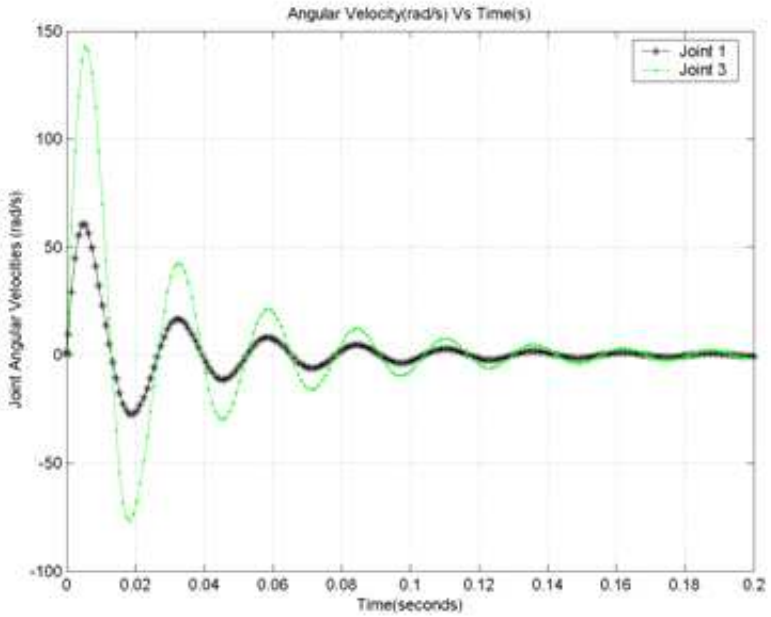

(b) Wing - Joint angular relationship

Figure 4.10: Simulation results of the complex pendulum under air damping and mechanical friction

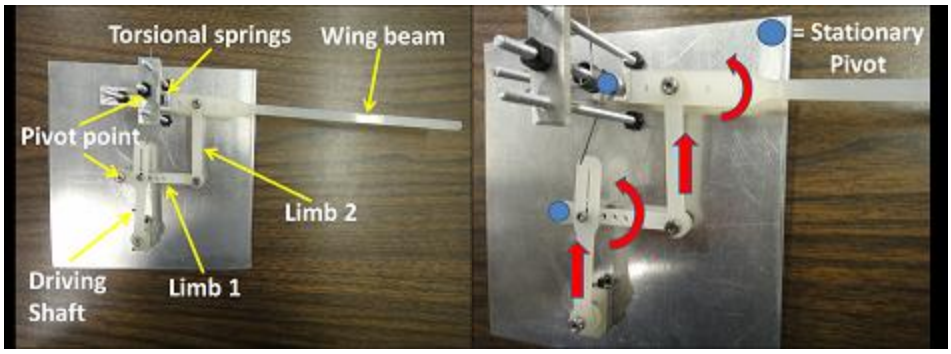

Figure 4.11: Four-Bar (Hard) Linkage Mechanism with Torsional Spring

The non-linear model simulation has shown promising results. The developed control algorithms and hybrid switching strategies have been described in the next section.

4.5.3 Linear Actuator - Four Bar Linkage

4.5.3.1 Hard Linkage

A four-bar linkage as shown in Fig. 4.11 with torsional springs at the wing base mechanically hard couples the actuator to the wing. The system is kinematically constrained to move as explained in Equations 4.4 and 4.24.

Remark 4.1. In general converting a linear actuation into a reciprocating-rotary actuation was replaced with other actuation mechanisms, since the inclusion of additional links and limbs to convert linear motion to reciprocating-rotary increased system weight, friction and mechanical complexity. Additionally the linear actuators were not high switching bandwidth capable, were output power/force deficient and required frequent re-tuning / maintenance.

Note 4.3. A compendium of actuation mechanisms and their developmental time line has been detailed in Chapter **??**. A complete comparison of various actuation mechanisms has also been presented therein.

4.6 QV CONTROL DESIGN CONCEPTION: 6 DOF FLIGHT MODES

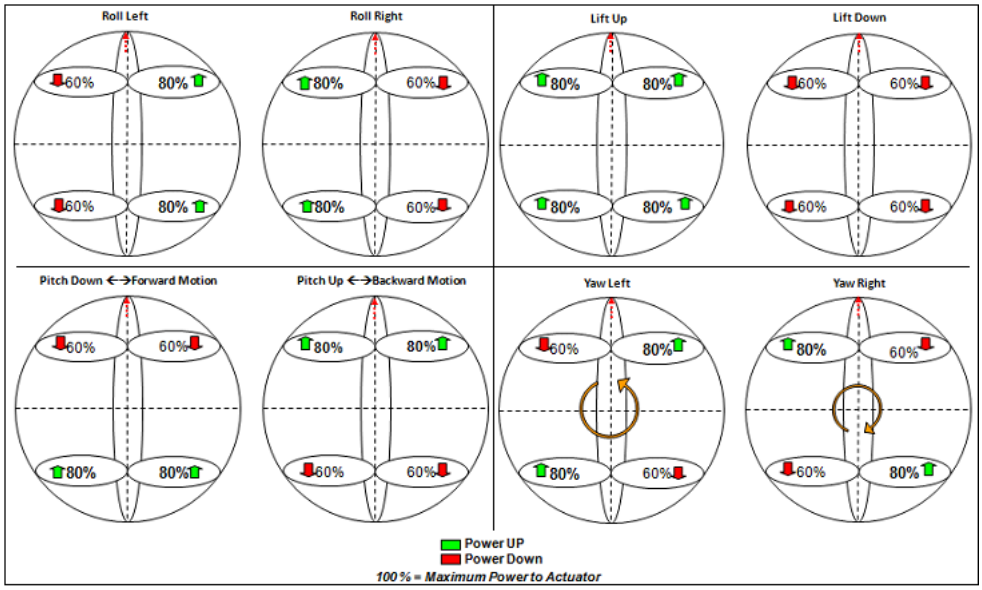

Figure 4.12: Flight Modes for the QV Design

Any flying vehicle should be capable of the basic 6 DoF flight. This is especially critical for indoor MAVs which fly in closed quarters with sharp turns and maneuvers. The three basic motions of any flying vehicle include Pitch, Roll and Yaw. In case of the QV conceptual design shown in Fig. 4.12, the in-flight control of these primitive motions can be accomplished by coordinating the power distribution to the individual wings. By powering up a given combination of wings, the vehicle can be made to perform primitive maneuvers. In the QV design, the primitive maneuvers are coupled to translational dynamics of motion. More on the flight modes is explained in the Section 4.6.2.

4.6.1 Hierarchical Control Scheme

The MAV control can be segregated into the flow diagram as shown in Fig. 4.13. The Mission module describes the global mission parameters to be met by the MAV, such as flying from point A to point B to point C, avoiding point D etc. The Path/Trajectory Planning module incorporates the above mission goals and assigns a trajectory to be followed to

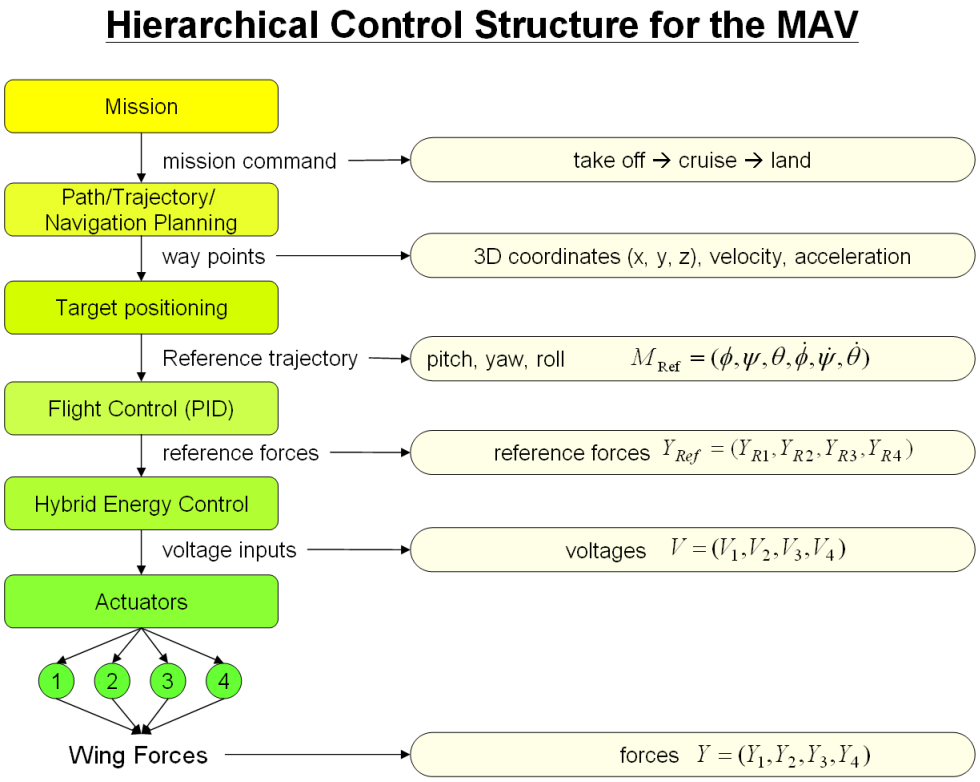

Figure 4.13: MAV Hierarchical Control Scheme

meet the mission goals. The Target positioning layer produces reference Euler angles and rates for the MAV to successfully follow the waypoints produced in the previous higher layer. The Flight Control layer is a linear controller, which matches the vehicles dynamic Euler angles and rates to conform to the reference values generated by the immediately upper layer. The Hybrid Energy Controller is responsible for sustaining oscillations about the wing-beat frequency. The energy controller controls the thrust produced by each wing by modulating the power output to each wing. There are four actuators in the system, which together control pitch (and forward/backward translation), yaw, roll (and left/right translation). More on the hybrid energy controller has been explained in Section .

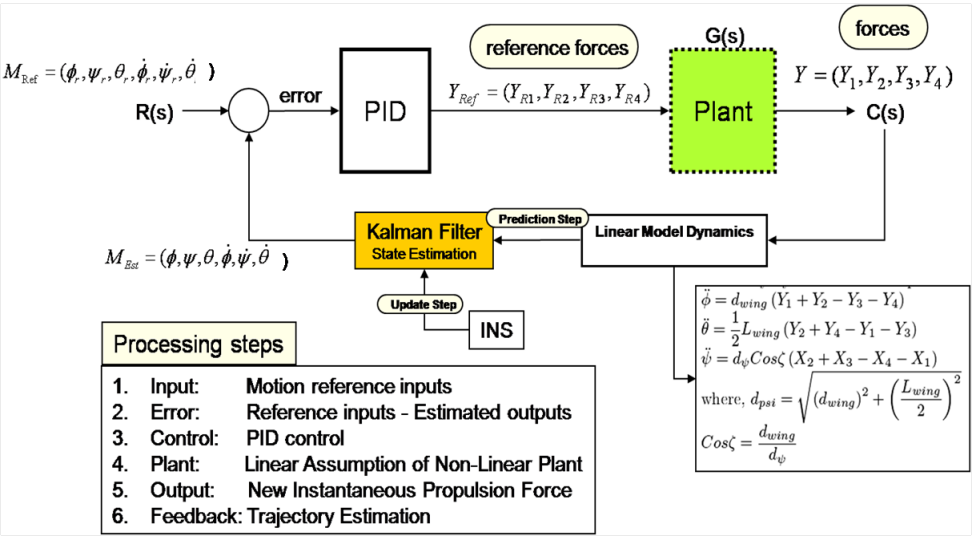

Figure 4.14: Multi-Loop Flight Control Scheme

4.6.2 Control System for the MAV

4.6.2.1 Mid-Level Linear System and Control

The flight control system comprises of a dual loop control system as shown in Fig. 4.14. Outer layer linear controller produces reference thrust values to be produced by the lower level hybrid energy controller. The linear model dynamics assume a symmetrical MAV configuration and predicts the angular parameters of the system, which are then updated by the estimation block. The Kalman Filter[3] acts as the sensor fusion block, which uses the sensor readings obtained from the GPS, gyroscopes, magnetometers, accelerometers etc to update the linear model predictions. This produces the instantaneous values of angular position and rates. The adder produces an error (differential) between the reference values and the actual values, which is fed into the linear controller for regulation.

4.6.2.2 Linear Modeling of the Mid-Level Dynamics

The modeling for each axis to determine the Euler Rates has been done by forming moment couples by two opposite ended forces Y1-Y2, Y3-Y4, in case of pitch control, Y1-Y3, Y2-

[3]Not Implemented yet. At present the sensor fusion block's output is simply the output of the Inertial Sensors, after the pre-filter.

Y4 in case of roll control and X1-X4, X2-X3 in case of yaw control, as shown in Fig. 4.15.

The most basic mid level model formulation has been done as shown in Eq. 4.27. The linear model has been further upgraded with air damping/drag, air disturbances and other non-linear external forces to converge to the most accurate model for controller development.

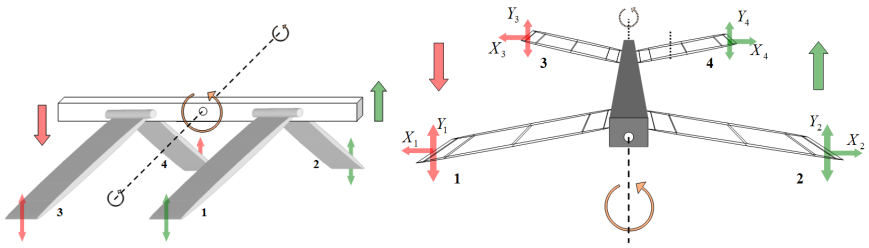

Figure 4.15: Linear Control Visualization

The opposing forces form Moment-Couples providing the necessary dynamic relationships:

$$\begin{aligned}
\ddot{\phi} &= \frac{d_\phi}{J_\phi}(Y_1 + Y_2 - Y_3 - Y_4) \\
\ddot{\theta} &= \frac{d_\theta}{J_\theta}(Y_2 + Y_4 - Y_1 - Y_3) \\
\ddot{\psi} &= \frac{d_\psi}{J_{psi}}(X_2 + X_3 - X_4 - X_1) \\
\ddot{z} &= \frac{1}{M_{MAV}}(Y_1 + Y_2 + Y_3 + Y_4)
\end{aligned} \tag{4.27}$$

where, J_ϕ, J_θ *and* J_ψ are the moments of inertia of the MAV about the three axes, and M_{MAV} is the mass of the MAV.

4.6.2.3 Low-Level Hybrid Energy Control

The MAV plant has been expanded for better understanding of the internals of the system. The plant can be seen to comprise the following as shown in Fig. 4.16:

1. The energy controller[2, 14], controls the actuators to produce sustained wing-beats.

2. The actuators, to connect to the four wings through associated mechanical linkages.
3. The wings, which will be used to produce the desired air-drag to generate lift.

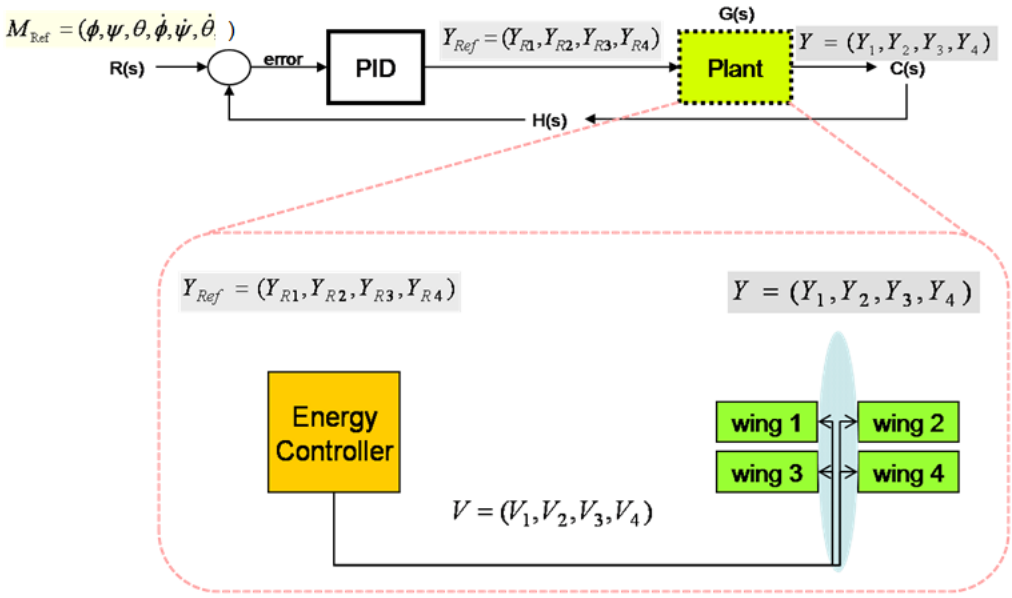

Figure 4.16: Hybrid Plant Architecture

The system energy is calculated from output - sensor feedback and internal sensor feedback for the system, by taking into accout the length & mass, angular position, spring extension and angular velocity of the wing. The interface of the non-linear controller can be seen from Fig. 4.16. The energy controller controls the power delivered to the actuators, in effect controlling the three body angular rates of the system. The control law used in[2] for achieving the desired energy has been shown here:

$$u = sat_{ng}\left(k\left(E - E_0\right) sign\left(\dot{\theta}_3 cos\theta_3\right)\right) \tag{4.28}$$

where, u is the control input (voltage) to the linear actuator. E is the Normalized Energy of the wing/spring combination and E_0 is the Desired Energy of the wing/spring combination, sat_{ng} puts a limit to the maximum actuation capability of the actuator, k is a design parameter. The result of the control law implementation on the actuation systems is the gradual

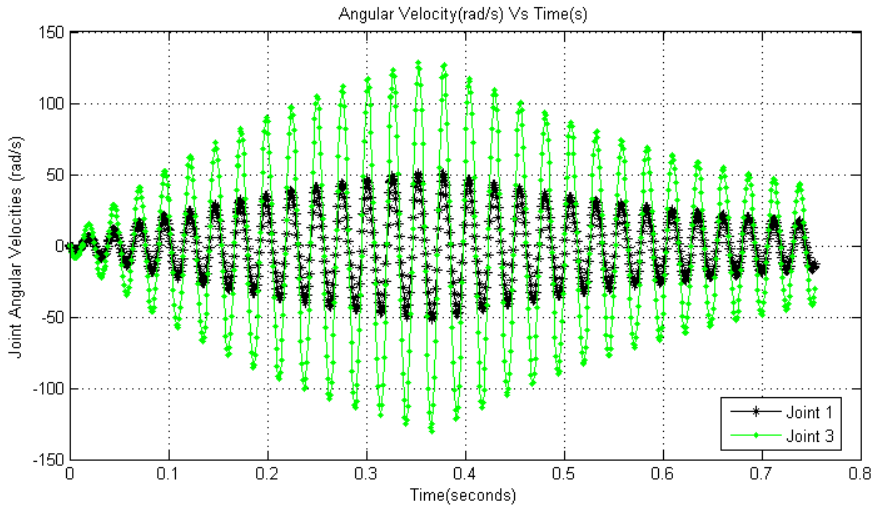

Figure 4.17: Angular velocity build-up in wing

build up of potential energy and in turn, kinetic energy (as seen from the increase/decrease of wing angular velocity, shown in Fig. 4.17).

4.7 SIMULATION RESULTS

The system step response for a given initial condition of $\phi_{Ref} = -12^o$, $\theta_{Ref} = 11^o$, $\psi_{Ref} = 11.5^o$ is shown in the Fig. 4.18 and Fig. 4.19. The MAV has also been commanded to maintain a level altitude of 20 cms above its launch position. The model has been described in Section 4.6.2.

4.7.1 Constant Gain: Manually Selected

The PID gains for the mid-level controller have been kept constant at reasonably agreeable values in the first controller and the system response for the above reference parameters is shown in Table 4.18. The five graphs show pitch, roll, yaw, altitude and actuator thrust response versus time.

4.7.2 GA Based Gain Tuning and Performance Improvement

Typically, the gains in the PI controller are adjusted by observing characteristic factors such as rising time, settling time and overshoot under a step response until the desired perfor-

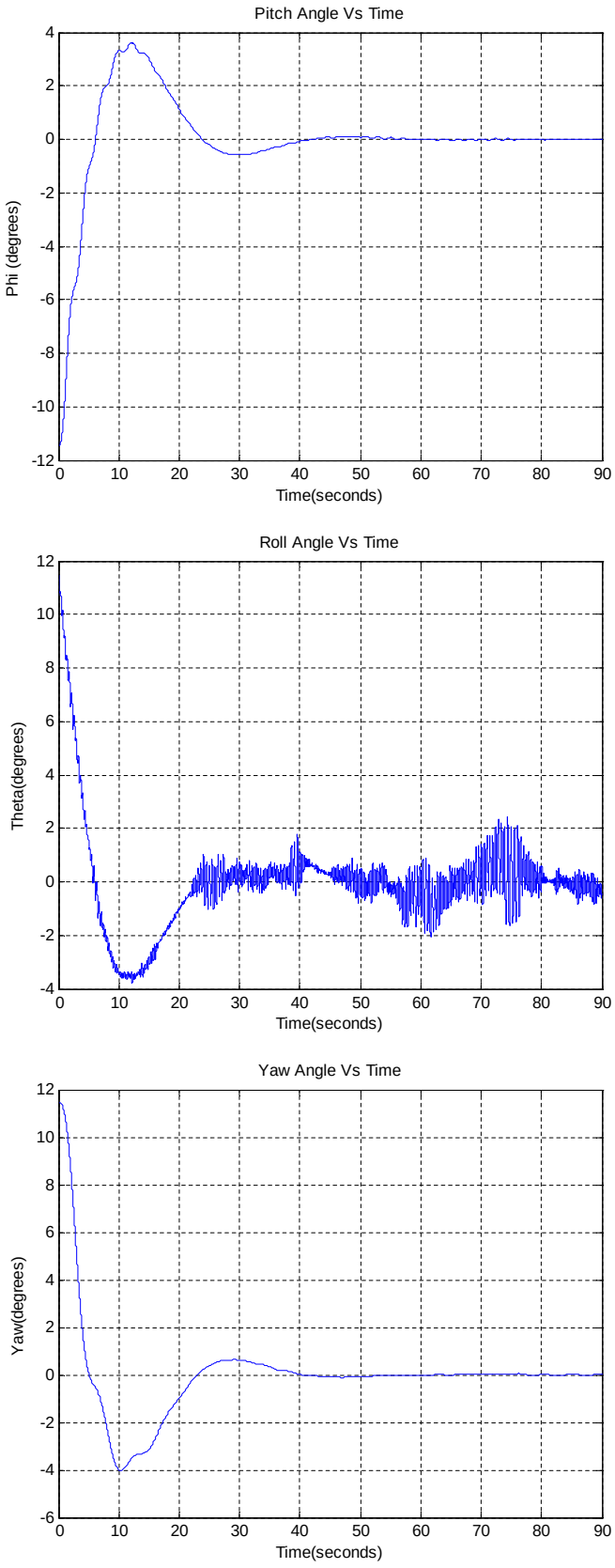

Figure 4.18: MAV Flight Control (Step Response): Manual PID gain selection

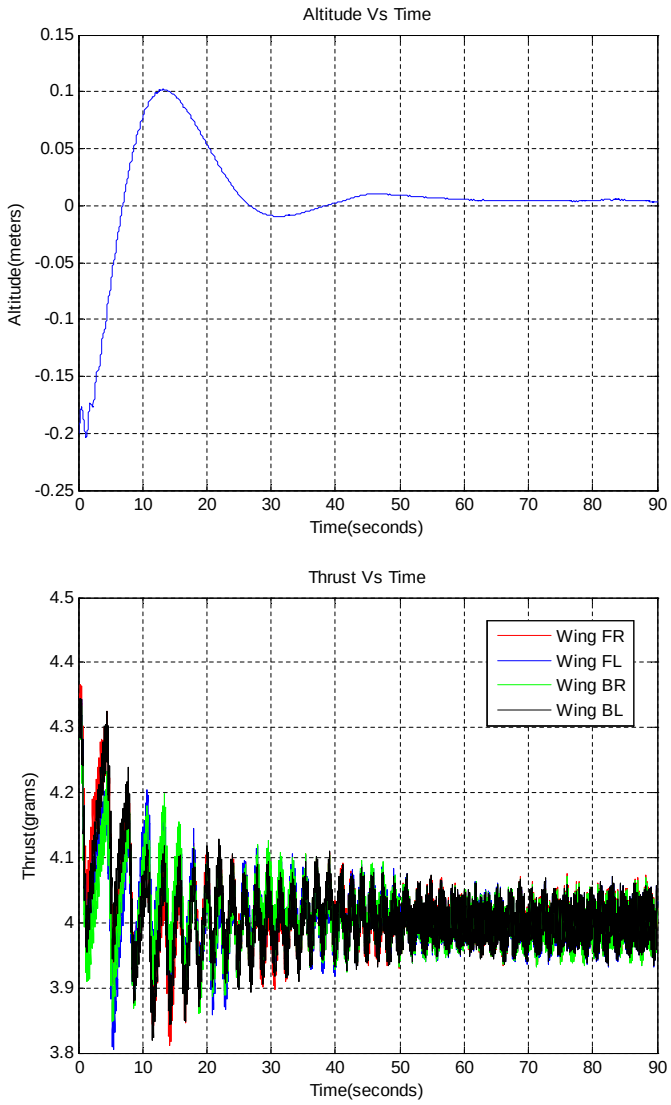

Figure 4.19: MAV Flight Control (Altitude Control and Actuator Output Lifts): Manual PID gain selection

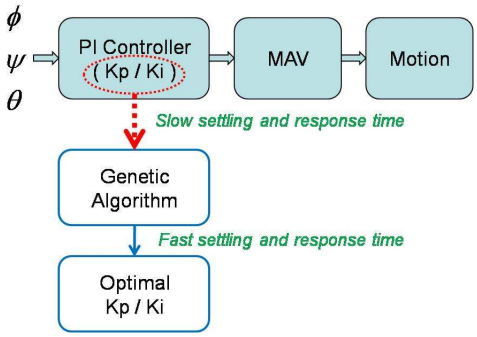

Figure 4.20: GA Tuning Block Diagram

Table 4.1: Gains (top down): Manual Selection, After GA tuning (6 Generations), After 96 Generations

PI Controller	Kp	Ki	Area Sum
Pitch	12.5	0.05	.3752
Roll	14	0.02	.3596
Yaw	7.3	0.05	0.5832

PI Controller	Kp	Ki	Area Sum
Pitch	8.3279	0.2546	0.5061
Roll	9.1720	0.0571	0.3506
Yaw	5.4359	0.0745	0.6380

PI Controller	Kp	Ki	Area Sum
Pitch	4.3874	3.2975	1.46E-12
Roll	6.3704	1.2216	1.29E-12
Yaw	2.4128	7.1614	0.00019

mance metrics are achieved. However, the QV system is highly non-linear and the driving mechanism is under-actuated as well, thus the choice of gains is highly experimental and can not guarantee satisfactory performance. In order to optimize the step response performance of the MAV, a good set of PI controller gains are necessary; the Genetic Algorithm (GA)[4] algorithm is applied towards that goal. The performance of the proposed system can be measured by the system response times to a step input.

Cost Metric: The cost function for the GA is defined as the cumulative area under the step response graph until the system settles down. The smaller the area, the faster the response time.

Generally, in order to apply the GA to a selection problem, the gene structure and evaluation method should be prepared; in this research, the set of PI gains is defined as a gene and the fitness function is defined as the cost metric. The crossover rates and the mutation rates are set as 100% and 10%, respectively. Table 4.21 highlights the results of gain tuning using the devised GA after 6 generations.

[4]The GA tuning was done along with Seong-Joo Kim (Visiting Scholar)

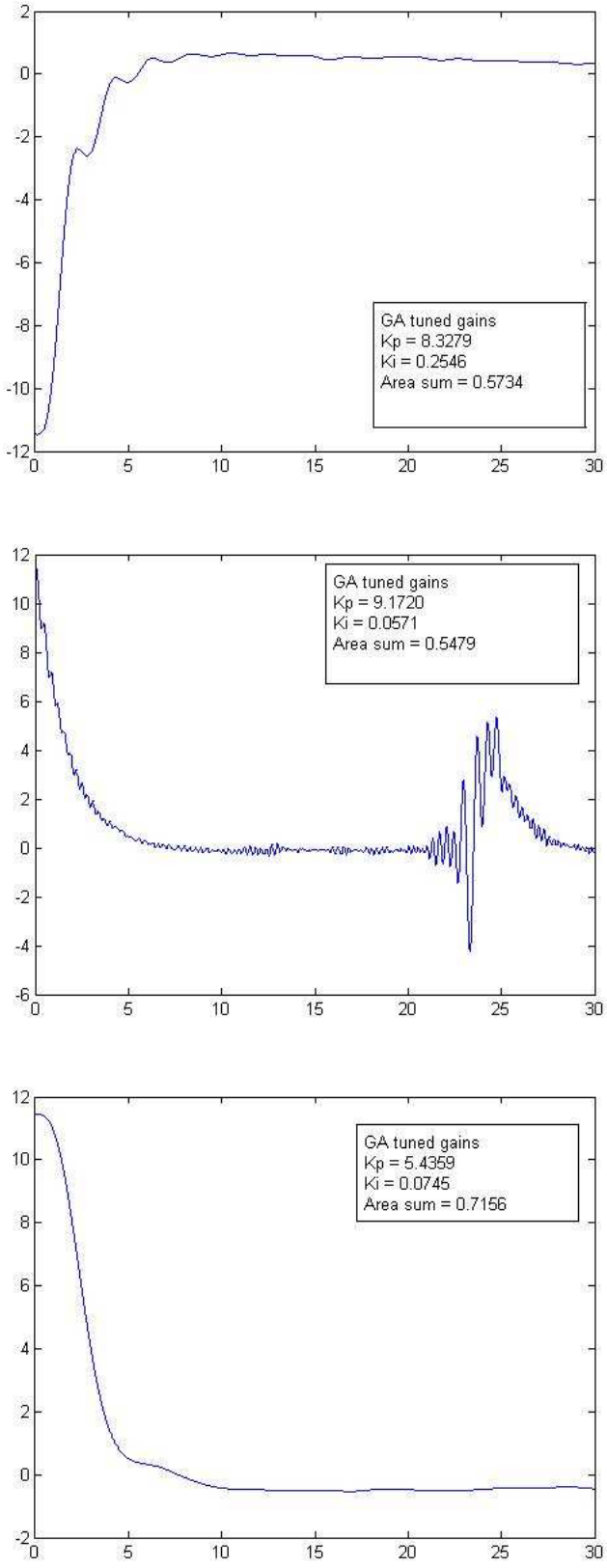

Figure 4.21: Linear Control / Hybrid Energy Control: step response: GA based PID gain selection (After 6 generations)

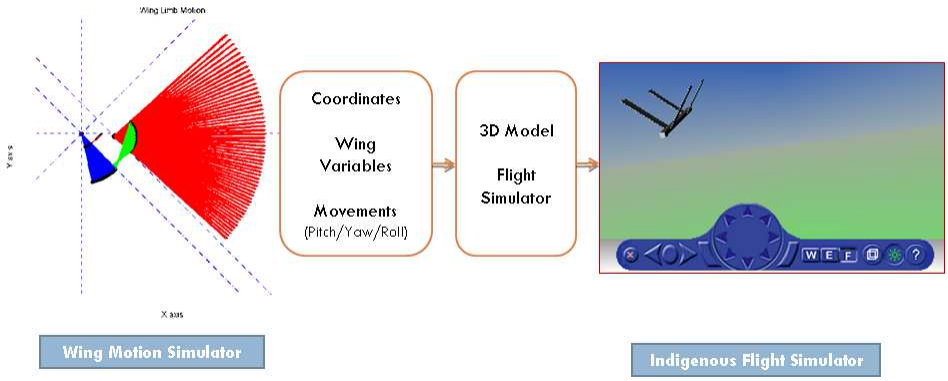

Figure 4.22: Wing Motion Simulator (MATLAB) and Flight Simulator (Simulink)

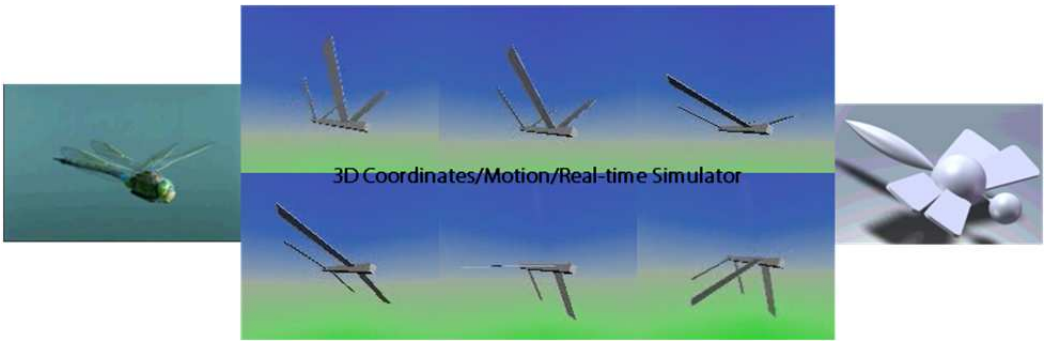

Figure 4.23: Inspiration to Design: Indigenous Flight Simulator in Simulink

There has been a marked performance improvement over manual gain selection. Settling time for manual selection was about 50~60 seconds to start with, with an overshoot of approximately 4 degrees. The GA based gain tuning had 0 degrees overshoot and the settling time has been reduced to approximately 5 seconds. The step response after GA tuning conforms to a critically damped system and has shown very promising results.

4.7.3 Visualization Environment and Simulation

The indigenous flight simulator / visualization environment has been shown here[5]. The wing simulator was made in MATLAB and the visualization was made in Simulink using the Virtual Reality Toolbox.

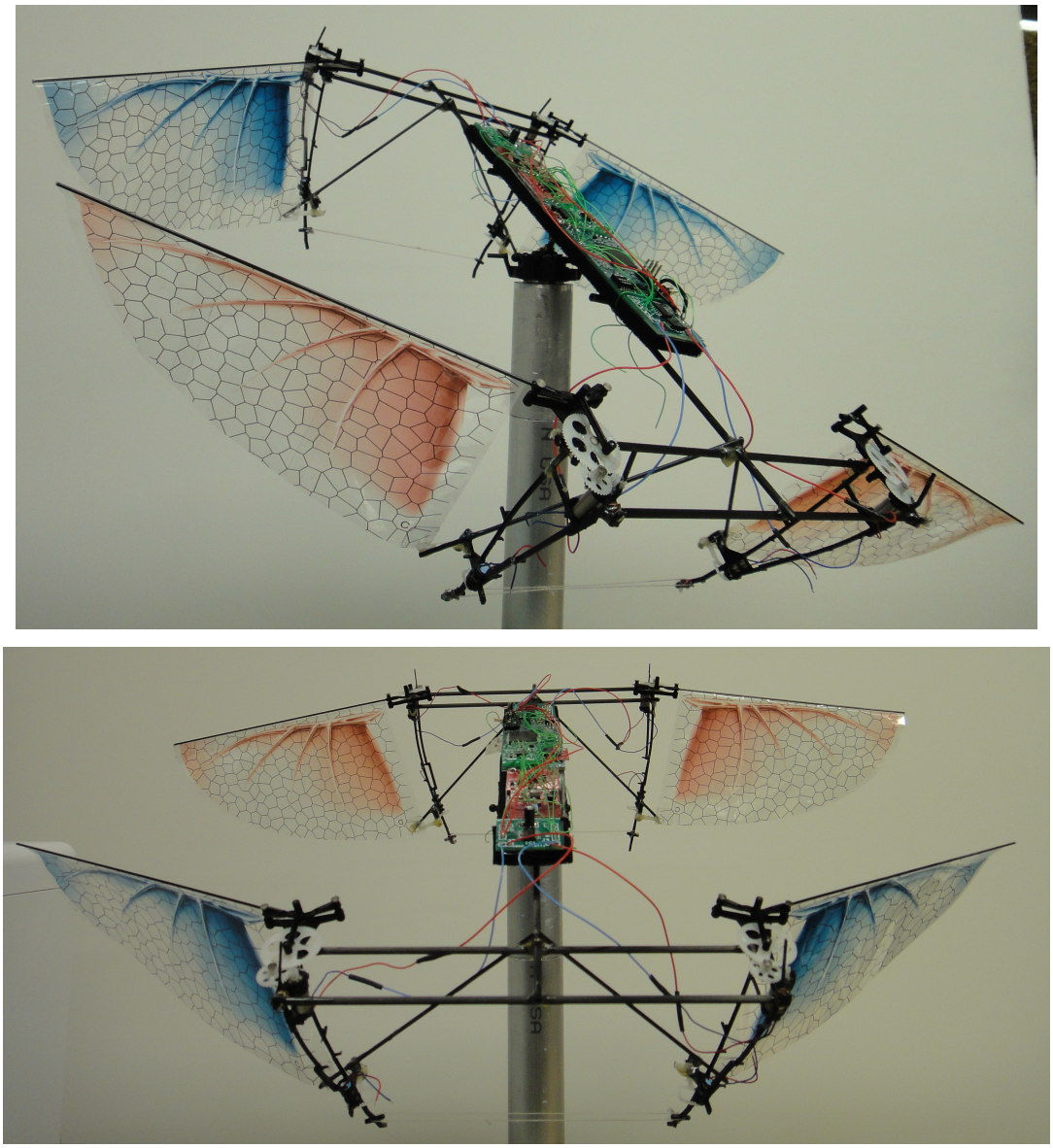

Figure 4.24: 3DoF Benchtop Prototype

4.8 3DOF TESTING OF THE FIRST MAV PROTOTYPE

A Test-Bench Simulator, shown in Fig. 4.24, has been designed to perform 3DoF motions and maneuvers. The goal is to test different control algorithms and their performance on a bench top setup without the need to initially subject the prototype to unnecessary wear and tear, crashes and in-flight failures. The vehicle has been since made 6DoF-capable by the installation of an indigenous, low weight Autopilot [40]. The design and construction of the autopilot has been presented in Appendix A.4 and briefly described in the following sub-section.

4.8.1 Embedded Flight Control System

To initiate testing of the MAV configuration an autopilot was required to be customized. Commercial Off the Shelf (COTS) autopilots were impractical due to their bigger size and power requirements and limited computational resources. Two indigenous autopilots (MARC-1 and MARC-2[6] were developed to facilitate embedding the control system on-board the MAV and interfacing it with a ground station.

4.8.1.1 Avionics Design

Fig. 4.25 shows the outline of the embedded hardware on-board the MAV. The selection of the processors for this embedded device involved many important considerations such as power consumption, size/weight and performance. The system is a twin-processor design with an inter-connected FPGA and DSP. The FPGA acts as the integrator and is used to implement various tasks like glue logic, control logic, custom IP and hardware-accelerators for computationally intensive algorithms. The FPGA also carries out low-level repetitive functions thus helping to improve the system performance considerably by freeing up the DSP from cycle-intensive tasks. The DSP carries out high-level flight controls, navigation and image/video processing. The FPGA and DSP combination in the design provides

[5]The simulink visualization was prepared in conjunction with Seong-Joo Kim (Visiting Scholar)
[6]Micro Architecture and Control (MARC)

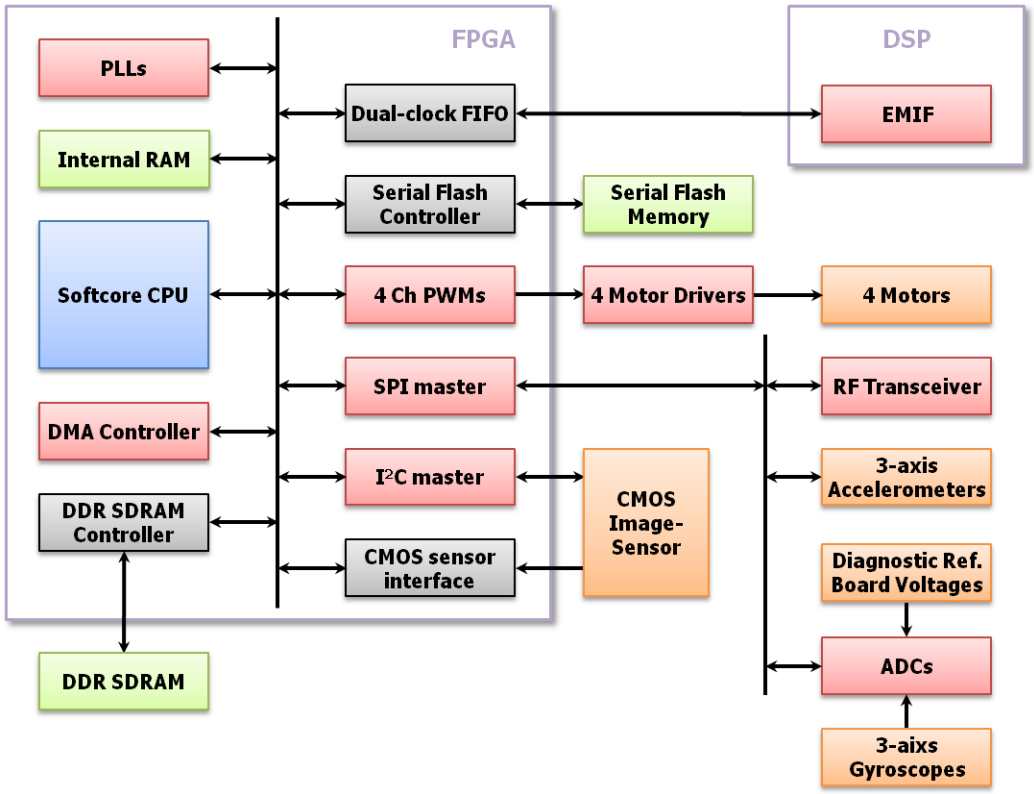

Figure 4.25: Embedded Hardware Architecture for the MARC-2 board

excellent performance characteristics and much flexibility to accommodate changing standards and component upgrades.

The FPGA[7,8], hosts a 32-bit softcore NiosII CPU, a DMA controller, a DDR RAM controller, an internal RAM, four digital PLLs, and all communication interfaces required for connecting external peripherals to the softcore CPU. The first round of experiments were carried out with the MARC-1 autopilot as shown in 4.26. However, the MARC-2 board was used to test the Flight Time increase of the 4-Wing configuration (since the MARC-2 consumed significantly more power than the MARC-1 (Ref. Appendix A.4, [40]).

4.8.2 Signal Conditioning

The inertial sensor inputs was seen to be quite noisy. The motors produced a significant amount of vibration due to their asymmetric flapping motion. The vibrations were seen to

[7]The sofware coding for the MARC-2 board was done by Jung Ho Moon
[8]The sofware coding for the MARC-1 board was done by David Smith

Figure 4.26: MARC-1 (dsPIC33F) Single Core

Figure 4.27: MARC-2 (Cyclone III, TI 55xx DSP) Dual Core

decrease with higher frequency flapping, but on the test runs the flapping frequency was rather small (lying in the range of 10 to 30Hz, as shown in Fig. 4.28) therefore a pre-filter (Fig. 4.29) was designed to filter input signal prior to sensor calibration and feeding the control system.

The output of the pre-filter is as seen in Fig. 4.30. A pre-programmed motion was executed using a continuous bang-bang operation of the Pitching motion for 15s, then Roll motion for 15s, followed by 15s of Yaw motion. The results are shown in Fig. 4.30.

4.8.3 Control System Execution and Testing

The testing was carried out first with a PD controller[9]. The step response was seen to produce an overshoot of about 6^o and a settling time of 2.5s, as shown in Fig. 4.31. The next testing was carried out with a PD controller again but with better gains; the system as shown in Fig. 4.32 was shown to completely eliminate overshoot and reduce settling time to 1.25s. Both gains were used with an initial deflection of about 25~30 degrees and the reference position was kept at 0^o.

[9]The control system testing was done along with David Smith

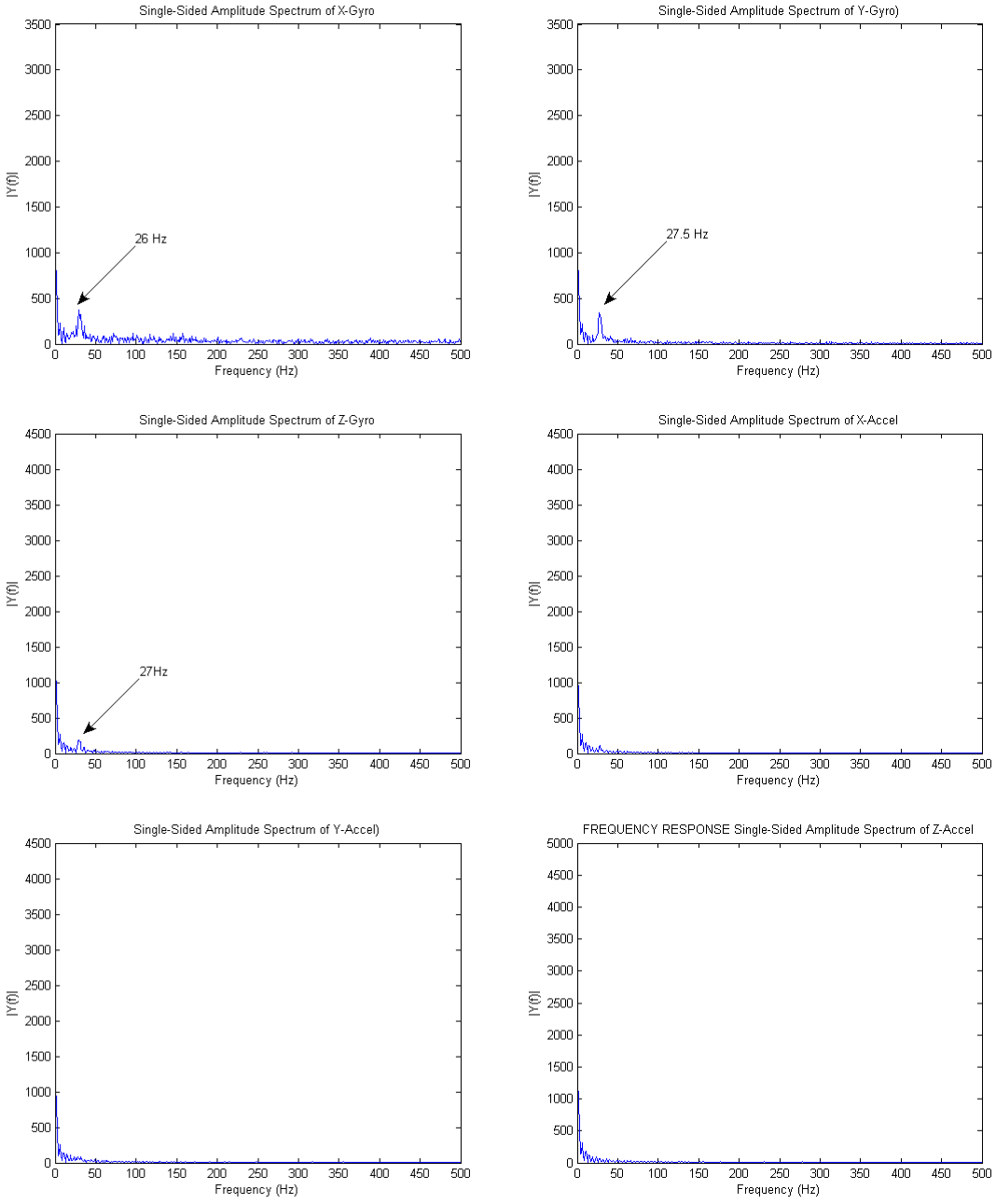

Figure 4.28: Frequency Response of Input Signals

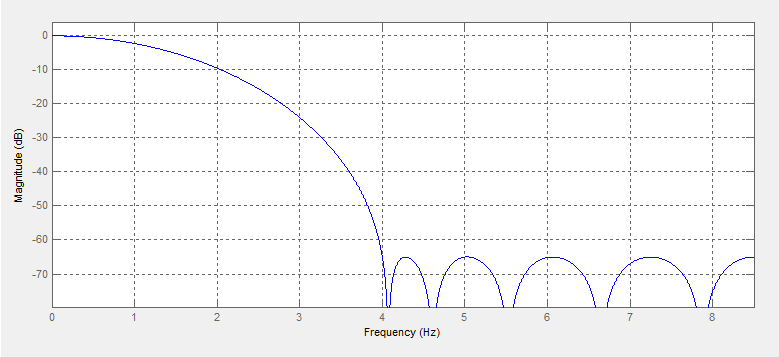

Figure 4.29: Pre-Filter Design: F_{Stop}= 0.01Hz, F_{pass}= 4Hz, F_{Sample}= 17Hz, 10^{th} Order FIR Filter, W_{pass}= 20db, W_{Stop}= 80db

Note 4.4. It was seen that even without the integral term, the system still settled to its reference position most of the times but not always.

We see that the system response is very impressive, the output response is 2.5 times faster than that predicted in the simulation model for the PD controller and was later improved to be 4 times faster with better gains.

4.9 CHAPTER CONCLUDING REMARKS

The non-linear model is seen to comply with physical non-linear complex pendulum physics very closely. The simulation of the non-linear model of the wing with spring restoration, gravity, air damping, joint friction was carried out and the result was seen to comply with a damped, un-actuated harmonic oscillator. The results complied with practical observations and published literature on the subject.

The non-linear wing model was successfully tested in simulation using Hybrid Energy Controller so proposed. The wing system was made to build up energy (and in turn lift) and also dampen energy (and in turn reduce lift) using the Energy Controller. The energy control was complemented with defining a novel control scheme to achieve all 6DoF flight control on the four-wing MAV configuration so proposed. The simulation results demonstrated the efficacy of the control scheme in generating various flight modes (pitch, roll,

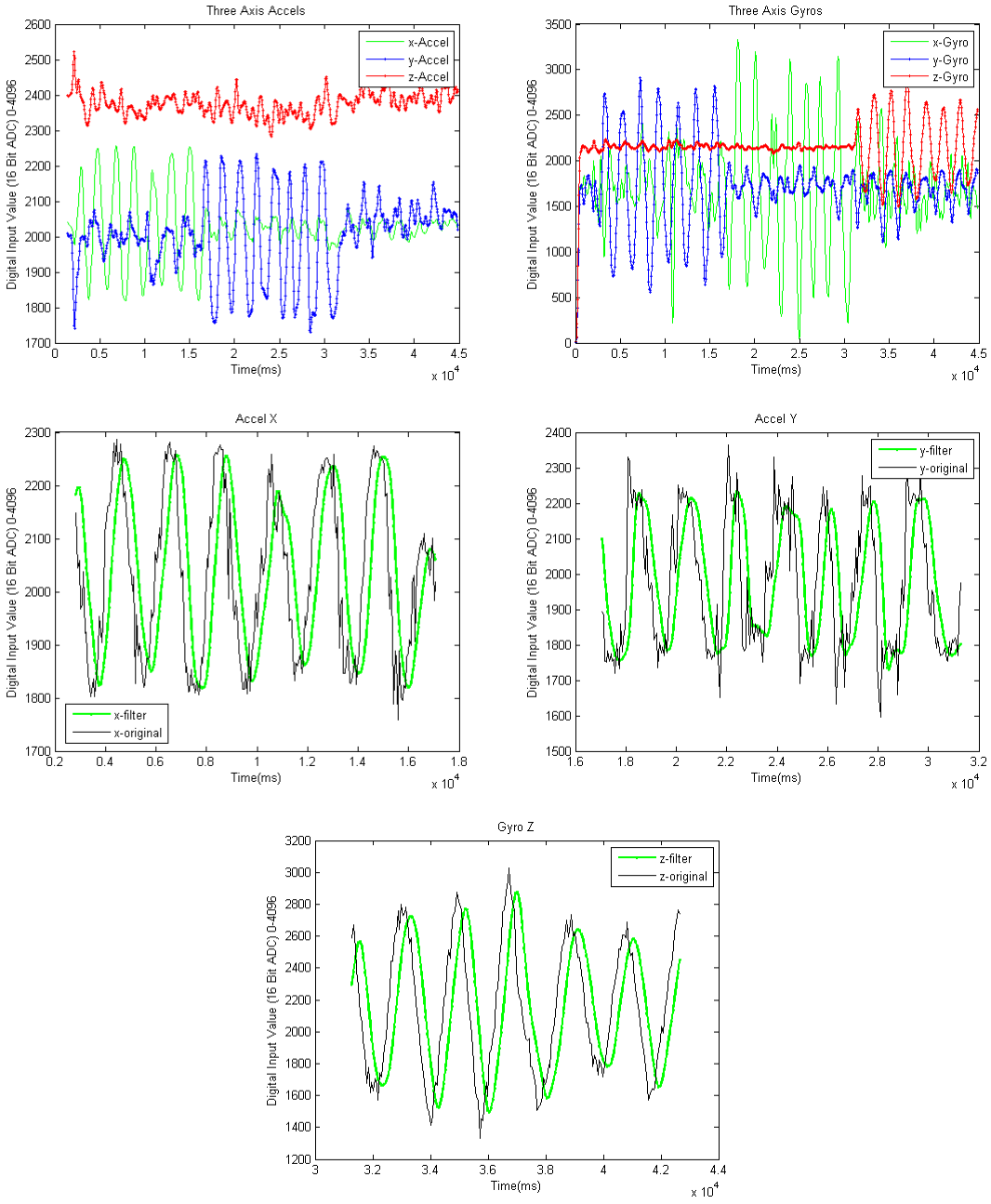

Figure 4.30: Inertial Sensor Inputs (Raw and Filtered)

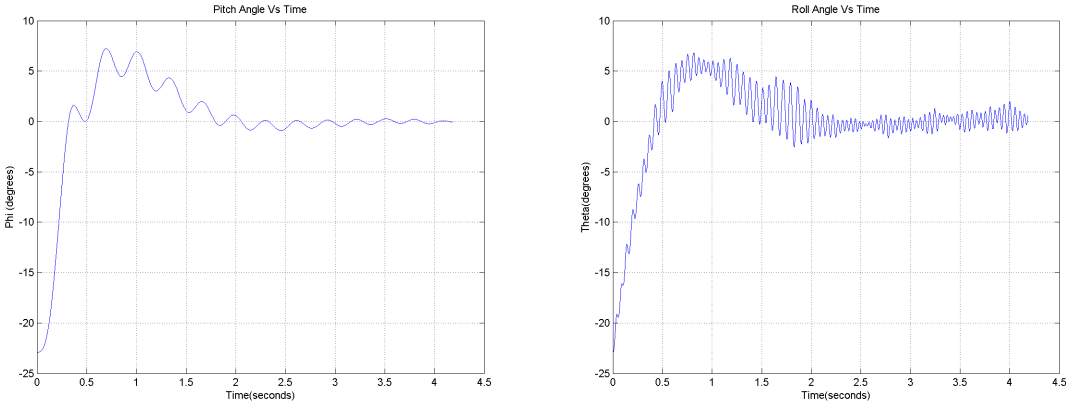

Figure 4.31: Step Response: PD Controller - Initial Gains

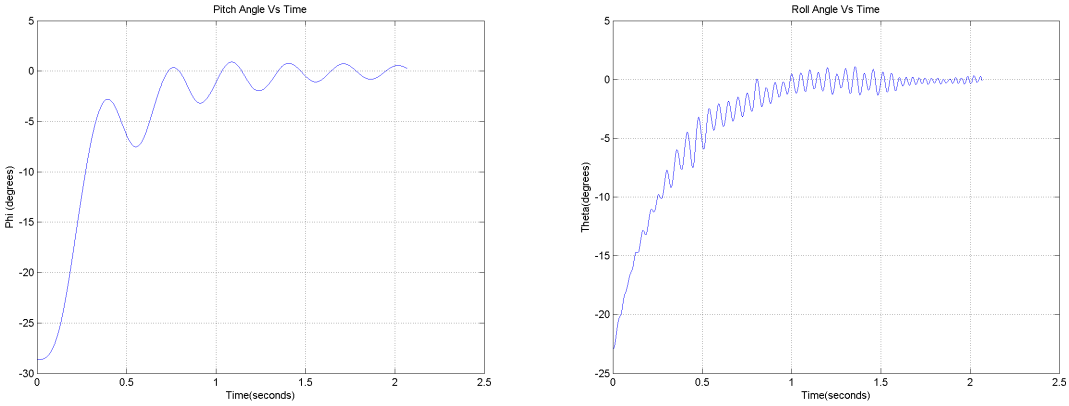

Figure 4.32: Step Response: PD Controller - Final Gains

yaw and 3D translation). The step responses of the MAV system were seen to stabilize the MAV system and bring it to equilibrium. The GA based PID gain selection improved on the manually tuned gains by reducing the settling time and step-overshoot to that shown by a critically damped system. The gains so produced through the GA showed a 10 fold performance increase over manually selected gains.

The discussion was carried towards showing the efficacy of implementing the control scheme on two indigenously developed autopilot systems (MARC-1 and MARC-2). The flight control was finally tested on a benchtop hardware simulator with a ball and socket joint to provide 3DoF flight capability, showing the basic Euler angle control. The control system was seen to stabilize the MAV in two experiments, through the use of PD controller in 2.5s and 1.25s respectively.

CHAPTER V

CONCLUSIONS

The energy dynamics of a Four-Wing flapping MAV design was compared to present day 2-Wing flapping configurations. In Chapter 2 it was proved that the energy increase in a Multi-Wing design is seen to be quite significant, spanning to even 400% and above over that shown by a 2-Wing configuration. The experimental results complied very closely to the theoretical predictions. In particular it was shown how the Quad-Wing MAV (QV) system, is capable of improving on-board energy reserves on MAVs.

Efforts to improve actuation power efficiency were undertaken by studying and employing passive elastic spring elements in the actuation mechanism. In Chapter 3, spring inclusion showed higher output torque requirement for non-spring jointed wings over spring-jointed flapping mechanisms, spanning to 100% and above in many cases. The power efficiency improvement was shown to hold experimentally as well. To demonstrate the use of springs, the wings are required to flap in resonance using a new flapping scheme called, FiFVA. In Chapter 3, the Fixed Frequency, Variable Amplitude (FiFVA) actuation was engineered and used to successfully demonstrate the possibility and effectiveness of replicating insect-like wing flapping. The comparison of all developed designs was made and presented in Table 3.4[1]. Two new actuation systems, namely the SOLO and the MorphES were engineered towards facilitating resonance flapping in wings of MAVs.

In Chapter 4, a novel control methodology to produce all 6DoF in-flight maneuvers was developed for the QV design; The 6DoF flight control was tested and demonstrated in simulation. Additionally, 3DoF flight results were also demonstrated on a functional four-wing MAV benchtop prototype, by controling all three Euler angles on the MAV.

[1]The performance was measured keeping weight of the actuation systems nearly uniform across different mechanisms during design

The wings of the MAV are modeled computationally using ANSYS / Fluent and run through a series of kinematic parameter sweeps, as shown in Appendix A.2. The results of the parameter sweeps clearly show that a very high feathering angle is desirable in hovering mode, producing the greatest net lifts. The optimal flapping amplitude, frequency however depends on the application and power availability. The lift / thrust results were shown to improve for higher flapping frequencies. For stable hovering performance, the unique QV control scheme to achieve 6DoF flight was presented. It was concluded that by orienting the wings such that the resultant force vector from the lift and thrust components of the wing points vertically downwards, the horizontal force losses in the plane of the QV will be minimized. This greatly improves lift performance and 6DoF control. Additionally, a robust flapping / feathering test bench was fabricated and tested to produce different kinematic wing motions.

In addition, two miniature autopilot systems were developed and utilized towards embedding the proposed flight control scheme on the self-powered QV benchtop prototype. The autopilots were very low on power consumption and weight, specifically customized to be used on the QV-MAV.

The research successfully demonstrated energy efficiency improvement in MAVs by the inclusion of elastic members in the actuation system, towards elastic re-use of potential energy in the system at resonance. On-board energy harvesting improvement (and/or payload increase/improvement) for MAVs was shown by doubling the actuation unit on 2-Wing MAVs, making them into 4-Wing MAVs. The result was an increase in flight endurance and payload capacities on MAVs. A novel 6DoF flight control methodology for the Four-Wing MAV was developed and tested in simulation and was shown to control all three basic Euler angles on the QV-MAV benchtop prototype.

APPENDIX A

THE APPENDIX

The appendix is structured using chapters, sections, sub-sections and sub-sub-sections as in the main body.

A.1 WING KINEMATICS

A.1.1 Derivation of θ', θ'' and θ'''

Assuming here the global origin O_o = $(0,0)$, we can extrapolate the variables as below:

$$d_{05} = \sqrt{x_5^2 + y_5^2}$$

$$d_{05'} = \sqrt{x_{5'}^2 + y_{5'}^2}$$

$$l_4 = d_{04}, x = d_{55'}$$

$$Cos\,\theta' = \frac{d_{05}^2 + l_4^2 - d_{45}^2}{2.d_{05}.d_{04}} \tag{A.1}$$

$$Cos\,\theta'' = \frac{d_{05}^2 + d_{05'}^2 - x^2}{2.d_{05}.d_{05'}} \tag{A.2}$$

$$Cos\theta''' = \frac{x_5}{d_{05}} \tag{A.3}$$

where, θ' is found from $\triangle 045$, θ'' is found from $\triangle 055'$ and θ''' is found from $\triangle 05x_5$.

A.1.2 Displacement Analysis Derivation

$$\bar{\theta_1} = \pi + \theta_1 \tag{A.4}$$

$$\bar{\theta_2} = -\theta_2 \tag{A.5}$$

$$\bar{\theta_k} = -\theta_k \tag{A.6}$$

$$\bar{\theta_3} = \pi + \theta_3 \tag{A.7}$$

$$\begin{bmatrix} x_0 - x_3 \\ y_0 - y_3 \end{bmatrix} = \begin{bmatrix} L_3\bar{C}_3 + L_2\bar{C}_{3+k} + L_1\bar{C}_{3+k+2} \\ L_3\bar{S}_3 + L_2\bar{S}_{3+k} + L_1\bar{S}_{3+k+2} \end{bmatrix} \tag{A.8}$$

Taking x_0 and $y_0 = (0,0)$, then

$$\begin{bmatrix} x_0 - x_3 - L_1\bar{C}_1 \\ y_0 - y_3 - L_1\bar{S}_1 \end{bmatrix} = \begin{bmatrix} L_3\bar{C}_3 + L_2\bar{C}_{3+k} \\ L_3\bar{S}_3 + L_2\bar{S}_{3+k} \end{bmatrix} \tag{A.9}$$

$$\bar{C}_k = \frac{\left(x_3 + L_1\bar{C}_1\right)^2 + \left(y_3 + L_1\bar{S}_1\right)^2 - L_3^2 - L_2^2}{2L_2L_3} \tag{A.10}$$

$$\bar{S}_k^{\pm} = \pm\sqrt{1 - \bar{C}_k^2}$$

Ignoring the positive sign, because $\bar{\theta}_k$is always negative in our configuration:

$$\bar{S}_k = -\sqrt{1-\bar{C}_k^2} \tag{A.11}$$

$$\bar{\theta}_k = atan\left(\bar{S}_k, \bar{C}_k\right) \tag{A.12}$$

$$L_1 Cos\theta_1 + L_2 Cos(\theta_1+\theta_2) = (x_3 - x_0) + L_3 Cos\bar{\theta}_3 \tag{A.13}$$

$$L_1 Sin\theta_1 + L_2 Sin(\theta_1+\theta_2) = (y_3 - y_0) + L_3 Sin\bar{\theta}_3 \tag{A.14}$$

$$[L_1 Cos\theta_1 + L_2 Cos(\theta_1+\theta_2) - (x_3 - x_0)]^2 + [L_1 Sin\theta_1 + L_2 Sin(\theta_1+\theta_2) - (y_3 - y_0)]^2 = L_3^2$$

$$L_1^2 + L_2^2 + 2L_1 L_2 Cos\theta_2 = x_3^2 + y_3^2 + L_3^2 + 2L_3 x_3 Cos\bar{\theta}_3 + 2L_3 y_3 Sin\bar{\theta}_3 \tag{A.15}$$

$$\bar{C}_3 = \frac{\begin{vmatrix} -x_5 - L_1\bar{C}_1 & -L_2\bar{S}_k \\ -y_5 - L_1\bar{S}_1 & L_3 + L_2\bar{C}_k \end{vmatrix}}{\triangle} \tag{A.16}$$

$$\bar{S}_3 = \frac{\begin{vmatrix} L_3 + L_2\bar{C}_k & -x_5 - L_1\bar{C}_1 \\ L_2\bar{S}_k & -y_5 - L_1\bar{S}_1 \end{vmatrix}}{\triangle} \tag{A.17}$$

where, $\nabla = L_3^2 + L_2^2 + 2L_2 L_3 \bar{C}_k$

$$\bar{\theta}_3 = atan\left(\bar{S}_3, \bar{C}_3\right) \tag{A.18}$$

$$\bar{\theta}_2 = \bar{\theta}_1 - \bar{\theta}_k - \bar{\theta}_3 \tag{A.19}$$

A.1.3 Derivation of Angular Velocities

Now we can have from equation 4.1, $Cos\theta_1 = Cos(\theta' + \theta'' + \theta''')$

We substitute the values of $Cos\theta'$, $Cos\theta''$ and $Cos\theta'''$ as derived in the appendix, into the above equation to result in $Cos\theta_1 = f_1(x)$, since all sub-angles are functions of the solenoid's travel x. Which results in the angular velocity of joint 1 or $\dot{\theta}_1$

$$\dot{\theta}_1 = -\frac{\dot{f}_1(x)\dot{x}}{Sin\theta_1} \tag{A.20}$$

Also

$$Cos\bar{\theta}_2 = Cos(\bar{\theta}_1 - \bar{\theta}_3 - \bar{\theta}_k)$$

where, $\bar{\theta}_2$ is derived from θ_2, as shown in appendix.

As also seen under displacement analysis, we can solve for $\dot{\bar{\theta}}_2$ and in effect $\dot{\theta}_2$. $\dot{\bar{\theta}}_2$ can be also seen to be a function of the solenoid travel variable x, hence it can also be expressed in the form below.

$$\dot{\bar{\theta}}_2 = -\frac{\dot{f}_2(x)\dot{x}}{Sin\bar{\theta}_2} \tag{A.21}$$

From the displacement analysis Equations 4.2, we derive the following differential equations:

$$L_1 Sin\theta_1\dot{\theta}_1 + L_2 Sin(\theta_1+\theta_2)\left(\dot{\theta}_1+\dot{\theta}_2\right) = L_3 Sin\theta_3\dot{\theta}_3 \tag{A.22}$$

$$L_1 Cos\theta_1\dot{\theta}_1 + L_2 Cos(\theta_1+\theta_2)\left(\dot{\theta}_1+\dot{\theta}_2\right) = L_3 Cos\theta_3\dot{\theta}_3 \tag{A.23}$$

From A.22 and A.23 we get $\dot{\theta}_3 = \omega_3$, which is the angular velocity of the wing joint. This will be required in the Dynamics Analysis, detailed in the next section.

$$\omega_3^2 = \dot{\theta}_3^2 = (L_1\dot{\theta}_1)^2 + \left(L_2(\dot{\theta}_1 + \dot{\theta}_2)\right)^2 + 2L_1L_2\dot{\theta}_1(\dot{\theta}_1 + \dot{\theta}_2)Cos\theta_2 \tag{A.24}$$

After angular velocities of joints 1, 2 and 3 are obtained, the joint K angular velocity can be obtained by using the equation A.19 (appendix).

A.1.4 Linear Acceleration of the Solenoid

When the slider is constrained to only one degree of freedom (linear motion in one axis), we obtain the so-called "ordinary slider-crank mechanism", which is commonly seen is reciprocating engines and compressors.

The Joint 1 $O_0\,(x_{o,}y_o)$, Limb 4 (L_4), Limb 5 (L_5) and Joint 5' $O'_5\left(x'_5, y'_5\right)$ define the crank-slider mechanism.

Angular acceleration of Joint 1 is given as $\ddot{\theta}_1$:

$$\ddot{\theta}_1 = \alpha_1 = \ddot{\theta}_3\frac{\dot{\theta}_1}{\dot{\theta}_3} + \dot{\theta}_3\dot{\theta}_k\frac{L_3}{L_1}\frac{Cos\theta_k}{Sin\theta_2} + \dot{\theta}_1\dot{\theta}_2\frac{Cos\theta_2}{Sin\theta_2} \tag{A.25}$$

Since the entire system is kinematically constrained, the above derivation of angular acceleration is obtained by differentiating Equation A.23 with respect to time. The book [33] explains the following derivation of the linear acceleration of the solenoid shaft in more detail. However some equations have been listed here for maintaining continuity.

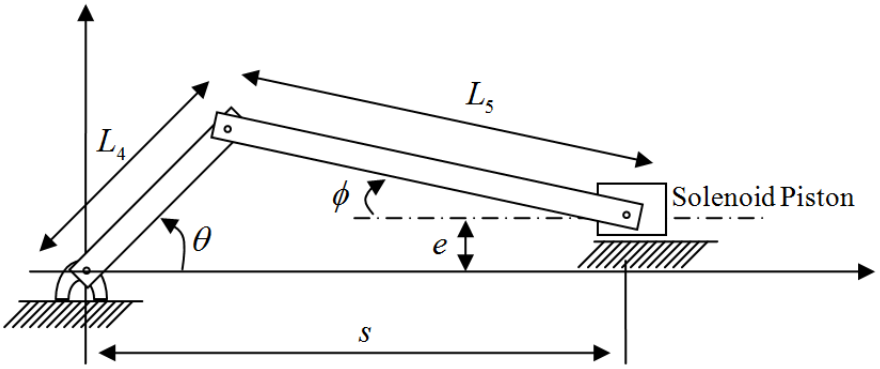

Figure A.1: Crank-Slider Mechanism Simplified

$$\dot{\theta} = -\dot{\theta}_1$$

$$\ddot{\theta} = -\ddot{\theta}_1$$

$$s = L_4 Cos\theta + L_5 Cos\phi$$

$$K_s = \frac{ds}{d\theta}$$

$$K_s' = \frac{dK_s}{d\theta}$$

where, the simplified version of the crank-slider mechanism adapted from the Figure 4.4 is shown in Figure A.1.

Finally we have:

$$\ddot{x} = -\left(K_s \times \ddot{\theta} + K_s' \times \left(\dot{\theta}\right)^2\right) \tag{A.26}$$

A.1.5 Solenoid Actuator Dynamics

$$F_{mag} = \frac{\partial W'(x,i)}{\partial x} \tag{A.27}$$

where W' = Energy stored in the coil in the form of magnetic flux

andg

$$W'(x,i) = \int_0^i \lambda(x,i).di \tag{A.28}$$

where, λ = flux linkage associated with the coil; which depends on the air gap distance (x) and current (i).

Also we note that current (i) and distance (x) are fully separable in relation to $\lambda(x,i)$, so we can differentiate the argument under the integral sign.

$$F_{mag} = \int_0^i \left.\frac{\partial\lambda(x,i)}{\partial x}\right|_{i=const} di \tag{A.29}$$

For instantaneous $F_{mag,}i$ does not change, so

$$F_{mag} = \frac{\partial\lambda(x,i)}{\partial x}\, i \tag{A.30}$$

Also,

$$NiA = \left(\frac{l\lambda}{\mu_0\mu_r} + \frac{x\lambda}{\mu_0}\right) \tag{A.31}$$

$$\lambda(x,i) = \frac{\mu_0 AN^2 i}{\frac{l}{\mu_r} + x} \tag{A.32}$$

which can also be represented as:

$$\lambda(x,i) = \left(\frac{k_a}{k_b + x} - offset\right) i \tag{A.33}$$

k_a and k_b are approximate constants,

whereas 'offset' is the flux leakage associate with the solenoid. All three constants are determined experimentally by plotting the flux vs current curves.

So F_{mag} can be written as

$$F_{mag} = \frac{\partial}{\partial x}\left(\frac{k_a}{(k_b + x)} - offset\right) i^2 \tag{A.34}$$

$$F_{mag} = i^2 \frac{k_a}{(k_b + x)^2} \tag{A.35}$$

A.2 AERODYNAMICS AND FLAPPING PERFORMANCE

MAVs operate in a very sensitive Reynolds number regime; wherein aerodynamic flow physics exhibits strong variance from conventional steady aerodynamic effects seen over the wings of fixed and rotary wing MAVs. Hence, designing vehicles that can efficiently fly in this regime represents an entirely new challenge to design engineers. Unlike subsonic fixed-wing aircrafts and their steady flow dynamics, biological flyers such as insects and small birds utilize vortex formation and harnessing to keep them aloft, especially in the case of hovering. It has also been demonstrated by Computational - Fluid - Dynamics (CFD) analysis that, bumble-bees flap their wings in a complex kinematic figure-eight pattern to generate lift and thrust [52]. Existing MAV designs cannot match the aerodynamic performance (stability, maneuverability, and efficiency) of insects and small birds due to the lack of design tools at this scale of flight.

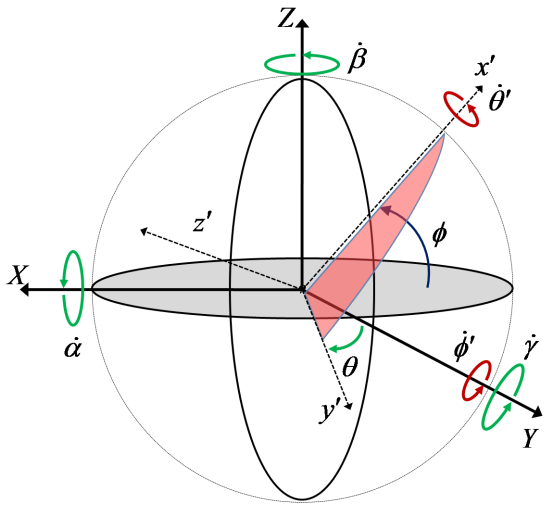

Figure A.2: Coordinate System for Wing Motion

Initially, effects of flapping frequency, amplitude and wing-feathering on 3D flow of motion parameters was studied and presented in detail in [35]. This involves the use of the unsteady solver and dynamic mesh capabilities of Fluidic Software Packages. The results are presented therein for a range of flapping amplitudes/frequencies and feathering amplitudes performing natural sinusoidal motions as produced by the active/passive actuation mechanism.

A.2.1 Coordinate Reference Frames

The 3D representation of the world/MAV-body frame of reference and the Wing Leading Edge frame of reference is as shown in Fig. A.2. $\dot{\alpha}$, $\dot{\beta}$ and $\dot{\gamma}$ represent the angular rates of the wing in the MAV/world frame of reference sent to the dynamic solver in *Fluent*. $\dot{\phi}'$ is the angular velocity of the flapping motion about the Y axis; $\dot{\theta}'$ is the angular velocity of the feathering motion. Table A.1 lists the nomenclature used in the analysis.

The coordinate transformation from the Wing-Leading-Edge frame of reference to the World frame of reference is given by the Eq. A.36. The angular velocity transformation is given by Eq. A.37 as required by Fluent.

Table A.1: Nomenclature

Symbol	Description
ϕ	Instantaneous flapping angle
θ	Instantaneous Feathering Angle
A_{flap}	Amplitude of Flapping Motion
A_{feat}	Amplitude of Feathering Motion
C_L	Lift Coefficient
C_D	Drag Coefficient
t	Time

$$\begin{bmatrix} X \\ Y \\ Z \end{bmatrix} = \begin{bmatrix} cos(\phi) & sin(\theta)sin(\phi) & cos(\theta)sin(\phi) \\ 0 & cos(\theta) & sin(\theta) \\ sin(\phi) & sin(\theta)cos(\phi) & cos(\theta)cos(\phi) \end{bmatrix} \begin{bmatrix} x' \\ y' \\ z' \end{bmatrix} \tag{A.36}$$

$$\begin{bmatrix} \dot{\alpha} \\ \dot{\beta} \\ \dot{\gamma} \end{bmatrix} = \begin{bmatrix} cos(\phi) & 0 & 0 \\ 0 & sin(\phi) & 0 \\ 0 & 0 & 1 \end{bmatrix} \begin{bmatrix} \dot{\theta}' \\ \dot{\theta}' \\ \dot{\phi}' \end{bmatrix} \tag{A.37}$$

A.2.2 Wing Kinematics: Velocity Analysis

The wings of insects and birds often move in somewhat complex patterns. However, for modeling purposes the motion is usually simplified into four steps: downstroke, upstroke, supination, and pronation. Supination and pronation occur at the end of each flapping stroke and serve to change the angle of incidence of the wing about its leading edge. In Fluent, the wing kinematics must be defined in terms of rotational velocities as functions of time. The actuators used for the QV, flap the wings with a simple sinusoidal velocity profile as given by Eq. A.38.

$$\dot{\phi} = -A_{flap}\omega\cos(\omega t) \tag{A.38}$$

The feathering motion is more complicated. Our actual bench-top actuator uses a spring

and hard stops to feather the wing. This produces a feathering motion which starts and stops impulsively during the ends of the upstroke and downstroke. Trials in Fluent with sudden jumps in feathering velocity resulted in sudden jumps in the force traces as well, so it was necessary to approximate the feathering motion (as in Eq. A.39) using a continuous function (Described in [35]).

$$\dot{\theta} = A_{feat}\,\omega \sin(\omega t) \tag{A.39}$$

The above equation represents only the motion during the upstroke; during downstroke the feathering angle is always zero.

.

A.2.3 Grid & Boundaries

The unsteady flapping+feathering motion of the cambered elliptical wing was simulated in Ansys Fluent V12.1[1]. Fig. A.3 shows the unstructured tetrahedral grid generated using *Gambit*[2]. The overall grid was divided into 2 parts: an inner smaller spherical domain bounding the wing motion with a fine mesh to ensure good resolution of the flow around the wing, and an outer spherical domain with a coarser mesh. Fig. A.4 displays the grid deformation freeze frames for one complete flapping cycle.

A.2.4 Spanwise Vortex Formation

Fig. A.5 represents the formation of leading edge vortex which plays an important role in production of lift for unsteady flapping wings at low Reynolds Number. More detail has been given in [35].

[1] A commercially available CFD software package. The CFD results were obtained by Taher Basrai and Daniel Prosser

[2] a commercially-available software for grid generation

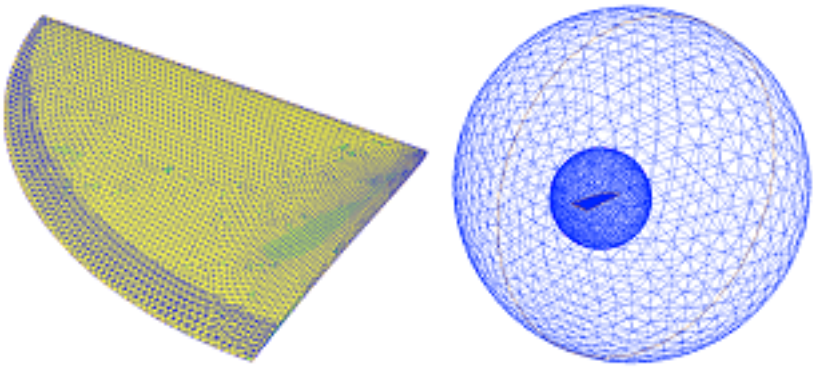

Figure A.3: Wing Mesh (Left); Mesh Grain/Boundary (Right)

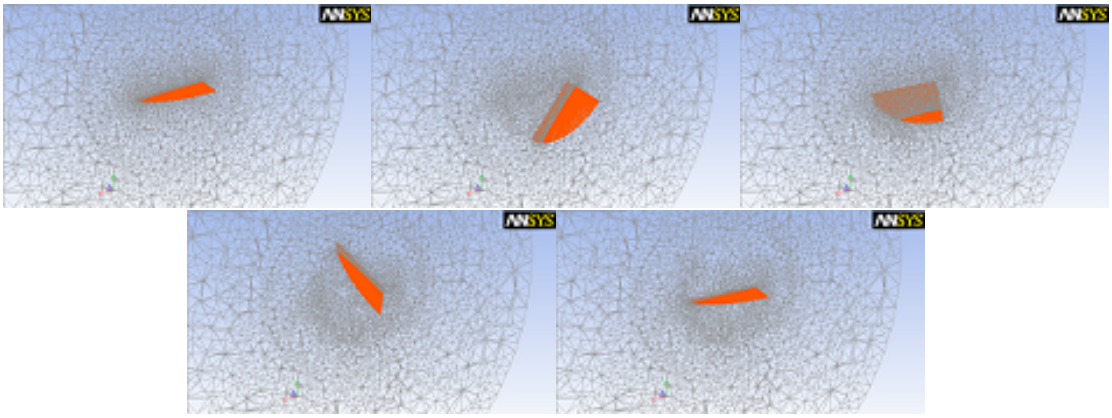

Figure A.4: Grid Deformation: One Flapping Cycle (from Top left to Bottom right)

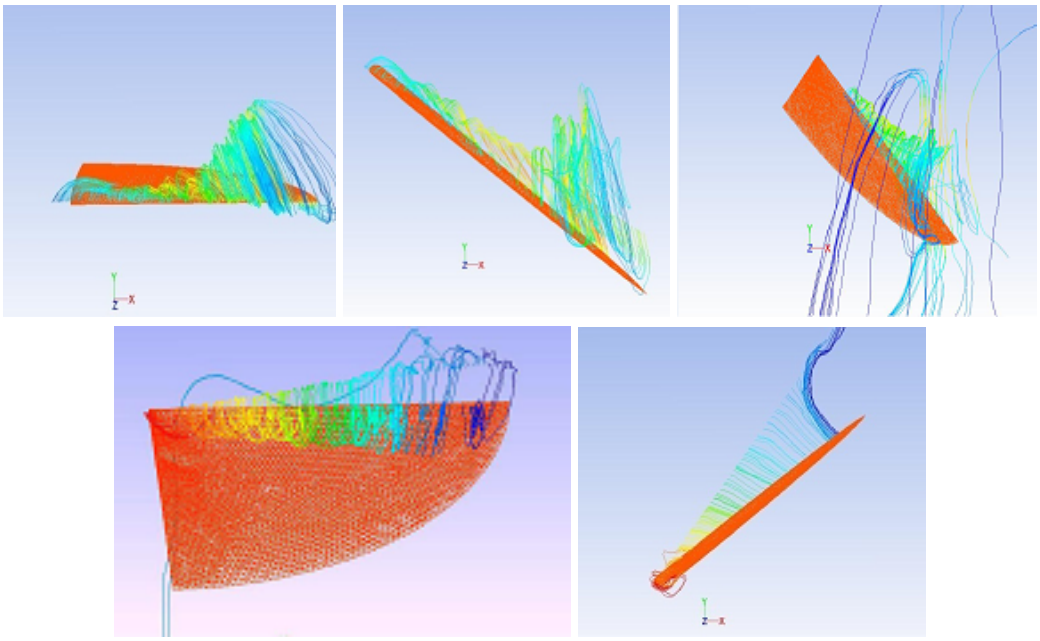

Figure A.5: Leading Edge Vortex Dynamics on Wing Surface (From Top-Left): at 0s; T/8 s; T/4 s; T/2 s; 7T/8 s

A.2.5 Amplitude Sweeps

A 3D quarter- elliptical wing with base chord 3.5" and span of 5.5" is used. Further, in order to augment positive lift generation, a small camber was given to the wing. Sweeps of flapping and feathering amplitudes were performed at a flapping frequency of 20 Hz in order to converge on a set of motion parameters to improve the performance of the flapping wing vehicle. Feathering amplitudes of 0, 15, 30, 45, 60, and 90 degrees were each run for flapping amplitudes of 30, 40, 50, and 60 degrees, for 24 total cases. The Reynold's number and the reduced frequency range for these cases was from 2500-6000 and 0.3-0.8 respectively. Taking advantage of the periodic trend of forces over each flapping cycle, each case was run for two full flapping cycles to remove the effects of startup transients and poor solver convergence during the first several time steps. For each case, the average lift and drag coefficients and forces were recorded for the second full flapping cycle. The direction of lift and drag is usually referenced to the direction of the upstream velocity, but for hovering, where the upstream velocity is 0, lift and drag are defined relative to the body of the MAV. Thus, lift is in the positive z-direction and drag is in the positive x-direction.

The most striking feature of Fig. A.6 is that average lift force increases with increasing feathering amplitude. This highlights the importance of feathering motion in producing lift. Note that in the case of no feathering, the average lift force is roughly zero for all flapping amplitudes. However, the increase in lift force becomes less pronounced for very high feathering amplitudes; the average lift force for 90 degrees feathering is not much greater than that for 60 degrees. For cases with a positive feathering amplitude, lift force increases linearly as flapping amplitude increases, and the effect generally becomes more pronounced as feathering amplitude increases.

Fig. A.7 shows the drag force[3] for the amplitude sweeps. An MAV in a dragonfly-like configuration can maintain equilibrium in hovering mode even if each wing is producing a

[3]Note, negative drag is equivalent to thrust, which is conventionally important for forward flight, but in hovering mode it is desirable to minimize any horizontal force.

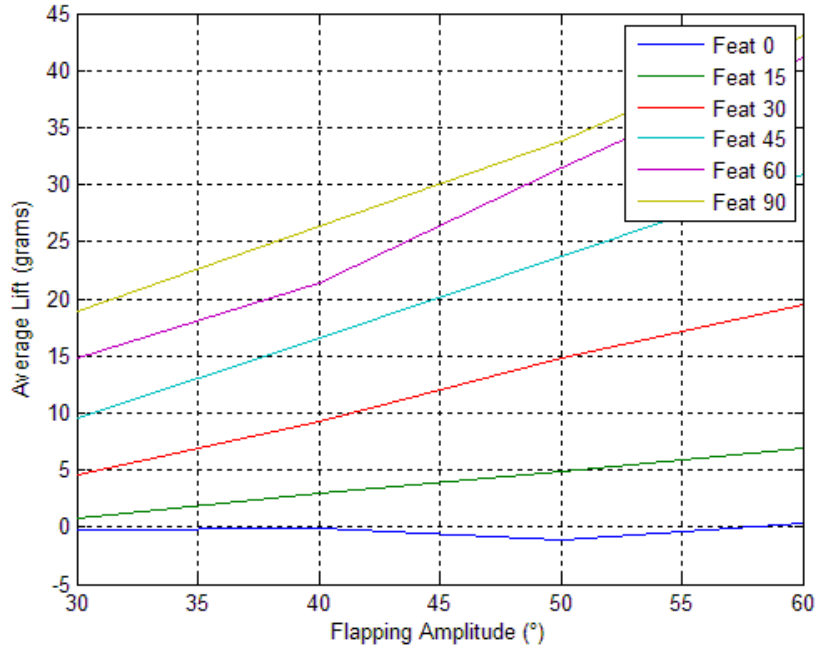

Figure A.6: Lift Force (grams)

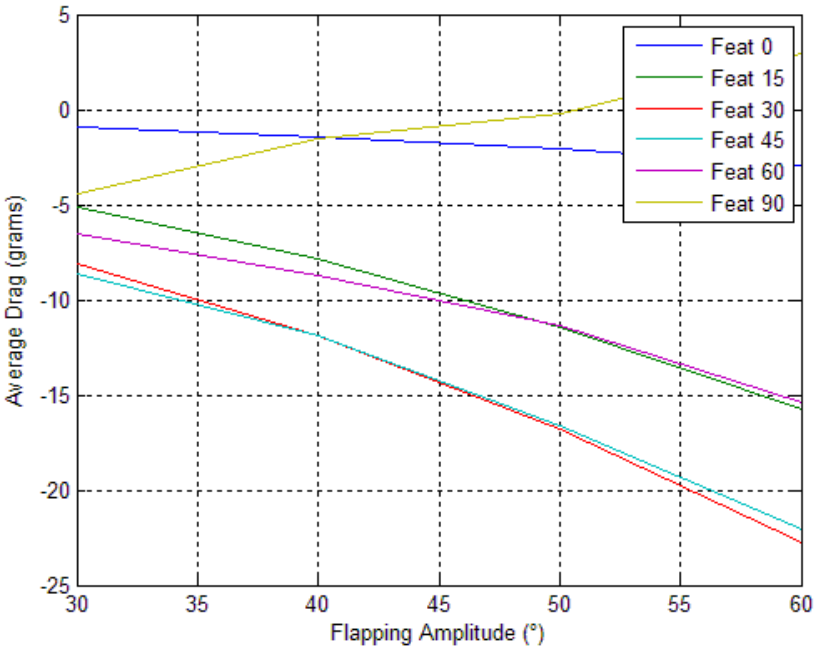

Figure A.7: Drag Force (grams)

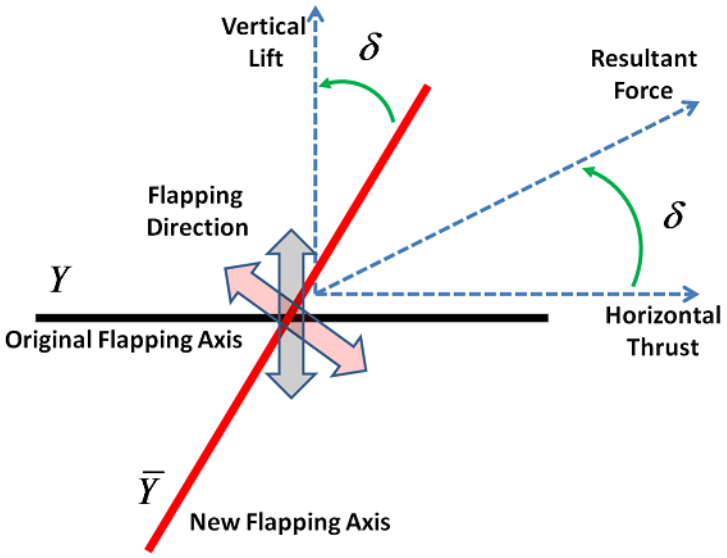

Figure A.8: Wing Flapping Axis Chage: Net Force Re-direction

horizontal force, as long the net horizontal force of all wings together is zero. The solution is to re-orient the wings at an angle so they flap about a new axis between the Y and the Z axis, determined by the vector addition of the thrust and lift force components. By directing the net resultant force, along the negative Z axis, each wing can be made to produce *Only* an upward force. This can be seen in the design of the QV-MAV in Fig. 4.24. The 6DoF control can now be achieved with the control law illustrated in Fig. 4.12.

Fig. A.8 shows how the lift and thrust components produced by the wing are directed perpendicular to each other. The net resultant force is directed at an angle δ. This requires that the wings' flapping pivot be re-oriented to the new position such that the resultant force is directed vertically upwards.

A.2.6 Frequency Sweeps

The results for different flapping frequencies were checked at an $Amplitude_{Flapping}$= 50^o and $Amplitude_{Feathering}$= 60^o. Fig. A.9 shows the average force over a flapping cycle at different frequencies. A steep increase is seen in the average lift force and drop in the average drag force (thrust) with increase in flapping frequency as expected. As explained above, re-orienting the wings to flap in a different plane can channel the forces more effectively. A

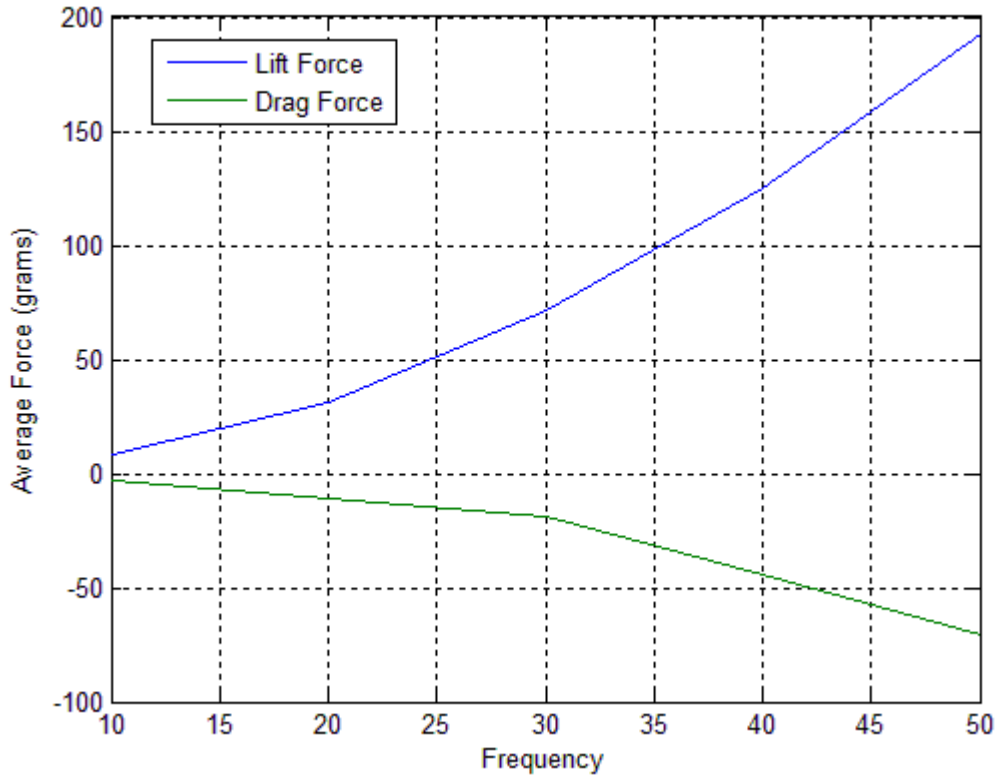

Figure A.9: Lift and Drag Forces Vs Frequency

more interesting trend is seen in Fig. A.9 which shows the average lift and drag coefficient over one flapping cycle. More detailed analysis is presented in [35].

A.3 FEATHERING HARDWARE AND PROTOTYPING

A.3.1 Load Cell and Wind Tunnel Rig Designs

Fig. A.10 is a scale model of the wing actuation mechanism, connected to a 6-axis load cell.

A.3.2 Feathering Mechanism

Khan and Aggarwal [23] explored the idea of using a spring-loaded cam-follower system, driven by a four-bar mechanism to control the feathering of the wings during flapping. However, this mechanism is only possible for systems with fixed amplitude flapping, this

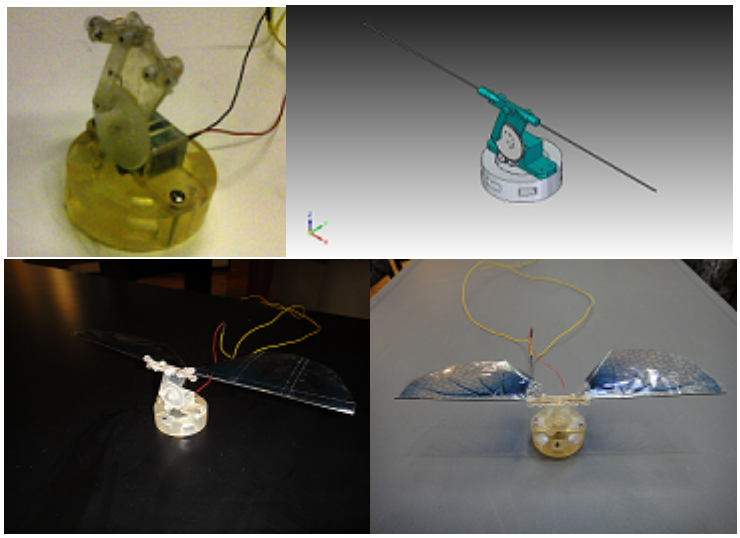

Figure A.10: Flapping Mechanism

doesn't work for insect, bird like systems with variable amplitude flapping. Raney and Solominski [36] produced active feathering of hummingbird scale wings, however addition of an extra actuator proves bulky and difficult to install. The feathering mechanisms we have implemented constitute passive feathering of the wings to conform to fixed frequency, variable amplitude flapping as exhibited by birds and insects.

A.3.3 Passive-Feathering - Designs

Some of the modular passive feathering wing designs tested on the flapping setup shown in Fig. A.10 are presented in Fig. A.11[4].

A.3.4 Spring Restoration Mechanism

Fig. A.12, is a close-up of the feathering mechanism which details the installation of the passive spring. The wing-spar (leading-edge) is connected to the larger spool and is capable of free rotations (limited by hard-stops), the feathering is passive, thus the feathering angle is dictated by the spring constant and the air-damping on the wing. The addition of the spring ensures that abrupt impact stops are not presented on the wing when it reaches its maximum feathering limits.

[4]The CAD was done by Jason Dickert

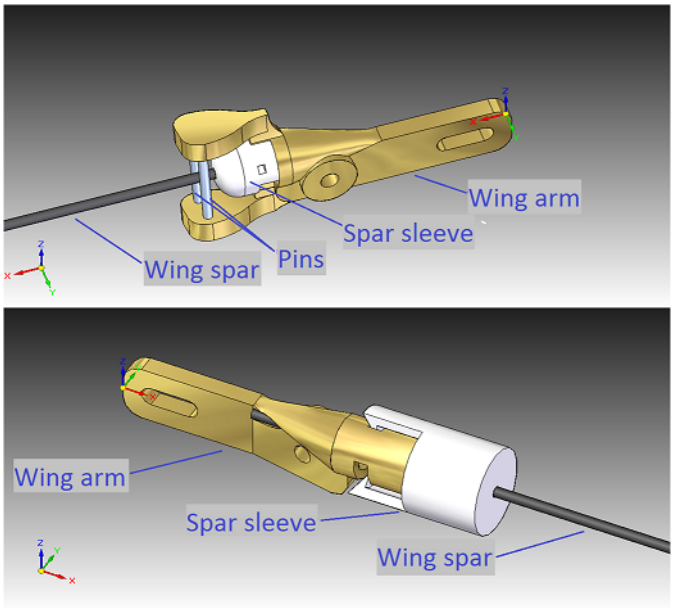

Figure A.11: Passive-Feathering Designs

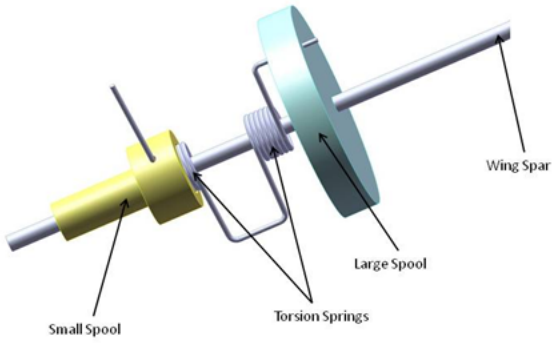

Figure A.12: Spring Joint for Passive-Feathering

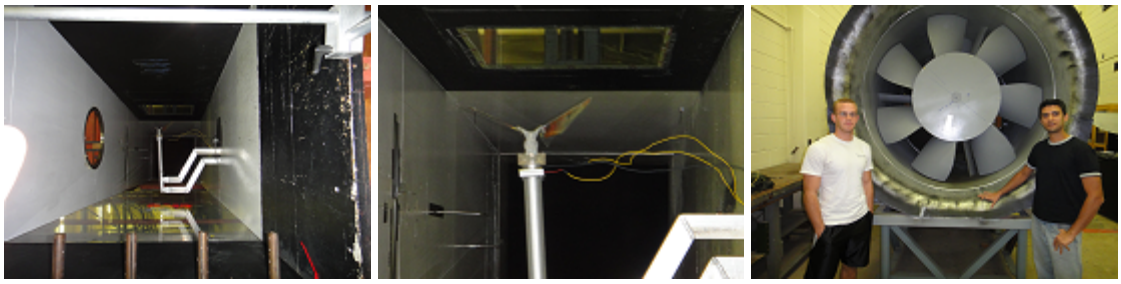

Figure A.13: Wind-Tunnel-Setups (From Left): GT Wind-Tunnel; MAV Mount Close-up; GT Wind Tunnel Turbine

A.3.5 Wind-Tunnel Facility

The aerodynamic forces experienced by the load cells at different flapping modes of the MAV will be experimented and matched against the simulation results obtained. The comparison would provide a means to iterate and improve upon wing designs, simulation models, flapping/feathering mechanisms and subsequently miniaturize the wing size to meet MAV size specifications.

A.4 EMBEDDED DESIGN

The conventional Mini and Large scale UAV systems span anywhere from approximately 12 inches to 12 feet; endowing them with larger propulsion systems, batteries/fuel-tanks, which in turn provide ample footprint and power reserves for on-board avionics and wireless telemetry. The limitations thus imposed become apparent when shifting to Micro Aerial Vehicles (MAVs) and trying to equip them with equal or near-equal processing, sensing and communication capabilities, as their larger scale cousins. The conventional MAV as outlined by DARPA is a vehicle that can have a maximum dimension of 6 inches and weighs no more than 100 grams. Under these tight constraints, the footprint, weight and power reserves available to on-board avionics is drastically reduced. The paper presents the advent of a new line of Micro Architecture and Control (MARC) avionics systems with very low-power, multi-sensor, multi-processor avionics interconnect architecture designed specifically with the power and payload constraints of MAVs in mind.

A.4.1 Related Work

There has been a significant amount of work done till date in autopilot and Flight Control System (FCS) hardware but none has been focused on embedding full scale (larger UAV) comparative avionics on "true" micro scale, with the added goal of Micro Power Consumption as well. The systems have been made to be compact and modular to conform to small/mid/large sized UAVs which are quite forgiving to the avionics with respect to both their power consumption and weight. When we scale to micro sizes (Table 1.1) both weight and power consumption of the avionics becomes significant in comparison to the actuators, becoming detrimental to the performance of the MAV. A number of issues in the present state of the art need to be addressed.

A number of avionics architectures and flight control boards in Research and COTS today use multi-voltage standards, i.e., the components, peripherals and on-board processors, sensors, transceivers operate at varying voltage levels [5, 8, 11, 16, 18, 30, 38, 44]; this is quite acceptable in UAVs of small/mid/large scales, where payload is not a severe constraint, but for MAVs this is highly impractical. The use of multi-volt peripherals on-board requires the installation of multiple power sources or voltage-regulators/level-shifters on-board the MAV. The added weight and efficiency losses of voltage-regulators / Buck-Boost Converters / level-shifters is quite avoidable by selecting low voltage sensors and keeping the voltage level uniform across peripherals.

Much of the work also discusses using a low-bandwidth RS-232 interface (115Kbps) to communicate with a host PC [38, 44] or transmit sensor data to the processor using the same [16, 21]. Also, higher resolution sensors imply larger data packets, limiting sampling rates; for MAVs with fast/unstable dynamics sensor update/sampling time should be very small.

A number of related works also talk about use of I2C or CAN protocols of interfaced sensors like magnetometers, accelerometers, gyroscopes etc [30, 44]. I2C has a maximum

baud rate of 400 to 800 Kbps and CAN bus, 1Mbps baud rate (as compared to an SPI interface of 24Mbps) which also act as bottlenecks for higher sensor sampling rates, required on unstable/dynamic MAVs.

Modularity is very crucial for experimental platforms but comes at the price of higher hardware weight and size. The severe restrictions on flight payload and flight time / flight energy reserves on-board a MAV warrant smaller form factors. Thus a stacking of modules approach [8, 11, 18, 21, 30], needs to be replaced by a single board - custom avionics solution. The modularity can be maintained to some extent by introducing an FPGA based solution to replace the flight computer and peripheral - interfacing controller and glue together different communication / interfacing protocols.

The use of a microcontroller (as against an FPGA) as the primary flight computer and integrator [11, 16, 20, 21, 30, 38, 44] compromises flexibility, speed and modularity. For upgrading/expanding memory interfaces/sensors/processors the avionics board will require re-designing or a new COTS board will have to be selected. Most of the microcontrollers also used were 16-bit architecture (as against a 32 bit design), hence the maximum addressable memory size (without a virtual memory) is 64KB, presenting a major restriction for long range data-logging or video recording or any kind of memory intensive application. Having a low operating clock frequency for the on-board processors [20, 38, 44] is also a detrimental factor to micro sized passively-unstable flyers, requiring high processing and sensor data acquisition.

The size and weight of the state of the art flight control boards with excellent processing capabilities and sensing suites is non-transferable to MAVs. The present state of the art avionics with the lightest configuration weigh above 65 grams and/or consume at least 6~7.5 Watts of on-board power [5, 16, 21]. Grzonka et al. [16] show case their Small UAV with a 300 grams avionics payload at 7.5 Watt power consumption. Christophersen et al. [5] demonstrate the flight control board with a weight of 65 grams. Kendoul et al. [21]

present their board with a gross weight of 65 grams. All of these exceed the maximum payload capacity for an MAV by manyfolds.

Thus an FCS board within a ceiling of 15 grams and power consumption of less than 0.5 Watts is the primary requirement for MAVs. We present here the MARC avionics system that weighs 15 grams, consumes 0.6 Watts of on-board power and possesses nearly equal or higher performance functionality shown on FCS boards weighing 50~100 grams or more. The full performance of the hybrid DSP/FPGA MARC system is approximated at 1 Billion Floating Point operations per second (or 1 GFLOPS[5]).

A.4.2 Micro Architecture and Control (MARC) Avionics Platform

The autopilot/avionics-suite designed and tested comprises a low-power FPGA and multiple communication peripheral protocols for interfacing with 3-axis gyroscopes, 3-axis accelerometers, a high resolution digital image sensor, a serial flash memory among others. An external DDR memory device and a DMA device has been added for storing image data captured by the camera sensor and transmitting it through a low-power 2Mbps wireless RF transceiver. The FPGA also hosts a DDR memory controller, volatile/non-volatile internal memories, and various communication buses and custom digital glue logic required for interfacing with the external components. The DSP provides high performance signal processing and video processing capabilities along with high level control over the various low-level control loops. It is connected to the FPGA and to the DMA via the External Memory Interface (EMIF). The MARC construction and soft-computing capabilities are overviewed in the following sub-sections.

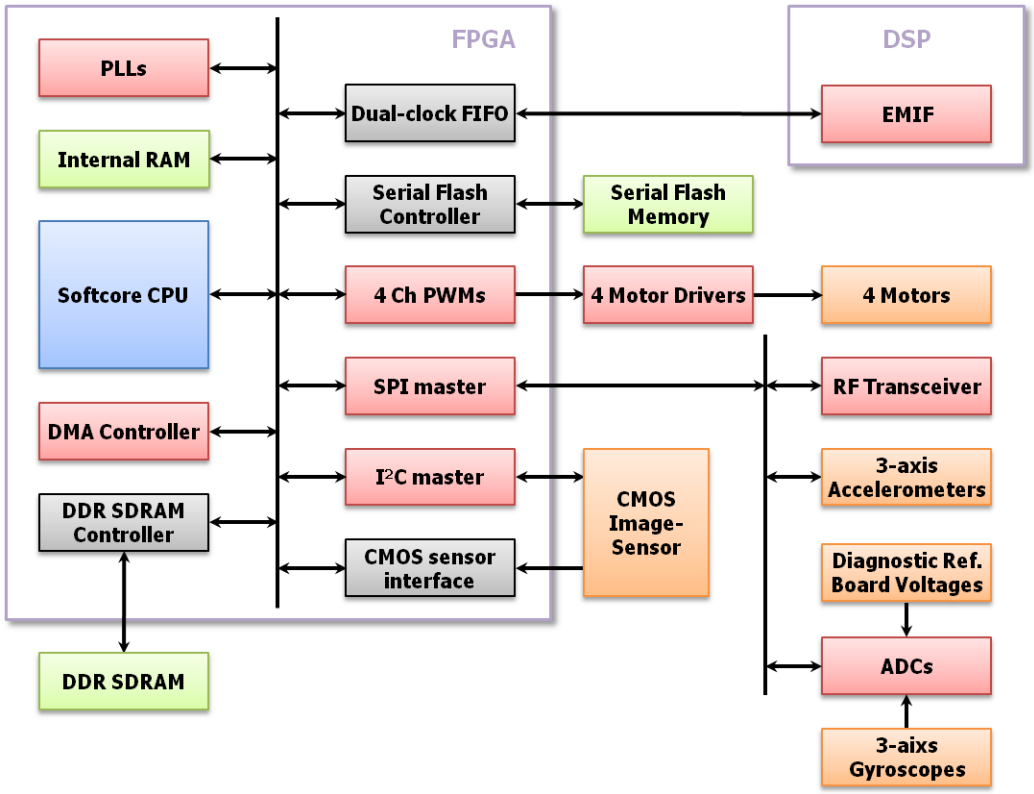

Figure A.14: Embedded Hardware Architecture

A.4.2.1 Avionics Design

Fig. A.14 shows the outline of the embedded hardware on-board the MAV. The selection of the processors for this embedded device involved many important considerations such as power consumption, size/weight and performance. The system is a twin-processor design with an inter-connected FPGA and DSP. The FPGA acts as the integrator and is used to implement various tasks like glue logic, control logic, custom IP and hardware-accelerators for computationally intensive algorithms. The FPGA also carries out low-level repetitive functions thus helping to improve the system performance considerably by freeing up the DSP from cycle-intensive tasks. The DSP carries out high-level flight controls, navigation and image/video processing. The FPGA and DSP combination in the design provides

[5]The computing speed differs for different instructions. It depends on the number of hardware multipliers and the ability of the code to be pipelined/multiplexed in hardware. The performance will improve with hardware acceleration applied to the soft core processor. 1 GFLOPS was recorded by running a predetermined cycle time code for 1000 times.

excellent performance characteristics and much flexibility to accommodate changing standards and component upgrades.

The FPGA, hosts a 32-bit softcore NiosII CPU, a DMA controller, a DDR RAM controller, an internal RAM, four digital PLLs, and all communication interfaces required for connecting external peripherals to the softcore CPU.

A.4.2.2 Sensor Interfaces

The SPI bus interface is a serial 3-wire communication protocol. Assigning a Chip Enable (CE) signal for each slave device, an SPI bus master can communicate with multiple SPI slave devices. The SPI bus is much faster (24Mbps) than the I2C(800Kbps) and CAN(1Mbps), thus the reasoning to use the SPI bus for high baud-rate serial communications for data acquisition/transmission and sensor sampling. The FPGA has two SPI master modules, connecting to the transceiver and for communication with peripheral sensors. Two 2-axis MEMS gyroscopes and host of different voltage and temperature references across the board are fed through an SPI interfaced 2Msps 16 Bit A/D converter. The voltage and temperature references throughout the board provide real-time diagnostic and prognostic information to the Flight Controller. The 3-axis accelerometer connects directly to the SPI Master as shown in Fig. A.14. Additional sensors are being added onto the MARC-3 Unit, which include a GPS, a 3-axis magnetometer/compass, pressure sensors and a stereoscopic camera system.

A.4.2.3 Embedded Vision and Wireless Telemetry

The ground station tele-operates the MAV and/or uploads waypoints for semi-autonomous flight navigation. The MARC collects internal state information, environmental data including aerial video/images during flight and transmits this data via a block data packet to the ground station also through the RF Transceiver; Fig. A.15 briefly illustrates the link.

The MAV and ground station are linked via a half-duplex, 2.4 GHz ISM band RF transceiver,

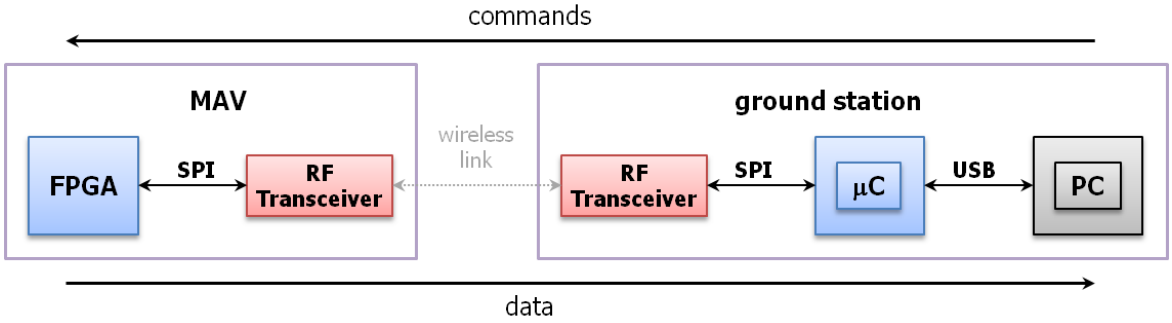

Figure A.15: Wireless link between the MAV and the ground station

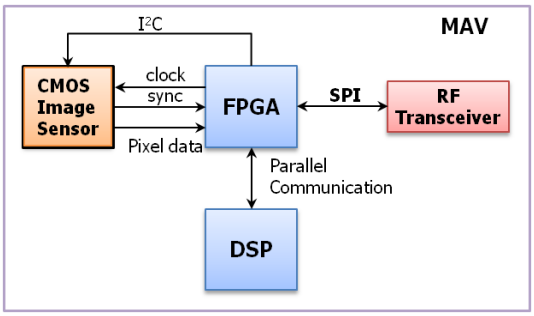

Figure A.16: Video/Image Capture and Transmission

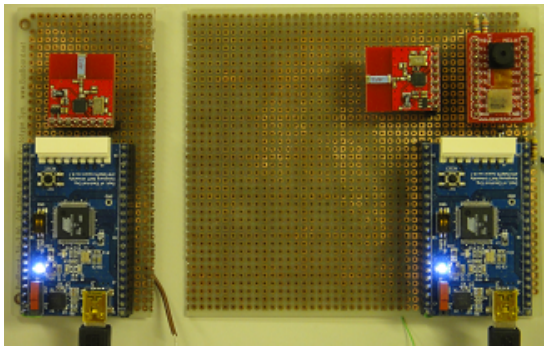

Figure A.17: Wireless Transceiver, CMOS Camera Interface

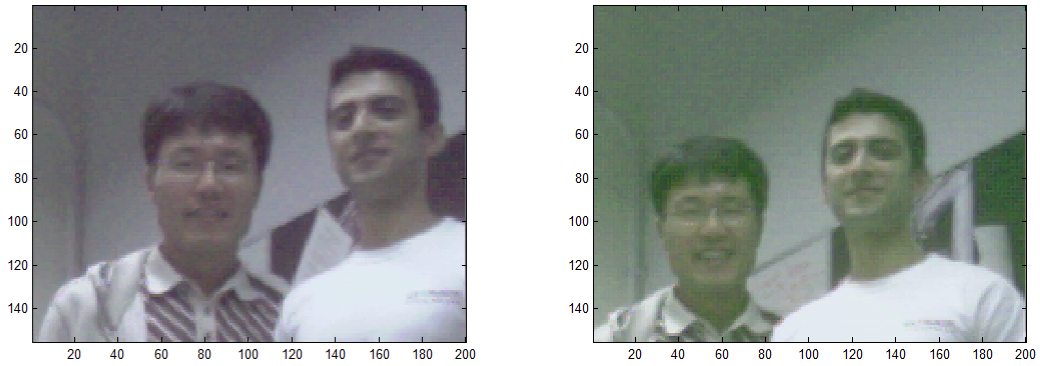

Figure A.18: Wireless CMOS Sensor images

which supports an air data rate of up to 2 Mbps. The RF transceiver is in standby or power down mode while not communicating, reducing power consumption. The prototype hardware is shown in Fig. A.17 and the wireless video results are shown in Fig. A.18.

Real-Time Imaging is imperative for remote Intelligence, Surveillance and Reconnaissance (ISR) purposes, and as such the MARC-2 is equipped with a VGA micro CMOS image sensor for capturing aerial - images; an upgrade to dual (stereoscopic) 5 Megapixel CMOS cameras is underway for the MARC-3. Fig. A.16 demonstrates the interface for image capture and wireless-transmission. The CMOS image sensor is connected to the FPGA hosting the soft-core processor, memory, and additional miscellaneous glue/accelerating logic. The image sensor supports video or snapshot operation at a capture rate of 30 fps. The major role of the DMA controller is bulk data transfers, reading from the CMOS image sensor to the DDR RAM, without the intervention of the CPU. The DMA controllers of the FPGA and DSP also perform bulk/single packet transfers between the internal/external memories of the two devices.

The FPGA includes an internal Dual-Access RAM of size of 600 KB. The internal data RAM, however, is not enough for storing image/video data captured by the CMOS sensor. Though SRAMs are usually easy to use and do not need a special controller, they are not ideal options for the avionics suite, owing to their larger form factors than DRAMs. A

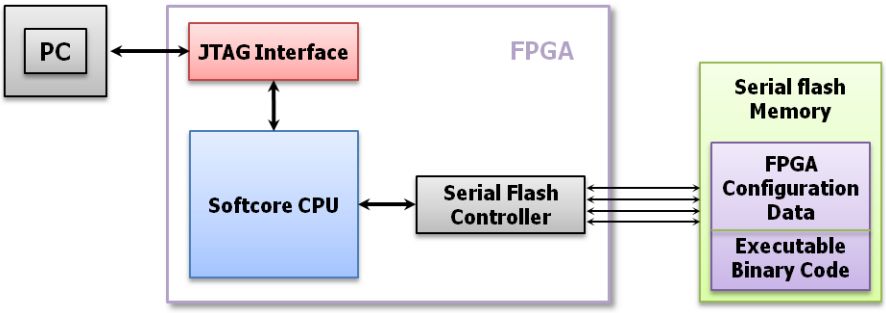

Figure A.19: Serial Programming Interface for the FPGA

DDR SDRAM controller (166Mhz R/W speed) is implemented on the FPGA itself. The FPGA hosts one I2C master and can communicate with multiple I2C slave devices. Since the maximum clock rate of the I2C bus is only 400 kbps, the I2C protocol is usually only used to configure slave devices and not for data transfer operations. On the MARC, the CMOS image sensor is initialized and configured through the I2C bus.

A.4.3 Serial Programming

The configuration data for the FPGA needs to be stored in an external non-volatile memory for power-up/start-up configuration to be possible. The executable binary code for the softcore CPU is also stored in an external non-volatile memory. The FPGA includes a serial flash controller and the MARC is equipped with a single serial flash memory of 128MB (not for real-time data logging).

A.4.4 FPGA - DSP Interface

The FPGA and DSP exchange image/video data, sensor data and MAV states, in addition to commands relayed by the ground station. They communicate via dual-clock FIFOs on the FPGA side and the External Memory InterFace (EMIF) on the DSP side. One of the two dual-clock FIFOs is for reading from the DSP and the other for writing to the DSP. The DSP recognizes the two FIFOs as a single external memory-mapped device of the same address. When the DSP writes to the address, the content is written to the read FIFO. When the DSP reads from the address, it reads the content of the write FIFO. On the other

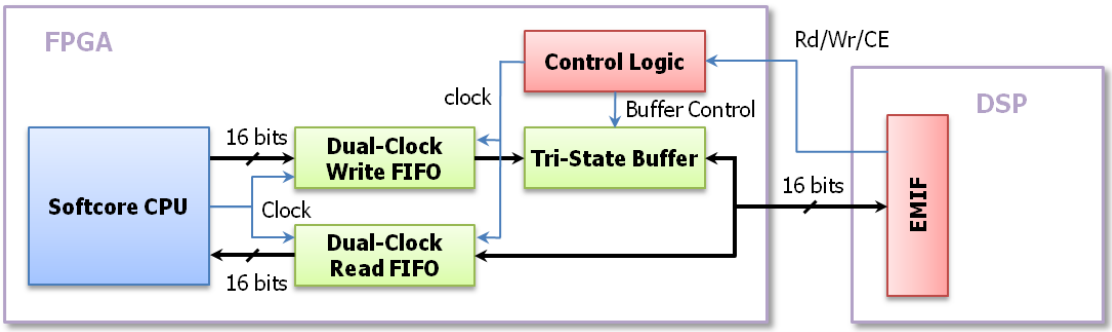

Figure A.20: FPGA - DSP EMIF interface

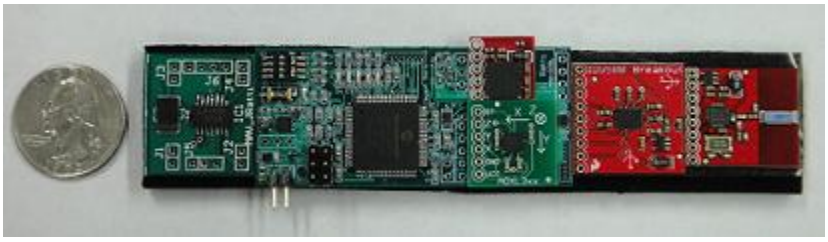

Figure A.21: MARC-1 (dsPIC33F) Single Core

hand, the two FIFOs are individually connected to the softcore CPU (on-board the FPGA) and therefore they have different addresses. The FPGA also includes control logic required for a tri-state buffer control and generating a clock signal to the FIFOs. The interface block diagram is shown in Fig. A.20.

A.4.5 Actuation Control

The FPGA has four 32-bit PWM generators for controlling the speed of four motors/actuators. The carrier frequency and duty cycle of the PWM outputs can be individually controlled by writing appropriate values in associated registers. Four dedicated Servo outputs have been connected to the Motor Driver chips on-board the MARC-2 for the QV design [41].

Figure A.22: MARC-2 (Cyclone III, TI 55xx DSP) Dual Core

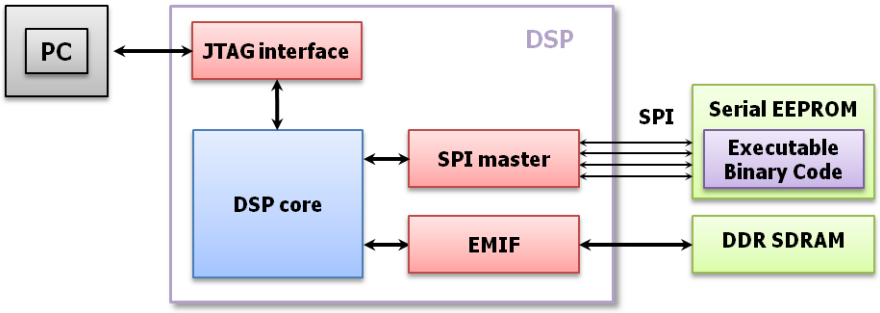

Figure A.23: DSP Interconnect

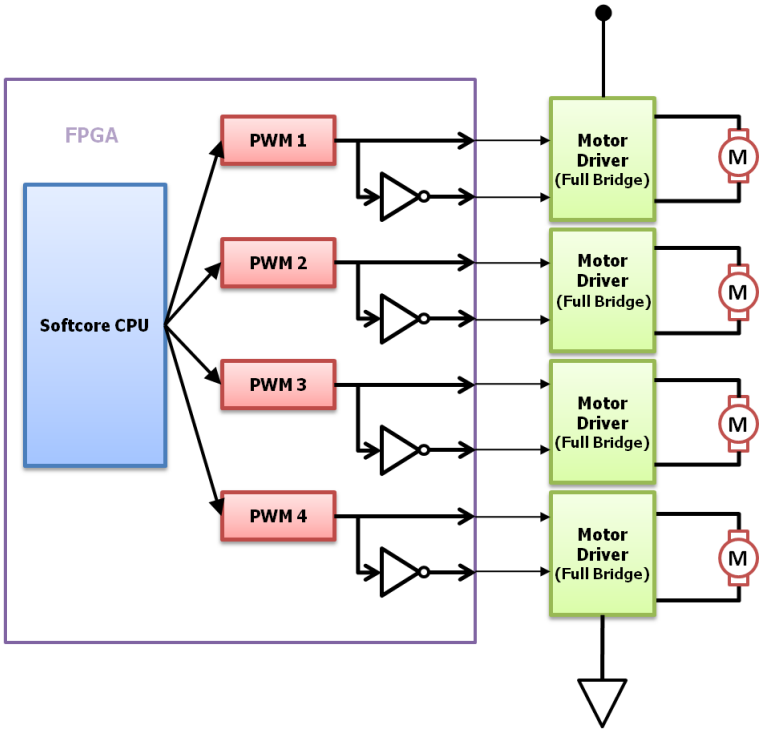

Figure A.24: QV Actuation Control using MARC-1,2

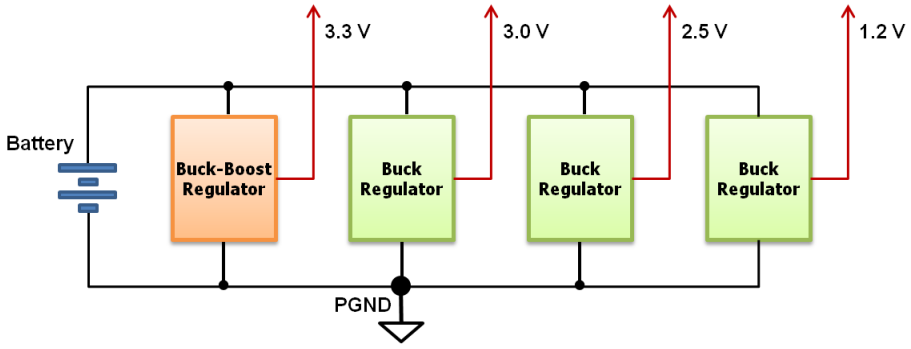

Figure A.25: On-board Power Supply and Distribution

A.4.6 Power Supply and Distribution

All the on-board sensors, wireless transceivers, cameras, processors and memory modules operate at a uniform 3V power supply. However, the FPGA requires three different power levels; 1.2v for its processor core operation, 2.5V for its PLL operation and 3.0 volts for interfacing with the 3 Volt peripherals. The power supply grid is shown in the Fig. A.25. Also larger difference between output voltages and input voltages result in larger losses in LDO and Switching Regulators, hence we devised the step wise voltage reduction. The transition from Battery Voltage to 3.3 Volts is carried out by the Buck-Boost converter to remedy the falling voltage of the Lithium Polymer Battery Pack. The three subsequent Buck Converters step down the voltage from 3.3 Volts to 3.0 Volts, from 3.0 Volts to 2.5 Volts and 2.5 Volts to 1.2 Volts respectively. The three Buck Converters are housed in a single chip to save footprint on the MARC board. The only disadvantages to using Buck/Boost converters is the interfacing with external inductors. The inductors are bulky, lossy and produce EMI interference, thus should be shielded (or avoided) as much as possible.

A.4.7 Results: Power Drain and Weight

The goal of the MARC-2 board was to keep all the avionics within a total weight of 15 grams and the on-board avionics power requirement within 0.75 Watts. Towards that end the different processors and peripherals were selected as shown in Table A.3. The total weight of the MARC-2 Avionics Suite was 15.75 grams and the total power consumption

Table A.2: Power and Weight Configuration of the MARC-1

Component	Weight (Grams)	Power (mW)
dsPIC33F	0.55	300
2-Axis Gyro Breakout	2	21
1-Axis Gyro Breakout	0.55	15.84
Transceiver Breakout	1.7	Tx: 33.9; Rx: 36.9
Motor Driver Breakout	2.35	90
Bare-PCB	6.35	3 (Losses-Approx)
Power Regulators, Switches, LEDs	2	40 (Losses-Approx)
Passives, Wiring	5	10 (Losses-Approx)
Total	20.5	550 (0.55W)
Total (w/o Motor Drivers)	18.15	460 (0.46W)

was approximately 0.833 Watts (Including the Motor Driver supply; which is not part of the avionics suite). Total power consumption without the motor drivers was 0.65 Watts.

Although unrelated, but if the designer is unable to obtain low weight and power avionics then the QV MAV design has the potential to accommodate even higher payloads and power intensive avionics owing to its inherent high efficiency actuation configuration [37, 41]. The MARC-1 board was designed with breakout modules for flexibility and modularity; the weight was thus higher (TableA.2). More detail has been presented under [40].

A.4.8 Real Time Operating System Architecture

The RTOS proposed is the Micro C OS-II Real Time Operating System. The architecture of the Hardware in the Loop (HILS) setup utilizing the RTOS [19] has been shown in Fig. A.26. The architecture illustrates the use of Semaphores, Flags and Mailboxes to communicate and coordinate the parallel operation of all the tasks and sub-tasks on-board the MAV. The architecture has been designed to keep the code flexible enough to allow adding higher level tasks to mission directives sent by the ground station. All this can be achieved without engrossing into the system level intricacies of handling and programming a microcontroller/microprocessor. The flexibility of the architecture also makes it extremely effi-

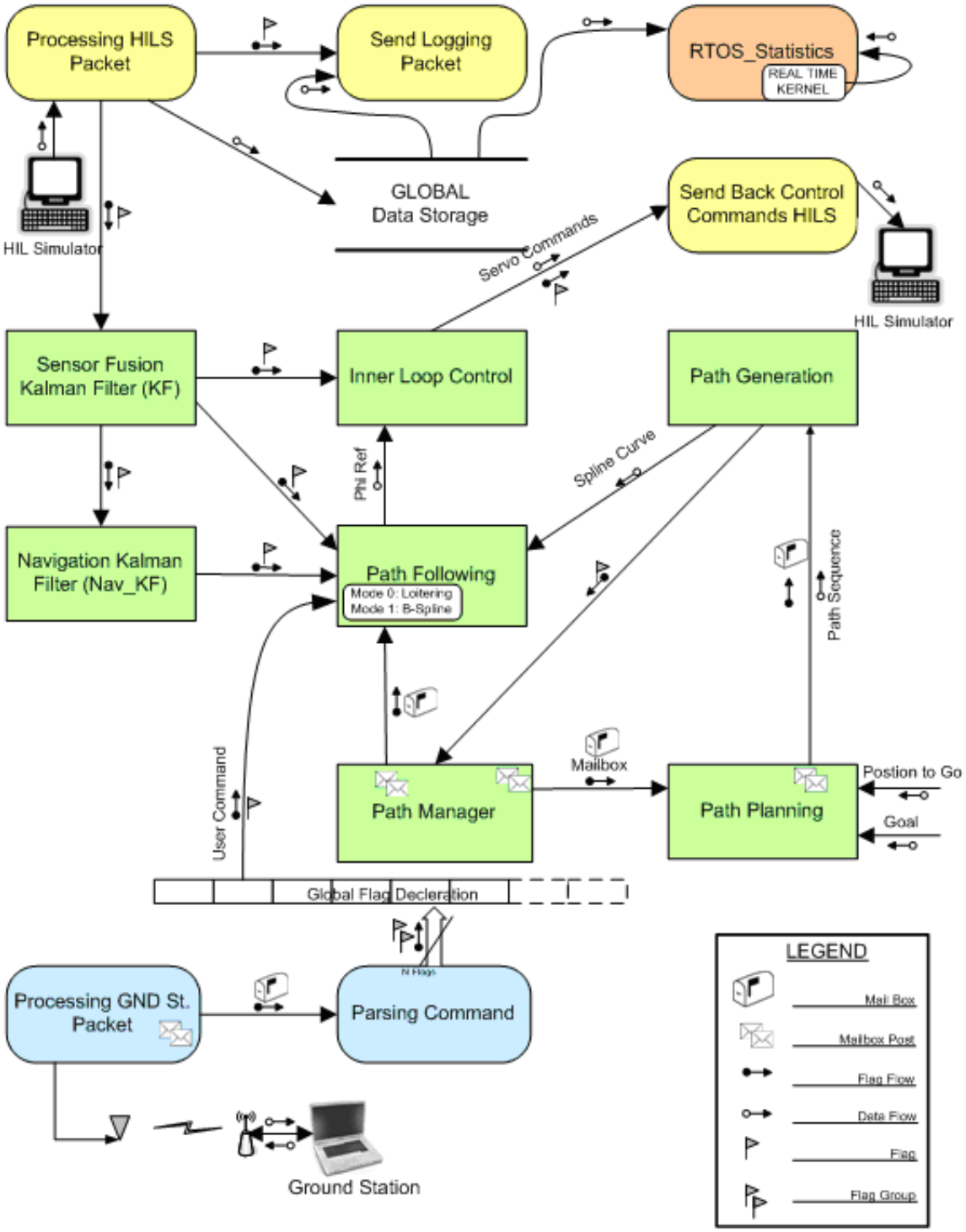

Figure A.26: RTOS Architecture for path planning and control on-board the MAV

Table A.3: Power and Weight Configuration of the MARC-2

Component	**Weight (Grams)**	**Power (mW)**
Cyclone- FPGA	2	245 (133Mhz)
TI-DSP	1.25	210 (200Mhz)
3-Axis Accelerometer	0.02	0.35
2-Axis Gyroscopes (x2)	0.03	21
Serial-Flash	1.5	0.3 (Standby)
ADC	0.035	9
CMOS Sensor	0.2	68 (15fps)
Quad-Full Bridge Drivers (x2)	0.25	180
Bare-PCB	5.5	5 (Losses-Approx)
Power Regulators, Switches, LEDs	2	55 (Losses-Approx)
Passives, Wiring	3	40 (Losses)
Total	15.75	833 mW (0.83W)
Total (w/o Motor Drivers)	15.5	653 mW (0.65W)

cient to debug faults in low-level, mid-level or high-level tasks/controls, without having to re-code/interfere with the other tasks/controllers.

REFERENCES

[1] R. Ames, O. Wong, and N. Komerath. *Fixed and Flapping Wing Aerodynamics for Micro Air Vehicle Applications*, volume V-195, chapter "On the Flowfield and Forces Generated by a Flapping Rectangular Wing at Low Reynolds Number". AIAA, 2001.

[2] K. J. Astrom and K. Furuta. Swinging up a pendulum by energy control. In *IFAC 13th World Congress*, 1996.

[3] A. Betz. Ein beitrag zur erklarung des segelfluges (a contribution to the explanation of gliding). *Zeitschrift fur Flugtechnik und Motorluftschiffahrt (Journal of flight technology and engine air shipping)*, 3:269–272, 1912.

[4] N.C. Cheung, K.W. Lim, and M.F. Rahman. Modeling a linear and limited travel solenoid. In *IECON Proc. of the Industrial Electronics, Control, and Instrumentation*, 1993.

[5] Henrik B. Christophersen, Wayne J. Pickell, Adrian A. Koller, Suresh K. Kannan, and Eric N. Johnson. Small adaptive flight control system for uavs using fpga/dsp technology. In *Proceedings of the AIAA "Unmanned Unlimited" Technical Conference, Workshop, and Exhibit, 2004*, 2004.

[6] Adam Cox, Daniel Monopoli, Dragan Cveticanin, Michael Goldfarb, and Ephrahim Garcia. The development of elastodynamic components for piezoelectrically actuated flapping micro-air vehicles. *Journal of Intelligent Material Systems and Structures*, 13(9):611–615, 2002.

[7] M.H. Dickinson. Solving the mysteries of insect flight. *Scientific American*, 284(6):49–57, 2000.

[8] Joerg S. Dittrich and Eric N. Johnson. Multi-sensor navigation system for an autonomous helicopter. In *Digital Avionics Systems Conference, 2002. Proceedings. The 21st*, volume 2, pages 8C1–1 – 8C1–19, December 2002.

[9] C. P. Ellington. Aerodynamics and the origin of insect flight. *Advances in Insect Physiology*, 23:171–210, 1991.

[10] C. P. Ellington. The novel aerodynamics of insect flight: Applications to micro-air vehicles. *Journal of Experimental Biology*, 202:3439–3448, 1999.

[11] Jack Elston, Brian Argrow, and Eric Frew. A distributed avionics package for small uavs. In *AIAA Infotech@Aerospace*, 2005.

[12] Benjamin M Finio, Brandon Eum, Christopher Oland, and Robert J Wood. Asymmetric flapping for a robotic fly using a hybrid power-control actuator. In *IROS*, 2009.

[13] R. Freethy. *How Birds Work, A Guide to Bird Biology*. Blanford Press, London, Dorset, UK, 1st ed. edition, 1982.

[14] K. Furuta, M. Yamakita, and S. Kobyashi. Swingup control of inverted pendulum using pseudo-state feedback. *Journal of Systems and Control Eng.*, 206(6):263–269, 1992.

[15] J. Grasmeyer and M. Keenon. Deveopment of the black widow micro aeri vehicle. In *39th AIAA Aerospace Sciences Meeting and Exhibit*, 2001.

[16] Slawomir Grzonka, Giorgia Grisetti, and Wolfram Burgard. Towards a navigation system for autonomous indoor flying. In *Proceedings of the 2009 IEEE international conference on Robotics and Automation*, pages 1679–1684. IEEE Press, 2009.

[17] K. Isogai and Y. Shinmoto. On generation of hovering force by mutual interactions of oscillating tandem airfoils. *Forum of 15th Symposium on the Computational Fluid Dynamics of Aircraft*, 37:191–203(in Japanese), 1999.

[18] Eric N. Johnson and Daniel P. Schrage. The georgia tech unmanned aerial research vehicle: Gtmax. In *Proceedings of the AIAA Guidance, Navigation, and Control Conference*, 2003.

[19] Dongwon Jung, Jayant Ratti, and Panagiotis Tsiotras. Real-time implementation and validation of a new hierarchical path planning scheme of uavs via hardware - in - the - loop simulation. *Journal of Intelligent and Robotic Systems*, 54(3):163–181, 2009.

[20] Aaron D. Kahn and James C. Kellogg. A low-cost, minimum complexity altitude/heading hold flight control system. In *Digital Avionics Systems Conference, 2002. Proceedings. The 21st*, volume 2, pages 8C2–1 – 8C2–6, 2002.

[21] Farid Kendoul, Yu Zhenyu, and Kenzo Nonami. Embedded autopilot for accurate waypoint navigation and trajectory tracking: Application to miniature rotorcraft uavs. In *IEEE Conference on Robotics and Automation*, 2009.

[22] Jishnu Keshavan, Norman M. Wereley, and Alfred Gessow. Design and development of a high frequency biologically-inspired flapping wing mechanism. In *48th AIAA/ASME/ASCE/AHS/ASC Structures, Structural Dynamics, and Materials Conference, Honolulu, Hawaii*, 2007.

[23] Z. A. Khan and S. K. Agrawal. Design and optimization of a biologically inspired flapping mechanism for flapping wing micro air vehicles. In *IEEE International Conference on Robotics and Automation*, 2007.

[24] R. Knoller. Die gesetze des luftwiderstandes (the laws of air resistance). *Flugund Motortchnik*, 3:1–7, 1909.

[25] R. Kornbluh. Project mentor: Biologically inspired platform. In *Keynote Presentation at the 8th AIAA/CEAS Aeroacoustics Conference*, June 2002.

[26] H. Liu and K. Kawachi. *Fixed and Flapping Wing Aerodynamics for Micro Air Vehicle Applications*, volume V-195, chapter "Leading-Edge Vortices of Flapping and Rotary Wings at Low Reynolds Number". AIAA, 2001.

[27] M. A. Mashraf, J. C. S. Lai, and J. Young. *Fixed and Flapping Wing Aerodynamics for Micro Air Vehicle Applications*, volume V-195, chapter "Numerical Analysis of Flapping Wing Aerodynamics". AIAA, 2001.

[28] R. Michelson. Update on flapping wing micro air vehicle research-ongoing work to develop a flapping wing, crawling entomopter. In *13th Bristol International RPV/UAV Systems Conference Proceedings, Bristol England*, pages 30.1 – 30.12, 1998.

[29] Robert Michelson, Daniel Helmick, Steven Reece, and Carmelo Amarena. A reciprocating chemical muscle (rcm) for micro air vehicle 'entomopter' flight. In *Proc. of the Association for Unmanned Vehicle Systems International*, pages 429–435, 1997.

[30] Taner Mutlu, Sertac Karaman, Savas Comak, Ismail Bayezit, Gokhan Inalhan, and Levent Guvenc. Development of a cross-compatible micro-avionics system for aerorobotics. In *Intelligent Vehicles Symposium, IEEE*, 2007.

[31] W. Nachtigall. *Insects in Flight*. McGraw-Hill, New York, 1974.

[32] M. F. Neef and D. Hummel. *Fixed and Flapping Wing Aerodynamics for Micro Air Vehicle Applications*, volume V-195, chapter "Euler Solutions for a Finite-Span Flapping Wing". AIAA, 2001.

[33] Burton Paul. *Kinematics and Dynamics of Planar Machinery*. Prentice-Hall Publication, 1979.

[34] Darryll J. Pines and Felipe Bohorquez. Challenges facing future micro-air-vehicle development. *Journal of Aircraft*, 43(2):290–305, 2006.

[35] Daniel Prosser, Taher Basrai, Jason Dickert, Jayant Ratti, Agamemnon Crassidis, and George Vachtsevanos. Wing kinematics and aerodynamics of a hovering flapping micro aerial vehicle. In *IEEE Aerospace*, 2011.

[36] David L. Raney and Eric C. Slominski. Mechanization and control concepts for biologically inspired micro air vehicles. *Journal of Aircraft*, 41(6):1257–1265, 2004.

[37] Jayant Ratti, Rohan Goel, Seon-Joo Kim, Jung-Ho Moon, Thomas D. Pappas, George Vachtsevanos, and Mike Roemer. Bio-inspired micro air vehicle: Design and control issues. In *AIAA Infotech@Aerospace*, 2010.

[38] Jayant Ratti, Arvind Jayaraman, Anubhav Singh, Jagdeep Singh, Ankur Saxena, Amandeep Premi, Ankur Khetrapal, Sahil Malhotra, Pranav Kedia, and Rahul Gaba. Dual quad-rotor uav system. In *Delhi College of Engineering, University of Delhi, www.uavindia.com*, 2006.

[39] Jayant Ratti, Emanuel M. Jones, and George Vachtsevanos. Fixed frequency variable amplitude (fifva) actuation systems for micro aerial vehicles. In *IEEE International Conference on Robotics and Automation@ICRA*, 2011.

[40] Jayant Ratti, Jung-Ho Moon, and George Vachtsevanos. Towards low-power, low-profile avionics architecture and control for micro aerial vehicles. In *IEEE Aerospace*, 2011.

[41] Jayant Ratti and George Vachtsevanos. A biologically - inspired micro aerial vehicle: Sensing, modeling and control strategies. *Journal of Intelligent and Robotic Systems*, 60(1):153–178, 2010.

[42] Jayant Ratti and George Vachtsevanos. Towards energy efficiency in micro hovering air vehicles. In *IEEE Aerospace*, 2011.

[43] J. M. Rayner. A new approach to animal flight mechanics. *Journal of Experimental Biology*, 80:17–54, 1979.

[44] A.L. Rodriguez, L.M. Parrilla, A. Simon-Muela, M.M. Prats, C. Querejeta, and F.G. de Blanes. Real time sensor acquisition platform for experimental uav research. In *Digital Avionics Systems Conference, 2009. DASC '09. IEEE/AIAA 28th*, pages 5.C.5–1 – 5.C.5–10, 2009.

[45] P. Samuel, J. Sirohi, L. Rudd, D. Pines, and R. Perel. Design and development of a micro coaxial rotorcraft. In *Proceedings of the AHS Vertical Lift Aircraft Design Conference, American Helicopter Society*, Alexandria, VA, Jan 2000.

[46] S. P. Sane and M. H. Dickinson. The control of flight force by a flapping wing: Lift and drag production. *The Journal of Experimental Biology*, page 20, 2001.

[47] S. P. Sane and M. H. Dickinson. The aerodynamic effects of wing rotation and a revised quasi-steady model of flapping flight. *The Journal of Experimental Biology*, page 10, 2002.

[48] T. Nick Pornsin sirirak, S.W. Lee, H. Nassef, J. Grasmeyer, Y.C. Tai, C.M. Ho, and M. Keenon. Mems wing technology for a battery-powered ornithopter. In *Proc. of the 13th IEEE Annual International Conference on MEMS*, 2000.

[49] Theodore Theodorsen. General theory of aerodynamic instability and the mechanism of flutter [online], 1935.

[50] J. M. Wakeling and C. P. Ellington. Dragonfly flight: I. gliding flight and stead-state aerodynamic forces. *Journal of Experimental Biology*, 200:543–556, 1997.

[51] J. M. Wakeling and C. P. Ellington. Dragonfly flight: Ii. velocities, accelerations and kinematics of flapping flight. *Journal of Experimental Biology*, 200:557–582, 1997.

[52] Z. J. Wang. Two dimensional mechanism for insect hovering. *Physical Review of Letters*, 85(10):2035, 2000.

INDEX

VITA

Jayant Ratti was awarded a B.E. degree in Electronics and Communication from the University of Delhi, India in 2006, a M.S. degree in Electrical and Computer Engineering from the Georgia Institute of Technology, Atlanta, Georgia, USA in 2008 and is presently pursuing his Ph.D. in Robotics at the Georgia Institute of Technology, Atlanta. His present activities and Ph.D. research relates to the design, development, modeling and control of Unmanned Aerial and Micro Aerial Vehicles. He is presently leading the engineering team on the QV-MAV development program at Georgia Tech campus. He won the Best Poster Design Award at the Georgia Tech Research and Innovation Conference for his research on the MAV. He also won the First Prize at the Robotics Innovation Conference and Competition, April 2011 at Woburn, MA. He has over 8 publications (including one recently at IEEE ICRA 2011). He also has four patents to his name for the Micro Aerial Vehicle Design. His experience/interest in the field of robotics expands into embedded-systems, controls, mechatronics, machine vision, Unmanned Ground/Air Vehicle design/development/integration. He is also the inventor/founder of TechJect, Georgia Tech's Online Project and Research Network. His other interests include physical training, swimming, playing chess, reading about ancient and modern history, societies and cultures. He was a nationally ranked chess player in school and was awarded the Sports Star of the Year in his High School along with a scholar with distinction. He has won numerous First Prizes in robotics and innovation contests both at the national and international levels, including the "Most Innovative Design" design award for the "Dual-Quad-Rotor UAV" Design at the International Aerial Robotics Competition (IARC) in 2006, held at Fort Benning, USA; for which he was the team lead from University of Delhi.